Theoretical Studies on Electron Transport and Stability of π-Conjugated Single-Molecule Junctions

岡澤, 一樹

https://hdl.handle.net/2324/7182432

出版情報：九州大学, 2023, 博士（工学）, 課程博士
バージョン：
権利関係：

Theoretical Studies on Electron Transport and Stability of π-Conjugated Single-Molecule Junctions

Kazuki Okazawa

Department of Applied Chemistry

Graduate School of Engineering

Kyushu University

2023

Table of Contents

Chapter 1 General Introduction 4

1.1. Single-Molecular Electronics 4

1.2. Single-Molecule Measurements 6

1.3. Conduction Properties of Single-Molecule Junctions 9

1.4. Survey of This Thesis 11

Chapter 2 Theoretical Background 14

2.1. Electron Transport Calculation by Using the NEGF Method 14

2.2. Orbital Rule for Electron Transport 18

Chapter 3 Frontier Orbital View in Conduction Properties of Single-Molecule Parallel Circuits 22

3.1. Introduction 23

3.2. Computational Details 26

3.3. Results and Discussion 27

3.3.1. Transmission Calculations for Aromatic and Non-Aromatic Doubled Paths 27

3.3.2. Frontier Orbital Analysis for Aromatic and Non-Aromatic Doubled Paths 31

3.3.3. Circuit Whose Conductance Does Not Vary with the Number of Paths 39

3.3.4. Conductance of Anti-Aromatic Parallel Circuits 45

3.4. Conclusions 49

3.5. Appendix 50

3.5.1. Resistance Distance 50

Chapter 4 Frontier Orbital View of Conductivity in Highly Conductive Single-Molecule Wires Based on One-Dimensional Topological Insulators 52

4.1. Introduction 53

4.2. Results and Discussion 56

4.2.1. Derivation of the Modified Relation between the Conductance and the Resonance Integrals for Polyene Wires. 56

4.2.2. Comparison between Eq. (4.10) and the Results by the NEGF–HMO 59
4.2.3. Frontier Orbital Analysis for the Wire 62
4.3. Conclusions 65

Chapter 5 Graph Theoretical Study on the Conduction Properties of Heteroatom Containing Single-Molecule Junctions 66

5.1. Introduction 67
5.2. Results and Discussion 69
5.2.1. Derivation of ZOGF Based on the Graph Theory 69
5.2.2. Derivation of ZOGF for a Single-Molecule Junction with a Heteroatom 73
5.2.3. Application to the Six-Membered Ring Systems 77
5.3. Conclusion 83

Chapter 6 Frontier Orbital Insights into the Distance Dependence of the Appearance of Stacked Aromaticity 84

6.1. Introduction 85
6.2. Computational Details 87
6.3. Results and Discussion 88
6.3.1. Evaluations of Aromaticity 88
6.3.2. Frontier Orbital View for the D_{4h} Dimer 91
6.3.3. Frontier Orbital View for the D_{2h} Dimer 93
6.3.4. Relationship between the Stacked Aromaticity and HOMO–LUMO gap of the monomer 96
6.4. Conclusion 99
6.5. Appendix 100
6.5.1. Analysis of the relationship between bond alternation and HOMO-LUMO gap of cyclobutadiene using the Hückel method 100

Chapter 7 General Conclusions 102

References 104

Acknowledgement 115

List of Publications 116

Chapter 1

General Introduction

1.1. Single-Molecular Electronics

Silicon-based semiconductors play a central role in modern computer technology. According to Moore's law, the number of transistors that can be placed in an integrated circuit and the computing speed doubles approximately every two years. Moore's law is not a scientific or physical law, but an empirical relationship by Gordon Moore, co-founder of Intel. His prediction has held since 1975 and has been known as "the law" ever since. To date, technological innovations in the semiconductor industry have maintained miniaturization of complementary metal-oxide-semiconductor (CMOS) technology. However, further miniaturization can become prohibitively expensive as device variation increases, and this technology will eventually face fundamental limitations, primarily due to direct tunneling of electrons between source and drain. Therefore, further miniaturization of electronics requires a shift from top-down to bottom-up manufacturing components.

In their pioneering theoretical study, Arieh Aviram and Mark Ratner suggested that a single molecule could act as a rectifier (Scheme 1.1).[1] The molecule mimics a semiconductor-like band structure by utilizing an electron-donating molecule, tetrathiafulvalene (TTF), and an electron accepting molecule, tetracyanoquinodimethane (TCNQ), which are aligned in different directions relative to the Fermi energy of the electrode. In this approach, the potential for electronic functional design is determined by a bottom-up synthesis method using atomically identical basic building blocks. This is still a revolutionary concept today, given the increasing device variability in controlling the position and distance of a smaller number of atoms in the active region of devices made by the top-down method. At the time, however, it was impossible to experimentally verify their predictions.

Scheme 1.1. Aviram-Ratner rectifier.

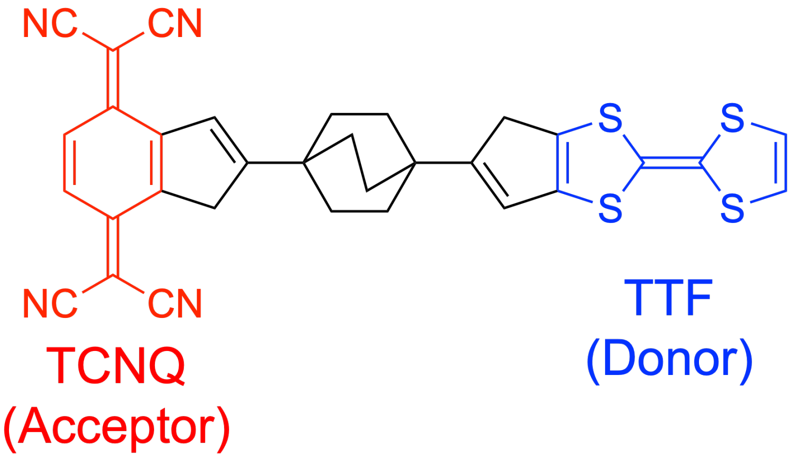

1.2. Single-Molecule Measurements

To form single-molecule junctions with molecules that are less than a few nanometers in size, it is necessary to create electrodes with the same distance between them as the molecules, i.e., nanogap electrodes. More than two decades after Aviram and Ratner's proposal, nanogap electrodes have been realized and single-molecule electronics have been experimentally demonstrated to be possible. The electrical conductivity of a single molecule could be measured with high reproducibility. Two techniques are shown below.

In 1997, Mark Reed was the first to successfully measure the electrical conductivity of 1,4-benzenedithiol molecules using the mechanically controllable break junction (MCBJ) technique.[2] In the MCBJ technique, a metal wire with a pre-cut break in the center is fixed at two points on an insulation-coated substrate. By bending the base, the wire is broken at the point where the center of the wire is cut. In this process, the metal is curved using a piezoelectric device to control the joint elongation distance with a high degree of accuracy. Immediately after the metal junction is broken, a large number of molecules cross-link the electrodes, but as the distance between the metal wires increases, the number of cross-linking molecules decreases and eventually a single-molecule junction is formed. This process can be repeated thousands of times and statistically analyzed to obtain reliable values of the single-molecule conductance.

In 2003, Nongjian Tao presented the scanning tunneling microscope break junction (STM-BJ) technique.[3] In this method, a gold STM tip is repeatedly brought into contact and released from a gold substrate in a sample solution. The iterative process of retracting the tip records thousands of conductance traces in a relatively short period of time. The conductance of a single molecule can be determined by statistically analyzing the conductance traces, which show a gradual decrease in conductance.

There are also conductance measurement techniques such as conductive atomic force microscopy (AFM) junctions,[4] electromigration break junctions,[5] and graphene-molecule-graphene single-molecule junctions.[6] With the establishment of these techniques, research on single-molecule devices has increased dramatically. For example, 1,4-benzenedithiol, first measured by Reed et al., exhibited insulator-like behavior. Recently molecules with conductance close to that of metals have been discovered.[7] In addition, various single-molecule rectifiers,[8] transistors,[9] and switches[10] have been designed. Furthermore, these methods are powerful tools not only for the study of single-molecule devices, but also for exploring fundamental principles of physics and chemistry, such as understanding single-molecule properties and chemical reactions at the single-molecule level.[11–13]

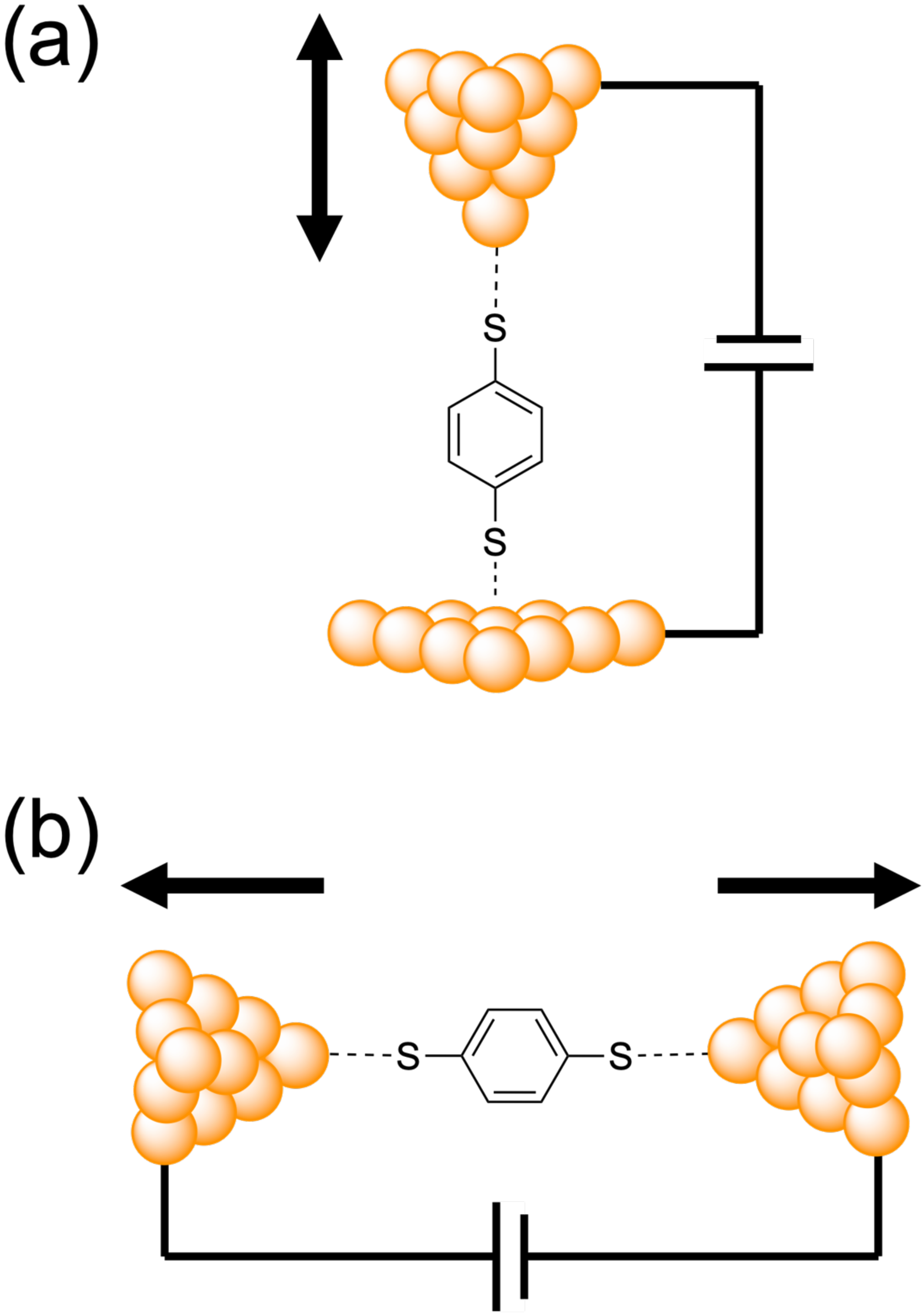

Figure 1.1. Schematics of (a) STM-BJ and (b) MCBJ techniques, respectively.

1.3. Conduction Properties of Single-Molecule Junctions

Many studies that have been conducted have shown that quantum effects dominate the conduction mechanism of single-molecule junctions. For example, electron transport by tunneling conduction and interference between electron waves, i.e., quantum interference. In long wires, electrons propagate by colliding with scatters such as atoms and lattice defects within the wire. At the single-molecule scale, the length of the system is equal to or short as the mean free path, so the electrical conduction properties are different from those of long wires. In single-molecule junctions, electrons transport from one electrode to the other by the tunneling effect. The conductance of a single-molecule junction is obtained from the Landauer formula.[14] Quantum interference significantly affects the electrical conduction properties of single-molecule junctions. When there is a constructive quantum interference, i.e., the electrons are in phase, the conductance increases. On the other hand, when there is a destructive quantum interference, i.e., electrons are in opposite phases, the conductance decreases, indicating insulating properties. The existence of the constructive quantum interference has been confirmed by conductance measurements of single-molecule parallel circuits.[15,16] The destructive quantum interference has been reported to appear in cross-conjugated systems.[17,18] The destructive quantum interference is also strongly correlated with the bonding pattern between the electrode and the molecule. The conductance of benzene with the Au electrode connected to the *meta*-position is theoretically predicted to be smaller than that with the Au electrode connected to the *para*-position, and this has been confirmed by experiment.[17,19–22] Figure 1.2 shows the electron transmission probability spectra obtained by using the non-equilibrium Green’s function (NEGF) combined with the Hückel molecular orbital (HMO) method. Quantum interference is an essential phenomenon for the development of functional single-molecule junctions.

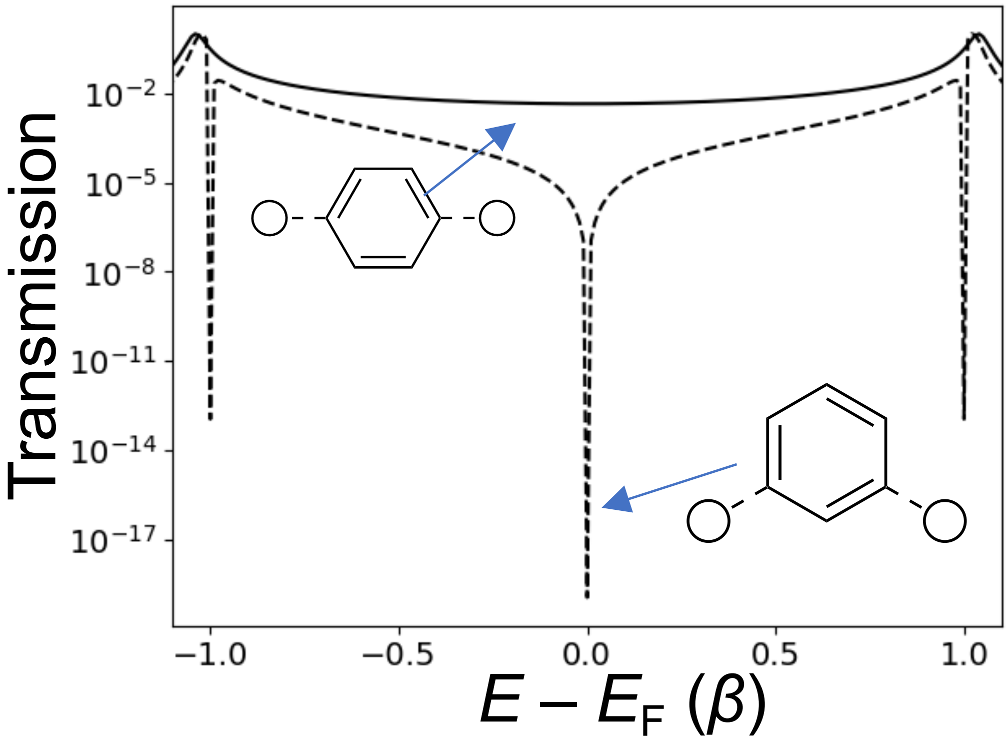

Figure 1.2. Transmission spectra for the *para*-connected benzene (solid line) and the *meta*-connected benzene (dashed line). These spectra are obtained by using the NEGF combined with the Hückel molecular orbital (NEGF–HMO) method.

To understand theoretically the electron transport phenomena in single molecule junctions, the Landauer formula and the NEGF method are very useful. Theoretical predictions of quantum interference have been proposed based on frontier orbital theory[20,23] and graph theory.[24] The approach based on frontier orbital theory allows for the description of the energy level difference between the highest occupied molecular orbital (HOMO) and lowest unoccupied molecular orbital (LUMO) of the molecule, and the orbital coefficients of the HOMO/LUMO of the two atoms in contact with the electrodes, in relation to the Fermi energy. The graph theory-based method treats the molecule as a graph and can predict the presence of destructive quantum interference by counting the pathways from one electrode to the other electrode.

1.4. Survey of This Thesis

Previous prediction methods are particularly effective in alternant hydrocarbon systems, but are not applicable to asymmetrically splitting systems, i.e., molecules containing heteroatoms or non-alternant hydrocarbons. In this study, the author extends the orbital rule for electron transport and the graph-theoretical approach to clarify their applicability to these systems. Whereas the previous prediction methods have focused on destructive quantum interferences that cancel each other out completely, this study will focus on other types of quantum interferences. Furthermore, it is necessary to consider not only the conductivity of the molecule but also its stability. For example, anti-aromatic molecules with a narrow HOMO-LUMO gap are highly conductive, but their instability makes them difficult to synthesize. In this dissertation, the author presents quantum chemistry-based investigations of the electrical conduction properties of π-conjugated single-molecule junctions and the aromaticity that is related to the stability of highly conductive molecules. This is expected to provide new insights into the properties of various types of quantum interference in single-molecule junctions. This approach will provide comprehensive knowledge of the conduction properties of single-molecule junctions and will lay the groundwork for the design of future single-molecule devices.

The dissertation is composed of seven chapters, as follows.

In Chapter 2, the author provides details on electron transport calculations using the nonequilibrium Green's function method, the relationship between the nonequilibrium Green's function and the zeroth order Green’s function (ZOGF), and the orbital rules for electron transport.

In Chapter 3, the author shows that the conductance of single molecule parallel circuits deviates from the superposition relationship applied to macroscale circuits by quantum interference. The author also elucidates whether constructive or destructive quantum interference occurs in terms of aromaticity and frontier orbital theory. (*J. Phys. Chem. C* **124**, 5, 3322-3331 (2020))

The conductivity of highly conductive single molecule wires designed on the basis of a one-dimensional topological insulator model cannot be explained in the framework of the ZOGF. Chapter 4 provides an explanation for this conduction property in the form of an extension of the ZOGF. (*to be Submitted*)

Single molecular junctions containing heteroatoms have different electron transport properties compared to hydrocarbon single-molecule junctions consisting only of carbon and hydrogen atoms with the same topology. However, as discussed in the previous section, the graph-theoretic path-counting method is only applicable to alternant hydrocarbons. In Chapter 5, the author extends the graph-theoretical path-counting method to apply to systems containing a heteroatom. (*J. Chem. Phys.* **156**, 9, 091102 (2022))

Next, the author discusses the stability of anti-aromatic molecules that have the potential to become highly conductive single molecular wires. Anti-aromatic molecules are unstable due to their very narrow HOMO-LUMO gap. In Chapter 6, the author reveals the origin of the stabilization of anti-aromatic molecules by face-to-face stacking using frontier orbital theory. (*J. Phys. Chem. A*, **127**, 22, 4780-4786 (2023))

Finally, in Chapter 7, the author provides a summary of the findings and discuss future research directions.

Chapter 2

Theoretical Background

2.1. Electron Transport Calculation by Using the NEGF Method

In the standard Landauer-Büttiker approach,[25] the conductance of a single molecular junction, composed of a molecule and two metal electrodes, is expressed as follows:

$$g = \frac{2e^2}{h} T(E_\mathrm{F}) \tag{2.1}$$

where $2e^2/h$ represents the conductance quantum, $T(E_\mathrm{F})$ denotes the electron transmission function or probability, and E_F stands for the energy of the Fermi level, under the limit of zero bias and zero temperature.

The transmission function can be obtained using the non-equilibrium Green's function (NEGF) method.[26] Employing this method allows for the calculation of the transmission function as follows:

$$T(E_\mathrm{F}) = \mathrm{Tr}[\mathbf{\Gamma}_\mathrm{L} \mathbf{G}^\mathrm{R} \mathbf{\Gamma}_\mathrm{R} \mathbf{G}^\mathrm{A}] \tag{2.2}$$

where $\mathbf{G}^{\mathrm{R(A)}}$ is the retarded (advanced) Green's function matrix, and $\mathbf{\Gamma}_{\mathrm{L/R}}$ is the broadening function matrix for the left/right electrode. The Green's function is calculated as follows:

$$\mathbf{G}(E) = [(E + i\eta)\mathbf{I} - \mathbf{H} - \mathbf{\Sigma}_{\mathrm{L}} - \mathbf{\Sigma}_{\mathrm{R}}]^{-1} \tag{2.3}$$

where η is a positive infinitesimal, $\mathbf{I}$ is the identity matrix, $\mathbf{H}$ is the Hamiltonian matrix for the molecule bridged between the two electrodes, and $\mathbf{\Sigma}_{\mathrm{L/R}}$ is the self-energy matrix describing the interaction between the molecule and the left/right electrode.

The relation between the self-energy matrix $\mathbf{\Sigma}$ and the broadening function matrix $\mathbf{\Gamma}$ can be expressed as follows:

$$\mathbf{\Gamma}_{\mathrm{L(R)}} = i\left[\mathbf{\Sigma}_{\mathrm{L(R)}} - \mathbf{\Sigma}^{\dagger}_{\mathrm{L(R)}}\right] \tag{2.4}$$

The matrix elements of the self-energy for the left (L) and right (R) contacts in eq. (2.4) can be obtained as

$$[\mathbf{\Sigma}_{\mathrm{L}}]_{mn} = \sum_{\alpha,\beta\in\mathrm{L}} \tau_{m\alpha}[\boldsymbol{g}_{\mathrm{L}}]_{\alpha\beta}\tau^{\dagger}{}_{\beta n} \tag{2.5}$$

and

$$[\mathbf{\Sigma}_{\mathrm{R}}]_{mn} = \sum_{\alpha',\beta'\in\mathrm{R}} \tau_{m\alpha'}[\boldsymbol{g}_{\mathrm{L}}]_{\alpha'\beta'}\tau^{\dagger}{}_{\beta' n} \tag{2.6}$$

respectively. $\boldsymbol{g}_{\mathrm{L/R}}$ is the Green's function matrix for the left/right electrode. $\tau_{m\alpha}$ is the hopping integral between the site m in the molecular region and site α in the electrode region. Here, Latin letters denote molecular sites and Greek letters denote electrode sites. Consider the case where only the terminal atoms of the left and right electrodes, i.e., site α of the left electrode and site α' of the right electrode, are attached to the sites r and s of the molecule, respectively (see Figure 2.1). The self-energy matrix has a non-zero element as follows:

$$[\mathbf{\Sigma}_{\mathrm{L}}]_{rr} = \tau_{r\alpha}[\boldsymbol{g}_{\mathrm{L}}]_{\alpha\alpha}\tau^{\dagger}{}_{\alpha r} \tag{2.7}$$

and

$$[\mathbf{\Sigma}_{\mathrm{R}}]_{ss} = \tau_{s\alpha'}[\boldsymbol{g}_{\mathrm{R}}]_{\alpha'\alpha'}\tau^{\dagger}{}_{\alpha' s} \tag{2.8}$$

The left and right electrodes are modeled by an ideal one-dimensional (1D) linear gold chain. The Green's function for such a 1D system can be obtained as follows:[27]

$$[\boldsymbol{g}_{\mathrm{L}}]_{\alpha\alpha} = [\boldsymbol{g}_{\mathrm{R}}]_{\alpha'\alpha'} = \frac{\exp(ika)}{\tau_{\mathrm{elec}}} \tag{2.9}$$

Here ka has to satisfy the condition of $E = \varepsilon_{\mathrm{elec}} + 2\tau_{\mathrm{elec}}\cos ka$, where $\varepsilon_{\mathrm{elec}}$ and τ_{elec} are the on-site energy and the nearest-neighbor hopping integral in the gold electrodes, respectively. It is assumed that $\varepsilon_{\mathrm{elec}}$ should coincide with the Fermi energy.

The conductance depends on the broadening function matrix $\mathbf{\Gamma}_{\mathrm{L(R)}}$ as well. In this study, the author begins with a simple situation where two specific atoms denoted by r and s in the molecule are connected to the electrodes as shown in Figure 2.1. In this case, the broadening function matrix $\mathbf{\Gamma}_{\mathrm{L(R)}}$ has only one non-zero element as follows:

$$[\mathbf{\Gamma}_{\mathrm{L}}]_{rr} = \gamma_{\mathrm{L}} \tag{2.10}$$

and

$$[\mathbf{\Gamma}_{\mathrm{R}}]_{ss} = \gamma_{\mathrm{R}} \tag{2.11}$$

so that from eq. (2.2) it can be written as follows:

$$T(E_{\mathrm{F}}) = \gamma_{\mathrm{L}}\gamma_{\mathrm{R}}|G_{rs}(E_{\mathrm{F}})|^2 \tag{2.12}$$

This equation indicates that the transmission and thus the conductance are directly proportional to the (r, s) element of the NEGF.

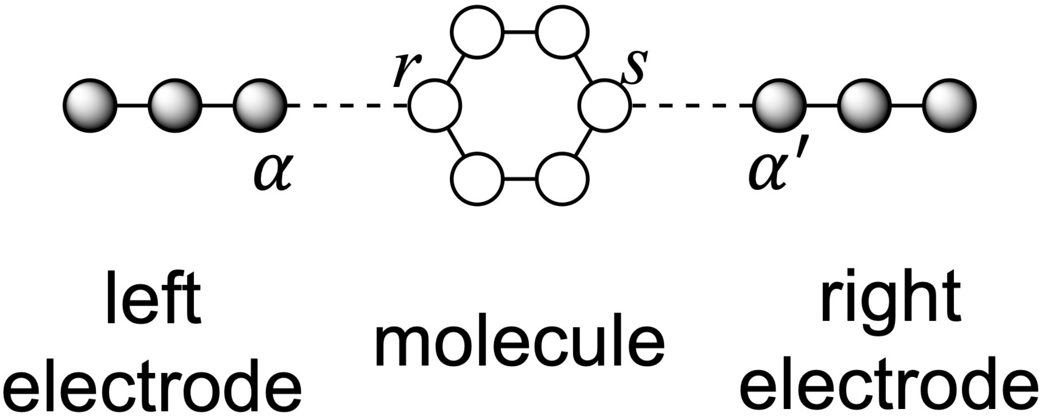

Figure 2.1. Schematic representation of the two-probe molecular junction.

2.2. Orbital Rule for Electron Transport

All the transmission probabilities can be calculated by using eq. (2.2), which includes the NEGF, but the qualitative discussions rely on what the author may call the zeroth order Green's function (ZOGF). Here, the author shows how one could connect the two. In these studies, the author considers molecules weakly coupled to the electrode so that the conduction properties can be understood from the approximate Green's function, or zeroth Green's function, $\mathbf{G}^{(0)}$, at the Fermi level:

$$\mathbf{G}(E_{\mathrm{F}}) \approx \mathbf{G}^{(0)} = [(E_{\mathrm{F}} + i\eta)\mathbf{I} - \mathbf{H}]^{-1} \tag{2.13}$$

This Green's function can be regarded as the (unperturbed) Green's function of the molecule that does not interact with the electrode. The direct relation between the unperturbed Green's function and the perturbed Green's function G_{rs} can be obtained using the Dyson equation as follows:

$$G_{rs} = G_{rs}^{(0)} + \sum_{ij} G_{ri}^{(0)} \Sigma_{ij} G_{js} \tag{2.14}$$

As shown in eqs. (2.7) and (2.8), most of the matrix elements of $\mathbf{\Sigma}$ are zero. Therefore, the equation can be further simplified as follows:

$$G_{rs} = G_{rs}^{(0)} + G_{rr}^{(0)} [\mathbf{\Sigma}_{\mathrm{L}}]_{rr} G_{rs} + G_{rs}^{(0)} [\mathbf{\Sigma}_{\mathrm{R}}]_{ss} G_{ss} \tag{2.15}$$

Here, G_{ss} can also be calculated from another Dyson equation as follows:

$$G_{ss} = G_{ss}^{(0)} + G_{ss}^{(0)} [\mathbf{\Sigma}_{\mathrm{R}}]_{ss} G_{ss} + G_{sr}^{(0)} [\mathbf{\Sigma}_{\mathrm{L}}]_{rr} G_{rs} \tag{2.16}$$

Substituting eqs. (2.7) and (2.8) into eqs. (2.15) and (2.16), G_{rs} is given by,

$$G_{rs} = \frac{G_{rs}^{(0)}}{\left(1 - t^2 G_{rr}^{(0)} [\boldsymbol{g}_{\mathrm{L}}]_{\alpha\alpha}\right)\left(1 - t^2 G_{ss}^{(0)} [\boldsymbol{g}_{\mathrm{R}}]_{\alpha'\alpha'}\right) - t^4 [\boldsymbol{g}_{\mathrm{L}}]_{\alpha\alpha} [\boldsymbol{g}_{\mathrm{R}}]_{\alpha'\alpha'} \left(G_{rs}^{(0)}\right)^2} \tag{2.17}$$

It is assumed that all hopping integrals between the molecule and the electrode have the same value of t. If t is very small, the denominator in eq. (2.17) should be approximately 1. Therefore, it is reasonable to approximate $\mathbf{G}$ by $\mathbf{G}^{(0)}$.

Next, the ZOGF is expanded in the form of a molecular orbital as the basis. The time-independent Schrödinger equation with molecular orbitals $|k\rangle$ as eigenvectors is as follows:

$$\hat{H}|k\rangle = \varepsilon_k |k\rangle \tag{2.18}$$

where ε_k is the orbital energy for eigenstate k. The molecular orbitals satisfy the orthonormal condition.

$$\langle k|m\rangle = \delta_{km} \tag{2.19}$$

where δ_{km} is the Kronecker delta. The Green's function is defined as follows:

$$[(E + i\eta)\mathbf{I} - \mathbf{H}]\mathbf{G}^{(0)} = \mathbf{I} \tag{2.20}$$

Here, using eq. (2.18) and$\mathbf{I} = |k\rangle\langle k|$, the Green's function can be written down in the following form:

$$\mathbf{G}^{(0)} = \sum_k (E\mathbf{I} - \mathbf{H})^{-1} |k\rangle\langle k| = \sum_k \frac{|k\rangle\langle k|}{(E + i\eta) - \varepsilon_k} \tag{2.21}$$

Molecular orbitals are expanded using the linear combination of atomic orbital (LCAO) as shown below.

$$|k\rangle = \sum_{\alpha} C_{\alpha k} |\alpha\rangle \tag{2.22}$$

where $C_{\alpha k}$ is the orbital coefficient of atom α at the molecular orbital k. Substituting eq. (2.22) into eq. (2.21), $\mathbf{G}^{(0)}$ can be written as follows:

$$\mathbf{G}^{(0)} = \sum_{k} \sum_{\alpha\beta} \frac{|\alpha\rangle C_{\alpha k} C_{\beta k}^{*} \langle\beta|}{(E + i\eta) - \varepsilon_k} \tag{2.23}$$

When the electrodes contact the atoms r, s, the (r, s) component of $\mathbf{G}^{(0)}$ finally becomes as follows:

$$G_{rs}^{(0)}(E) = \sum_{k} \frac{C_{rk} C_{sk}^{*}}{E - \varepsilon_k + i\eta} \tag{2.24}$$

Since the Fermi level is assumed to be very close to the energy level of the frontier orbitals, the ZOGF is likely to be dominated by the contribution from the frontier orbital terms, leading to the following equation:

$$G_{rs}^{(0)}(E_{\mathrm{F}}) \approx \frac{C_{r,\mathrm{HOMO}} C_{s,\mathrm{HOMO}}}{E_{\mathrm{F}} - \varepsilon_{\mathrm{HOMO}}} + \frac{C_{r,\mathrm{LUMO}} C_{s,\mathrm{LUMO}}}{E_{\mathrm{F}} - \varepsilon_{\mathrm{LUMO}}} \tag{2.25}$$

In eq. (2.25), the infinitesimal positive number η is neglected for simplicity.

Chapter 3

Frontier Orbital View in Conduction Properties of Single-Molecule Parallel Circuits

In electronic devices, when the number of paths connecting the source and drain electrodes increase, the conductance of the device should also increase. This is true in the macroscopic case, but this is not always the case on the nanoscale. Kirchhoff's superposition law tells us that when the number of paths is doubled, the conductance is also doubled. However, as far as the path in a sense of molecular graph theory goes, things are not so simple. When the number of paths in a molecule gets doubled, three situations will arise: the conductance gets more than doubled, remains unchanged, or even gets smaller. Our theoretical study with the non-equilibrium Green's function method has revealed that the distinction of these situations has a close relation to the aromaticity of the ring formed as a result of doubling the path. The author will see how helpful it is to characterize the molecular transmission features relying on the frontier orbital theory, orbital interactions, and a local transmission concept. Some discrete mathematical aspects of the relation between the atom connectivity and electron conductivity are also described.

3.1. Introduction

It would be interesting to view the molecule as an element of the electrical circuit and compare it with the macroscopic one. According to the current superposition law, as shown in Scheme 3.1 the conductance values of the whole parallel circuit g is the sum of the conductance values of the respective resistors, g_1 and g_2, as follows:[28]

$$g = g_1 + g_2 \tag{3.1}$$

Scheme 3.1. An example of a macroscopic parallel electric circuit.

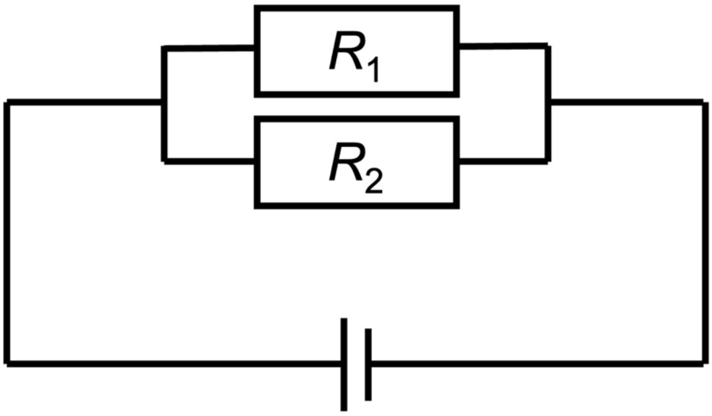

A molecule can be regarded as a graph, which is a discrete mathematical expression for a structure consisting of nodes and edges. This is an interdisciplinary field called chemical graph theory.[24,29] Scheme 3.2 shows hydrogen-depleted graphs for butadiene and benzene with their 1,4 positions connected with the electrode. In the case of butadiene, one can see only one path 1–2–3–4 connecting the two electrodes, while two paths are available for benzene. This is why one may view the benzene graph as a parallel circuit analogue compared to the butadiene graph. By means of some graph theoretic measures, one may expect that the connection between the two electrodes in the benzene junction would be stronger than the butadiene one. Graph theory can provide us with a qualitative measure of the topological distance separating two nodes in a molecular graph. There is one graph theoretic measure to estimate how much significant the communication between two nodes is. That is what is called resistance distance,[30,31] which is an index of distance between two arbitrary nodes and allow us to calculate the resistance between them when the resistance of all the edges in the graph is assumed to be unity. Conductance is calculated from the inverse of the resistance. The conductance values of butadiene and benzene calculated by using the resistance distance technique are 0.333 and 0.667, respectively. This reflects the stronger connection between the C1 and C4 sites in benzene than that in butadiene. Details of the calculation method for the resistance distance are given in the Appendix (section 3.5.1). These results show a good agreement with what is predicted from eq. (3.1).

Scheme 3.2. Molecular graph representations corresponding to (a) butadiene and (b) benzene molecular junctions.

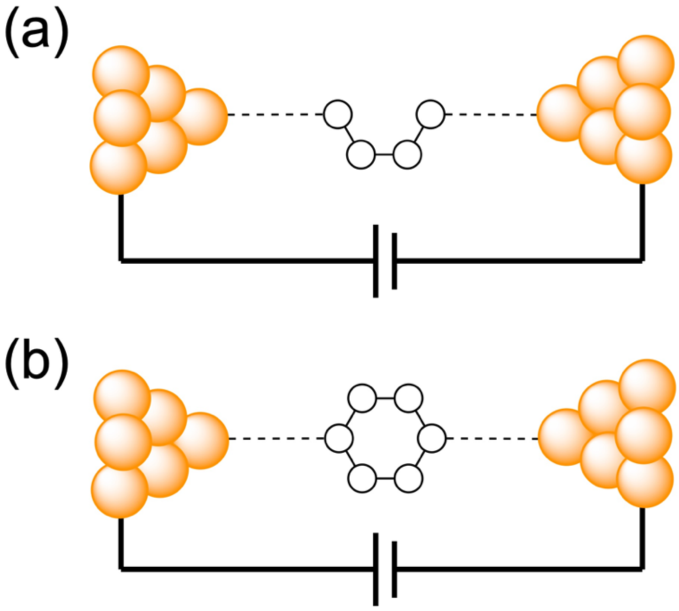

In the parallel circuit on the nanoscale, however, it is known that eq. 3.1 is not consistent with experimental results[32] due to quantum interference, which is caused by the superposition of the phase of the wave function. When the wave functions for electrons passing through different paths, whether in real space or energy space,[33,34] interfere constructively, the conductance of the parallel circuit for the nanoscale material is given by[15,28]

$$g = g_1 + g_2 + 2\sqrt{g_1 g_2} \tag{3.2}$$

where $2\sqrt{g_1 g_2}$ is the cross term coming from the quantum interference. Eq. 3.2 coincides with some experimental results for molecular parallel circuits.[15,16,32] Note that this equation is a simplified form of the original 1999 paper of Magoga and Joachim, where they specifically include more general phase factors, which can be attributed to the trend, whether the transmission is reinforced or weakened as a result of the multiplication of the pathways. Our paper includes an exemplification of such a trend, which itself does not seem to be new; however, as the author will soon see, the author intends in this study to pave the way for correlating this trend with the aromaticity of the ring formed when multiplying the pathways. The author believes this is an unexplored attempt.

In this chapter, the author will see whether or not eq. 3.2 holds true for single molecular junctions whose molecular-graph representations can be deemed to be a parallel circuit.[33,35–45] Zhou et al. have studied the current superposition law based on a layering system consisting of zigzag graphene nanoribbons, finding that when the interlayer distance is shorter than 5 Å, the interference effects between the parallel pathways are not negligible. In our study, on the other hand, the parallelization of the pathways is achieved by forming covalent bonds, not by layering, so our systems are perforce subject to the interference, be it constructive or destructive, which will eventually be correlated with the aromaticity. To this end, the author will use the non-equilibrium Green's function combined with the Hückel method (NEGF–HMO),[20,46] and the density functional theory (NEGF–DFT).[47–50] The author will show that there are some systems whose conductance is not consistent with eq. 3.2. Furthermore, the author will explain these phenomena using the frontier orbital theory[20,23,51–55] and the local transmission contribution.[19]

3.2. Computational Details

All molecular geometries were obtained by optimizing the molecules in gas phase using the B3LYP functional[56,57] and 6-311+G** basis set.[58,59] Au (111) surface was chosen as the electrode. Thiol (-SH) was chosen as the anchor unit to connect the molecules to the contact. The acetylene linker (-C≡C-) was added between the molecular core and the thiol anchor unit to avoid steric hindrance between the bridged molecule and the electrode surface. The terminal hydrogen atom connected with the sulfur atom was removed after optimization. Then, the anchor sulfur atom of the bridged molecule was chemisorbed on the fcc hollow site of the Au (111) surface, which can be modeled by an Au_9 cluster (see Figure 3.1). The bond length between the Au surface and the sulfur atom was taken from the literature.[60] The self-consistent-field-converged Hamiltonian matrix and the overlap matrix for the whole electrode–molecule–electrode structure was obtained from a single-point DFT calculation with the B3LYP functional and the LanL2DZ basis set[61,62] to perform the NEGF calculations within the wide-band-limit (WBL) approximation.[63] In the WBL, a constant value for the LDOS of the Au electrode surface was taken from the literature.[64] These electronic-structure calculations were conducted using Gaussian 09 software package,[65] while the subsequent transmission calculations were performed using ARTAIOS package.[66–68] The Hückel MO distributions were calculated and depicted using HuLiS software package.[69]

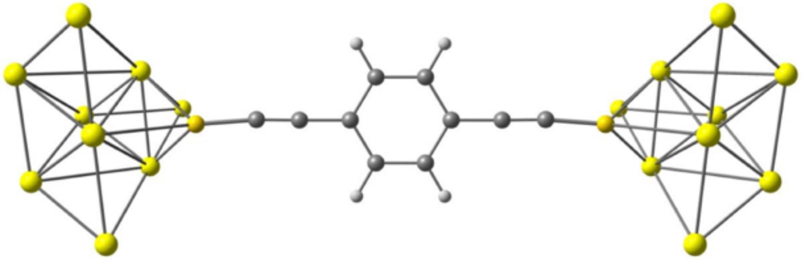

Figure 3.1. Model structure used for transmission calculations with the NEGF–DFT method. Gray, white, yellow, and gold spheres indicate C, H, S, and Au atoms, respectively.

3.3. Results and Discussion

3.3.1. Transmission Calculations for Aromatic and Non-Aromatic Doubled Paths

The author starts off with transport calculations for two sets of molecular systems (see Scheme 3.3). The first model is *cis-transoid* hexatriene and its parallel circuit analogue, *p*-quinodimethane. The second model is the *s-cis* butadiene–benzene system, as has been introduced in Scheme 3.3. In both systems, hexatriene and butadiene have a single path between the end atoms, while *p*-quinodimethane and benzene have two paths. The two models share the same number of paths in a graph theoretic sense. Making the number of paths doubled perforce leads to a ring formation. A macroscopic electric circuit with a circle may result in a circular flow of current and associated magnetic field generation. But that's another story. What matters here in the molecular analogue of the ring circuit is aromaticity.[70] The aromaticity or anti-aromaticity of a cyclic system can be characterized by using the nucleus independent chemical shift (NICS), which is based on the calculated magnetic shielding for the ghost atom at the ring center. [71–73] Generally, negative NICS values correspond to aromaticity, while positive values are associated with anti-aromaticity and values near zero for nonaromatic. *p*-quinodimethane has almost no aromaticity ($\mathrm{NICS(1)_{iso}}$: -1.61 ppm) whereas benzene has a strong aromaticity ($\mathrm{NICS(1)_{iso}}$: -10.2 ppm). It is interesting to note that it has been reported in the literature that aromaticity has a negative correlation with the conductance in some specific connection modes.[74–77]

Scheme 3.3. Kekulé structures of the four molecules investigated in this study. Arrows show the connection point with the electrode.

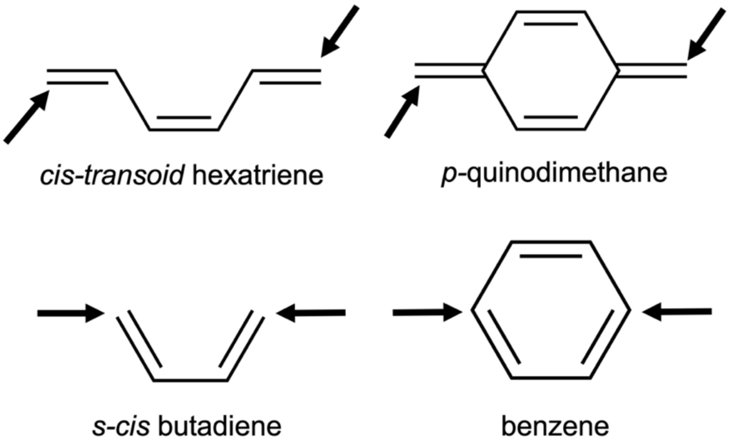

Figures 3.2 and 3.3 show the transmission spectra calculated for the systems shown in Scheme 3.3 with the NEGF–HMO and the NEGF–DFT methods. As shown in these figures, the NEGF–HMO method appears to be reliable enough because the NEGF–HMO results show the same tendency as the NEGF–DFT ones. Therefore, the author will henceforth focus our attention to the results of the NEGF–HMO calculations.

In Figure 3.2a, the transmission probability of *p*-quinodimethane at the Fermi energy is 3.9 times higher than that of hexatriene. The ratio calculated with the DFT is reduced to 3.3. However, by and large, the relation between the transmission probabilities of hexatriene and *p*-quinodimethane is in good agreement with what is expected from eq. 3.2.[78] On the other hand, the transmission probability of benzene at the Fermi energy is found 4 times lower than that of butadiene at the Hückel level. The same is true for the DFT calculation, though the ratio is reduced to 1.6. In contrast to the case of hexatriene vs. *p*-quinodimethane, eq. 3.2 cannot explain the tendency of the transmission probability in the case of butadiene vs. benzene. Sadeghi et al. pointed out the reduction of the conductance in a cyclic system compared to its single-path linear counterpart considering the paths simply as classical waveguides and attributing an impedance mismatch to the cause.[37]

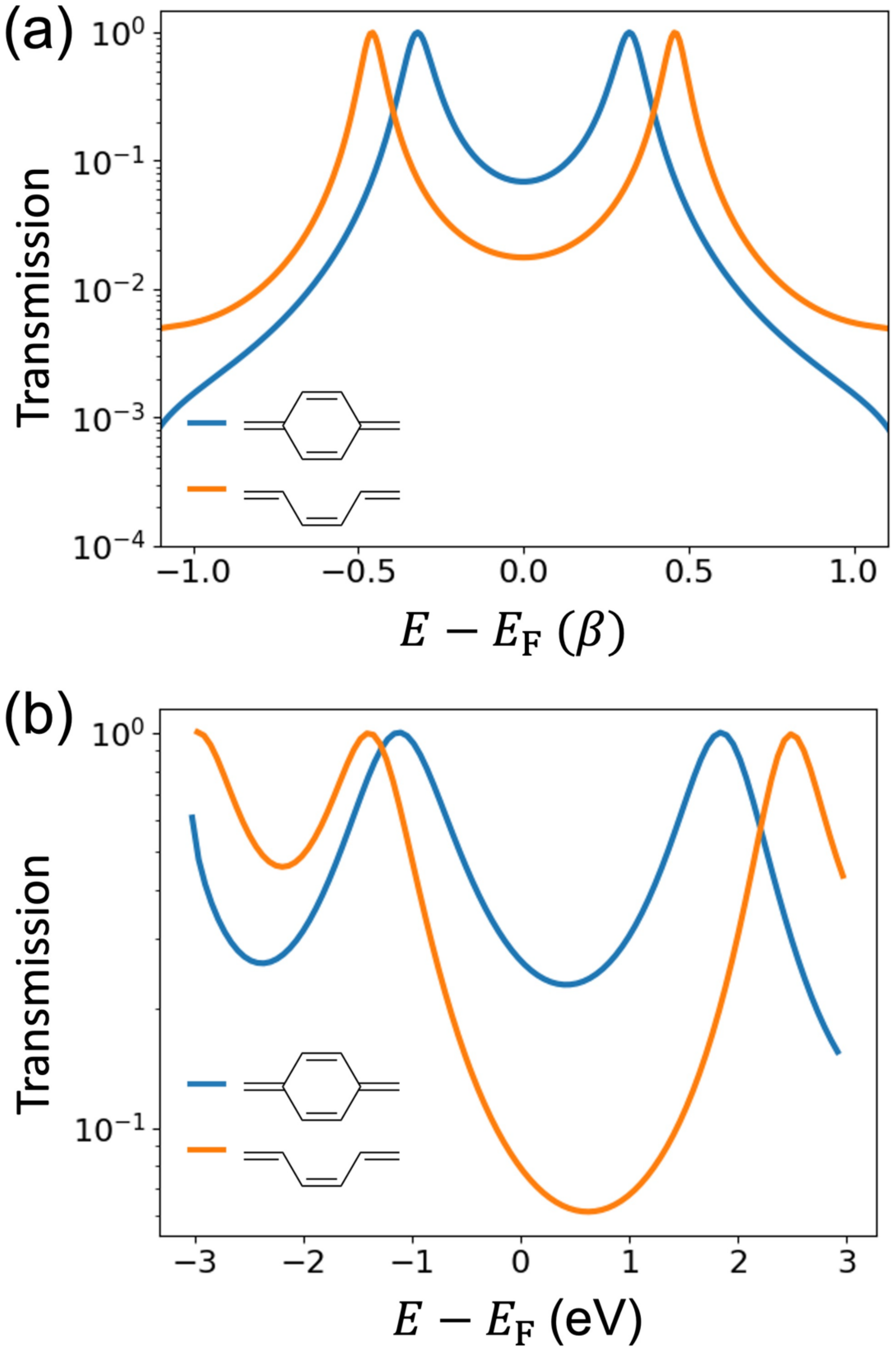

Figure 3.2. Transmission spectra for *p*-quinodimethane (blue line) and hexatriene (orange line). The spectra in (a) were calculated by using the NEGF–HMO and those in (b) were calculated by using the NEGF–DFT.

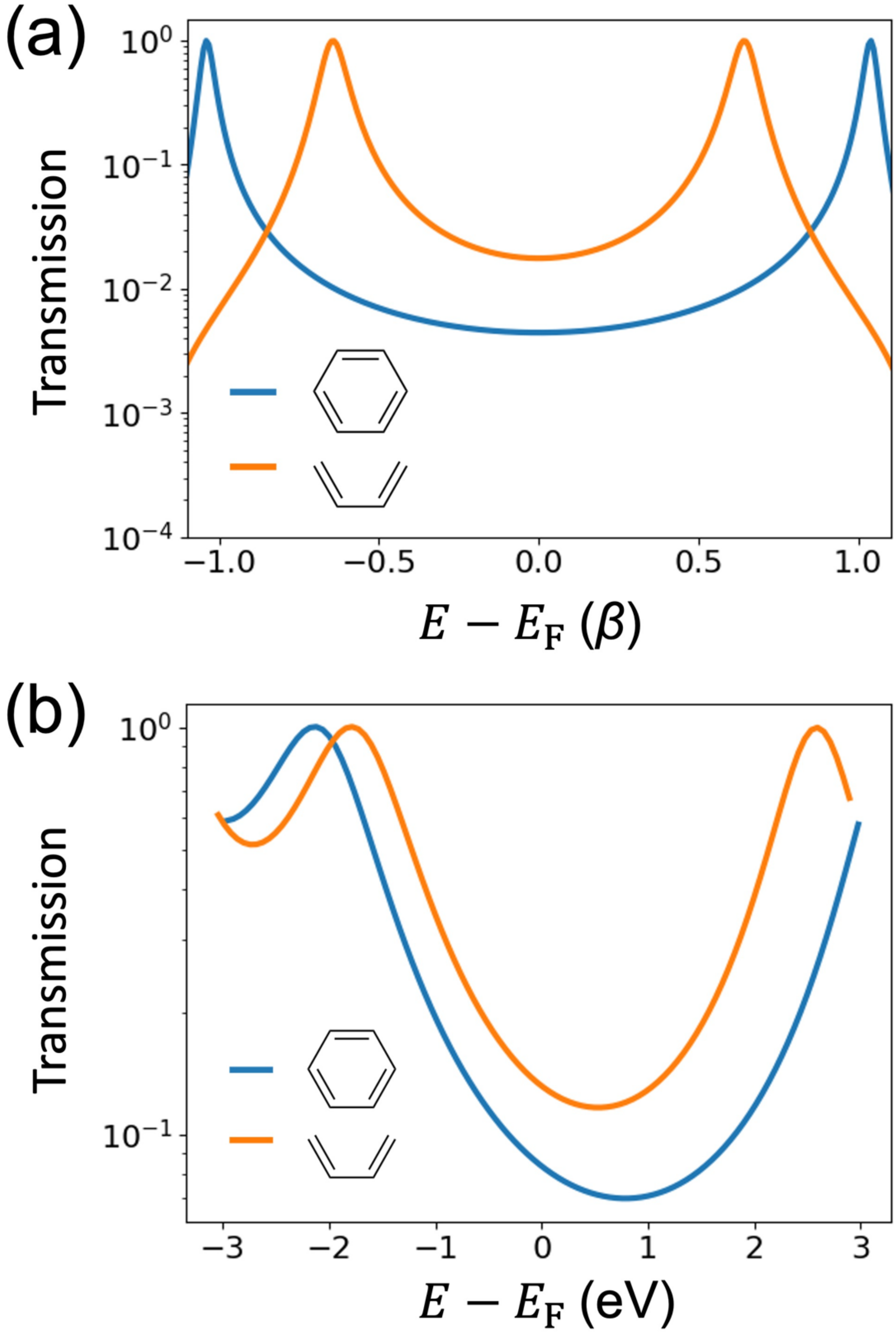

Figure 3.3. Transmission spectra for benzene (blue line) and butadiene (orange line). The spectra in (a) were calculated by using the NEGF–HMO and those in (b) were calculated by using the NEGF–DFT.

3.3.2. Frontier Orbital Analysis for Aromatic and Non-Aromatic Doubled Paths

Let us consider why benzene has a lower conductivity compared to butadiene, though the number of conductive paths is one in butadiene but that is two in benzene. By decreasing the absolute value of the Hückel Hamiltonian elements corresponding to the bonds highlighted by the red color in Scheme 3.4, one can easily move from the double-path model to the single-path model gradually and continuously. Figure 3.4 shows the relation between the resonance integral β' for the bonds highlighted by red and transmission probability at the Fermi energy, and that between β' and the HOMO–LUMO gap. In the case of *p*-quinodimethane, the HOMO–LUMO gap gets smaller as the value of β' gets larger. Note that the limit of $\beta' \to 0$ corresponds to the model of hexatriene. As the transition from hexatriene to *p*-quinodimethane proceeds, the transmission probability becomes larger because the contribution of the HOMO and LUMO to the absolute value of the Green's function becomes larger as indicated by eq. 2.25. On the other hand, the HOMO–LUMO gap of benzene becomes larger as β' becomes larger. Therefore, the transmission probability becomes smaller as the model system gets closer to benzene from butadiene. The tendency of the change of transmissions through these models is also in line with the change of the MO expansion coefficients in the HOMO and LUMO on the C atoms in contact with the electrodes, namely the numerators of eq. 2.25 (see Figure 3.5).

Scheme 3.4. Kekulé structures of *p*-quinodimethane and benzene. β' denotes the resonance integral for the bonds highlighted by red color (see the text for details).

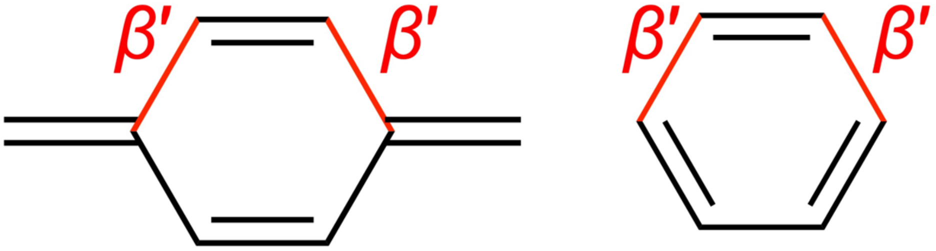

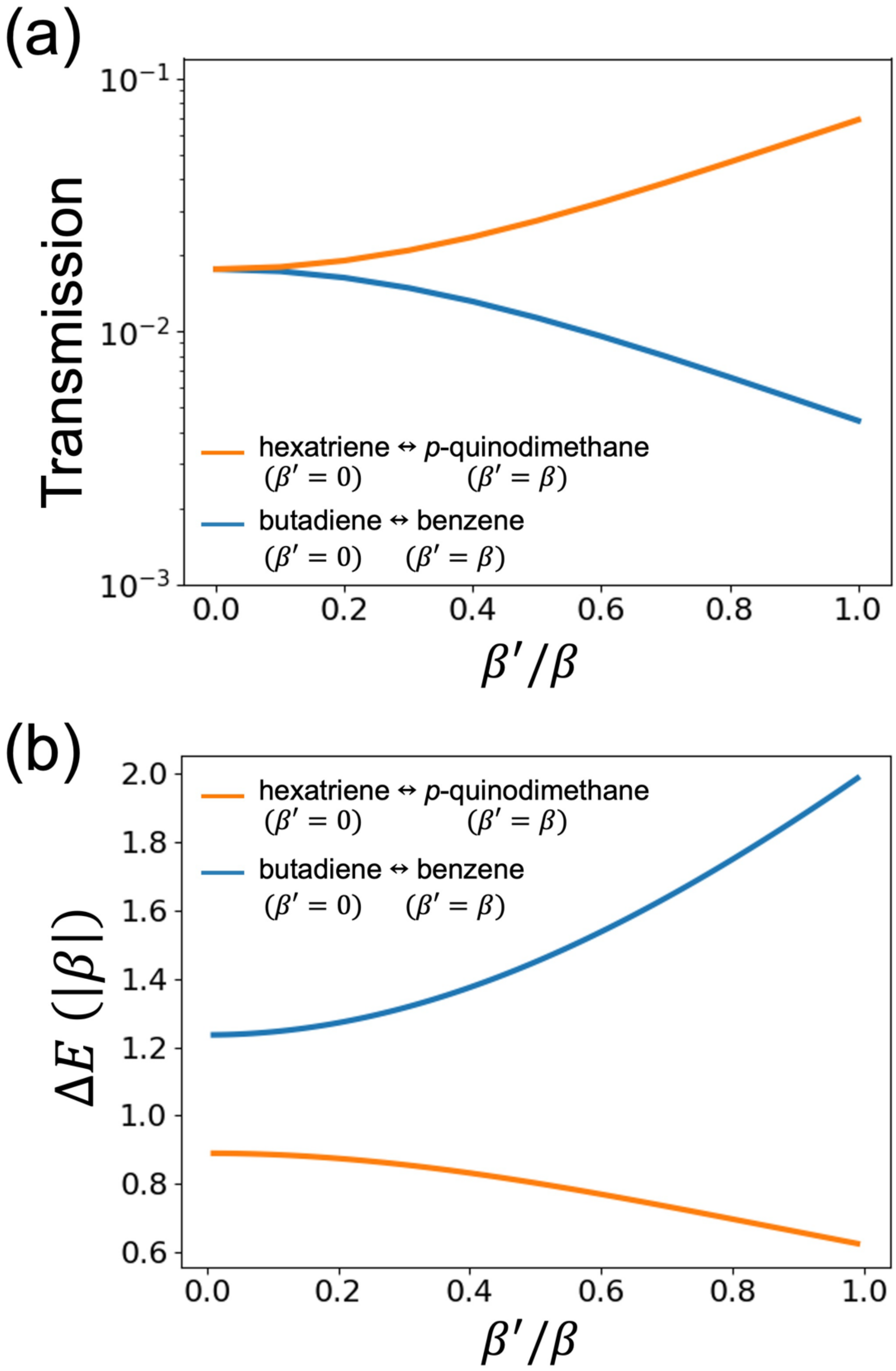

Figure 3.4. (a) Transmission probability at the Fermi level as a function of β’ for the bonds highlighted by red color in Scheme 3.4 and (b) the HOMO–LUMO gap energy depending on β’.

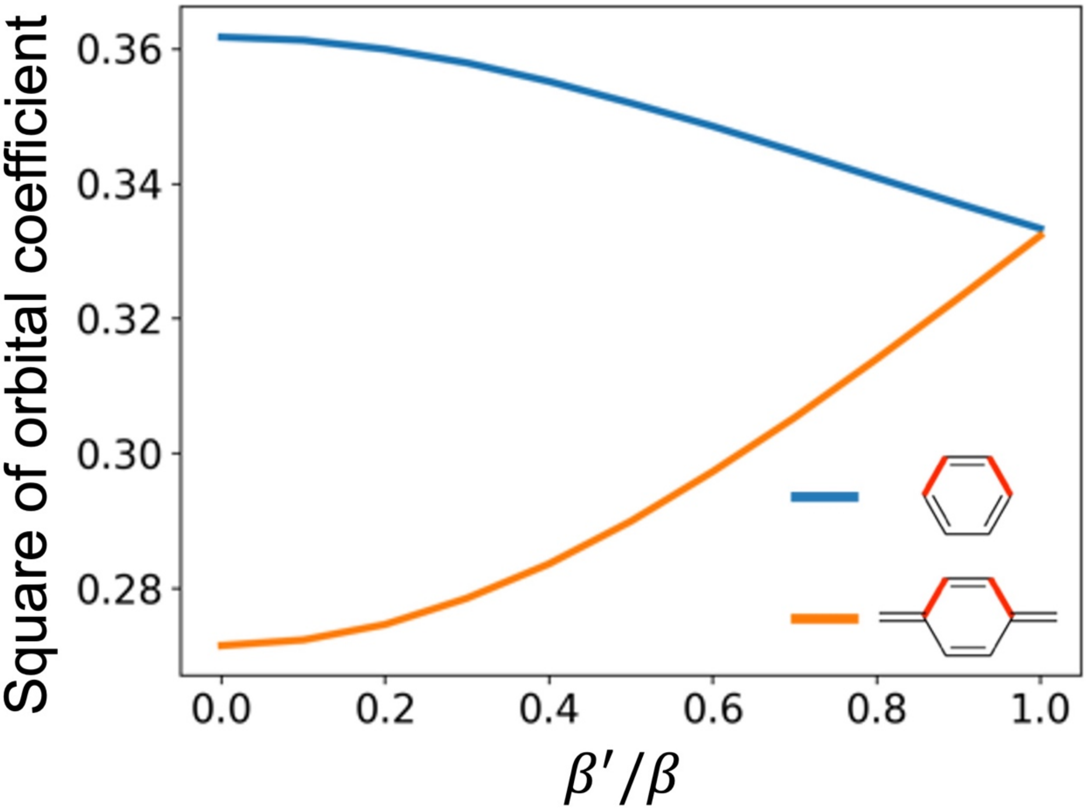

Figure 3.5. The square of molecular orbital coefficients for the atom connected with the electrode depending on β’. β’ denotes the resonance integral for the bonds highlighted by red color. In the two systems, the absolute values of the HOMO and LUMO coefficients are equal because the molecules considered here are alternant hydrocarbons. On top of that, the two electrode attachment sites are symmetrically identical. Therefore, it is only necessary to square one of the orbital coefficients of one molecular orbital.

These tendencies between the HOMO–LUMO gap and β′ beg for an explanation. The author uses the perturbational molecular orbital (PMO) methods in what follows.[79–81] In the case of *p*-quinodimethane, which can be virtually divided into hexatriene and ethylene parts (see Figure 3.6), the energy of the HOMO of *p*-quinodimethane is pushed up because the HOMO of hexatriene interacts with the HOMO of ethylene in an anti-bonding manner. In contrast, the energy of the LUMO of *p*-quinodimethane is pushed down because the LUMO of hexatriene interacts with the LUMO of ethylene in a bonding manner. Thus, the HOMO–LUMO gap of *p*-quinodimethane gets smaller compared to that of hexatriene.

Benzene may be thought of as being divided into butadiene and ethylene parts (see Figure 3.7). Note that benzene has two degenerate HOMOs and LUMOs. They are denoted as HOMO1 and HOMO2, and LUMO1 and LUMO2. The LUMO of butadiene is pushed up, resulting in the LUMO1 of benzene, as a result of the anti-bonding interaction with the HOMO of ethylene. The bonding counterpart results in the HOMO2 of benzene, whose energy coincides with the HOMO energy of ethylene because there is a nonnegligible out-of-phase contribution from butadiene's HOMO-1. Similarly, the HOMO of butadiene interacts with the LUMO of ethylene so that the resultant orbitals split into the bonding orbital (HOMO1) and the anti-bonding orbital (LUMO2). The in-phase contribution from butadiene's LUMO+1 to the LUMO2 makes it have the same energy as the parent LUMO of ethylene. This is why the HOMO–LUMO gap of benzene is larger than that of butadiene. Such an enlargement of the HOMO–LUMO gap has something to do with the benzene aromaticity.

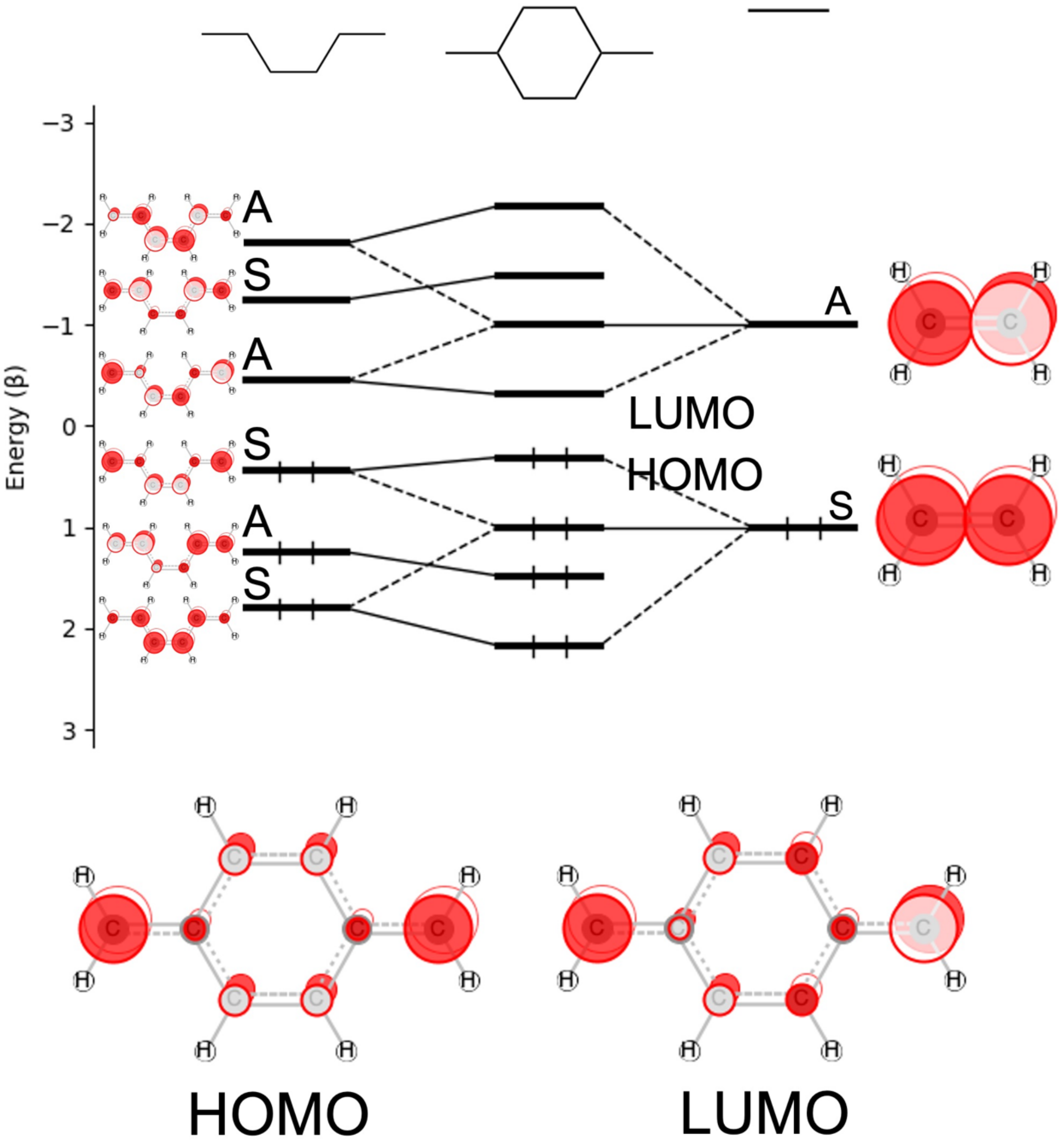

Figure 3.6. Orbital interaction diagram for *p*-quinodimethane partitioned into hexatriene and ethylene parts. S and A, respectively, indicate that the orbital is symmetric and antisymmetric with respect to the mirror plane that is perpendicular to the molecular plane, bisecting the molecule.

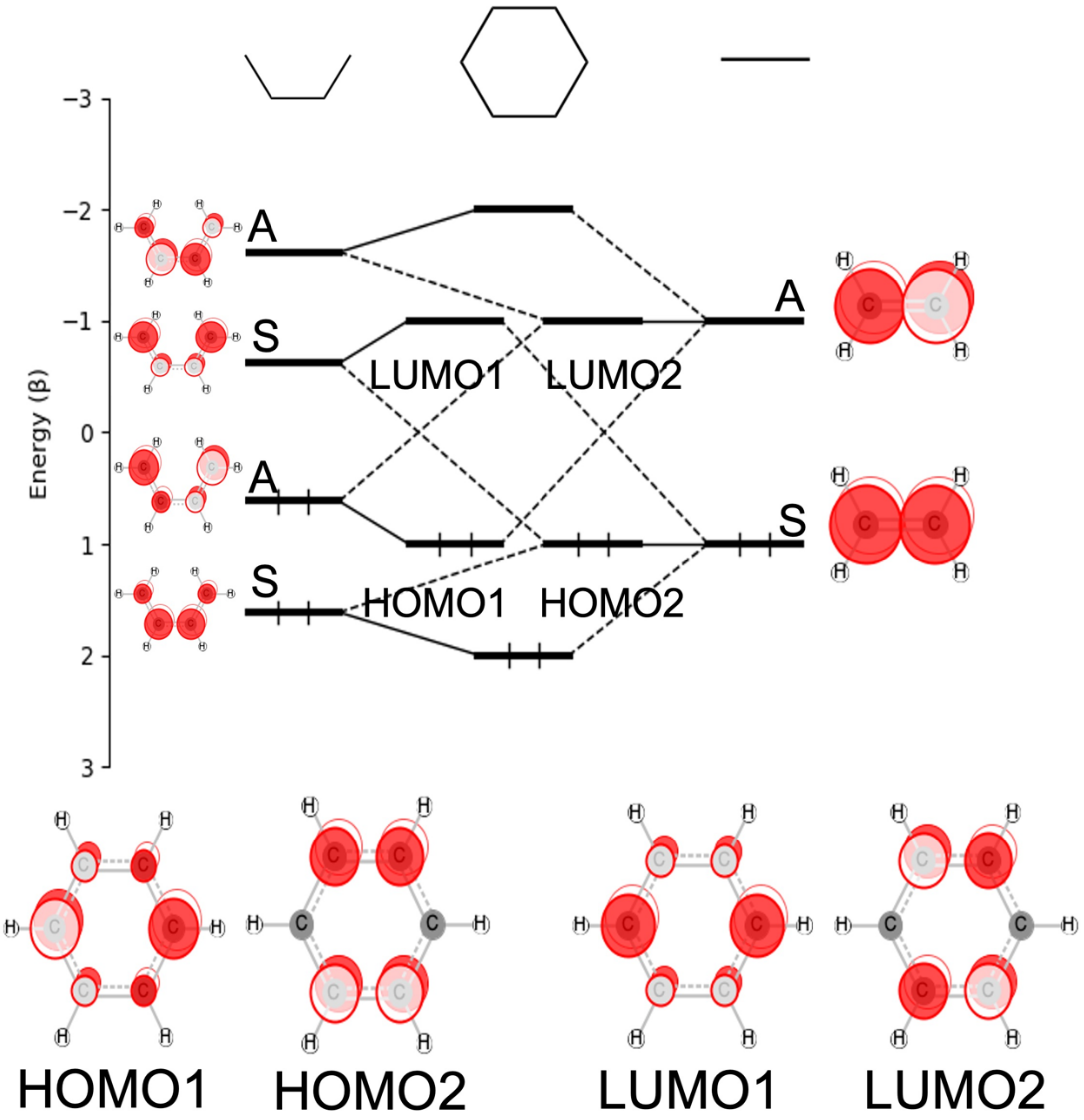

Figure 3.7. Orbital interaction diagram for benzene partitioned into butadiene and ethylene parts. S and A, respectively, indicate that the orbital is symmetric and antisymmetric with respect to the mirror plane that is perpendicular to the molecular plane, bisecting the molecule.

Let us consider the reason why the two cases have different orbital interaction patterns based on the orbital symmetry approach.[82] The frontier orbitals of the planar π conjugated molecules investigated here have two symmetry operations, i.e., the two-fold axis C_2 in the plane of the molecule, and the vertical mirror plane σ_v including the C_2

axis. In this study, the author deals only with σ_v for symmetry consideration. When the two orbitals interact, the symmetry of each orbital must be the same. Therefore, two patterns of interaction occur, namely, the pattern of HOMO–HOMO and LUMO–LUMO interactions, and that of HOMO–LUMO interactions. The HOMO–HOMO and LUMO–LUMO interactions occur when the HOMOs of the two interacting molecular parts are symmetric (S) and their LUMOs are antisymmetric (A). And it is also true if the symmetry is switched between the HOMO and LUMO. The HOMO–LUMO interactions occur when the symmetry of both of the HOMO of one fragment and the LUMO of the other fragment is S or when both of them are labelled A.

In the case of the combination of the HOMO–HOMO interaction and the LUMO–LUMO interaction, the energy of the HOMO generated after the interaction is pushed up, while the energy of the LUMO is pushed down, so the energy gap gets smaller. By contrast, in the case of the HOMO–LUMO interactions, the energy of the HOMO generated after the interaction is pushed down, while the energy of the LUMO is pushed up, so the energy gap gets larger.

Since the HOMO of the ethylene fragment has the S symmetry while the LUMO has the A symmetry, the type of the interaction is determined by the symmetry of the frontier orbitals of the other fragment. In the case of *p*-quinodimethane, since the HOMO and LUMO of hexatriene with six 2pπ orbitals are labeled S and A, respectively, these interactions between the hexatriene and ethylene fragments result in the HOMO–HOMO and LUMO–LUMO interactions. In the case of benzene, on the other hand, the HOMO and LUMO of the butadiene fragment with four 2pπ orbitals are labeled A and S, respectively. Note that the symmetry species are switched compared to hexatriene. Thus, the interactions between the butadiene and ethylene fragments lead to the HOMO–LUMO interaction. From these results, one could say that whether the HOMO–HOMO and LUMO–LUMO interactions or the HOMO–LUMO interactions take place depends on the symmetry of the HOMO and LUMO of butadiene and hexatriene, which can be further traced back to how many π orbitals or conjugated carbon atoms are included in the molecule.[83]

The author can understand the trend of the variation in conductance for a series of five-membered heterocycles, which has been discussed in the literature,[74–76] in the context of the increasing number of paths. The conductance of a heterocyclic compound can be compared to that of butadiene (see Scheme 3.5). In the heterocycle, the connection between the two end contact points is reinforced by the introduction of the X–mediated path. The conductance changes depending on the X atom. When the heterocycle is aromatic in such cases as X = O and S, the conductance is generally lower than the single-path analogue, butadiene.[74–76] This situation is very akin to the benzene–butadiene case.

Scheme 3.5. Comparison between butadiene and five-membered heterocycle junctions. Arrows show the connection point with the electrode.

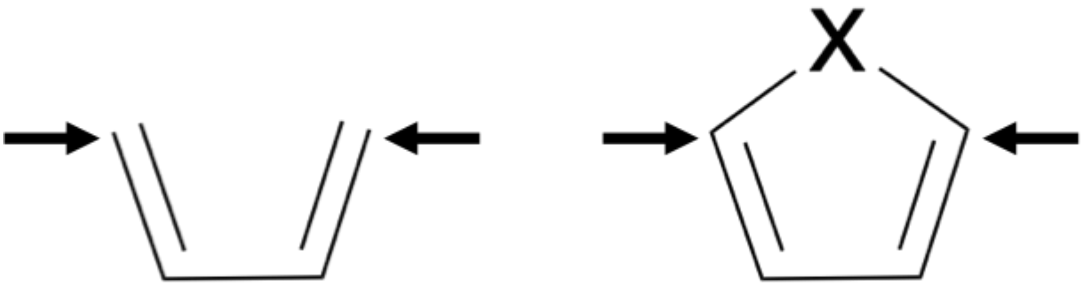

3.3.3. Circuit Whose Conductance Does Not Vary with the Number of Paths

Next, the author turns to a model in which its aromaticity is almost kept intact during the process of increasing the number of paths (see Scheme 3.6). Biphenyl appears to serve as a good model to probe this. Originally, in biphenyl, two phenyl rings are separated by a single path, but reinforcing the connection between them with an ethylene linker results in phenanthrene. This process would be repeated on the other side so that one could arrive at pyrene. However, it should be noted that the resonance hybrid of the phenyl rings in the original biphenyl molecule does not seem to change in the above-mentioned transmutation of the model.

Scheme 3.6. Kekulé structures of biphenyl, phenanthrene, and pyrene. Arrows show the connection point with the electrode.

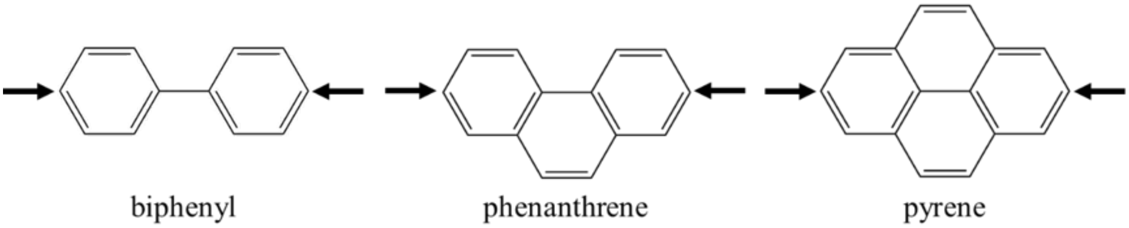

Figure 3.8 shows the transmission spectra for biphenyl, phenanthrene, and pyrene. In this figure, one can see that the transmission probability remains almost unchanged even if another path is added, which is different from the cases of the *p*-quinodimethane-hexatriene and benzene-butadiene systems.

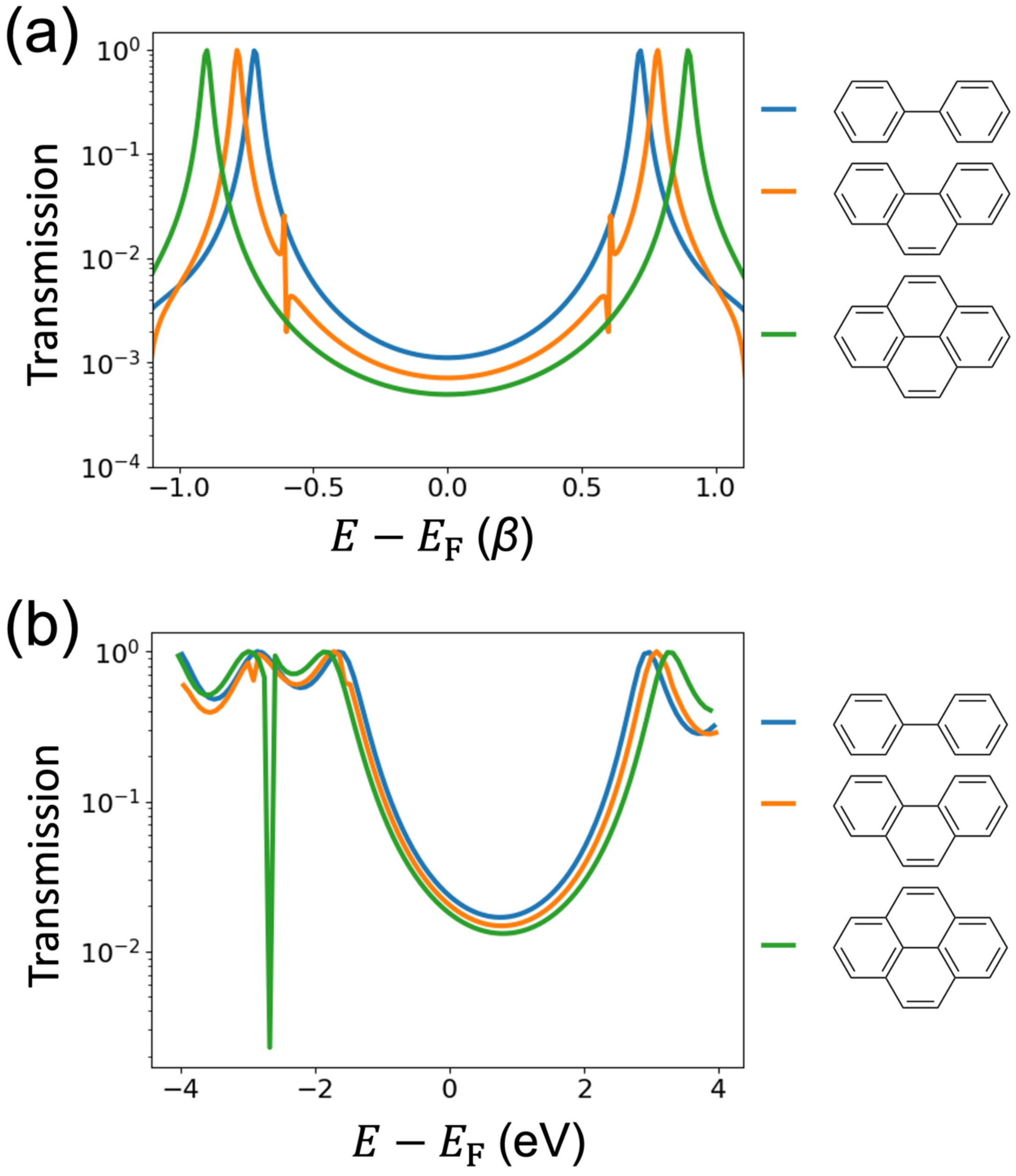

Figure 3.8. Transmission spectra for biphenyl (blue), phenanthrene (orange), and pyrene (green) calculated with (a) the NEGF–HMO and (b) the NEGF–DFT methods.

To justify the observed results, the author carried out the local transmission calculation,[19] which is a convenient technique to make it possible to decompose the total transmission into local atom-to-atom contributions. In this method, the total transmission can be decomposed into local (atomic) contributions as follows:

$$T(E) = \sum_{\mathrm{A} \in \mathrm{L}, \mathrm{B} \in \mathrm{R}} T_{\mathrm{AB}}(E) \tag{3.3}$$

where $T_{\mathrm{AB}}(E)$ is the transmission probability for electrons with the energy of E passing from the center A on the left side to the center B on the right side. Note that A and B are usually atoms, which are defined by the basis functions centered on them after a symmetric (Löwdin) orthogonalization. T_{AB} can be calculated on the basis of the Hamiltonian and overlap matrices that are obtained from a self-consistent field calculation.

Figure 3.9 shows the calculated local transmission plots for biphenyl, phenanthrene, and pyrene. The plot for phenanthrene indicates that another pathway is added, but any arrow does not proceed through the added pathway. The pyrene case also indicates that even if yet another pathway is added, any other arrow still does not proceed through the added pathways. The reason for this is that biphenyl has a bond between phenyl rings in the para position to the carbon atom connected with the source electrode, but the additional pathways in phenanthrene and pyrene exist in the meta position (see Scheme 3.7).[84] Therefore, in this system, transmission probability hardly changes even though the number of paths connecting two end electrodes is increased. For completeness, local transmission plots for butadiene, hexatriene, benzene, and *p*-quinodimethane have been calculated (see Figures 3.10 and 3.11).

Scheme 3.7. Selectivity of transport pathway in benzene. Blue arrows indicate the allowed pathway, while the red arrow indicates the forbidden one.

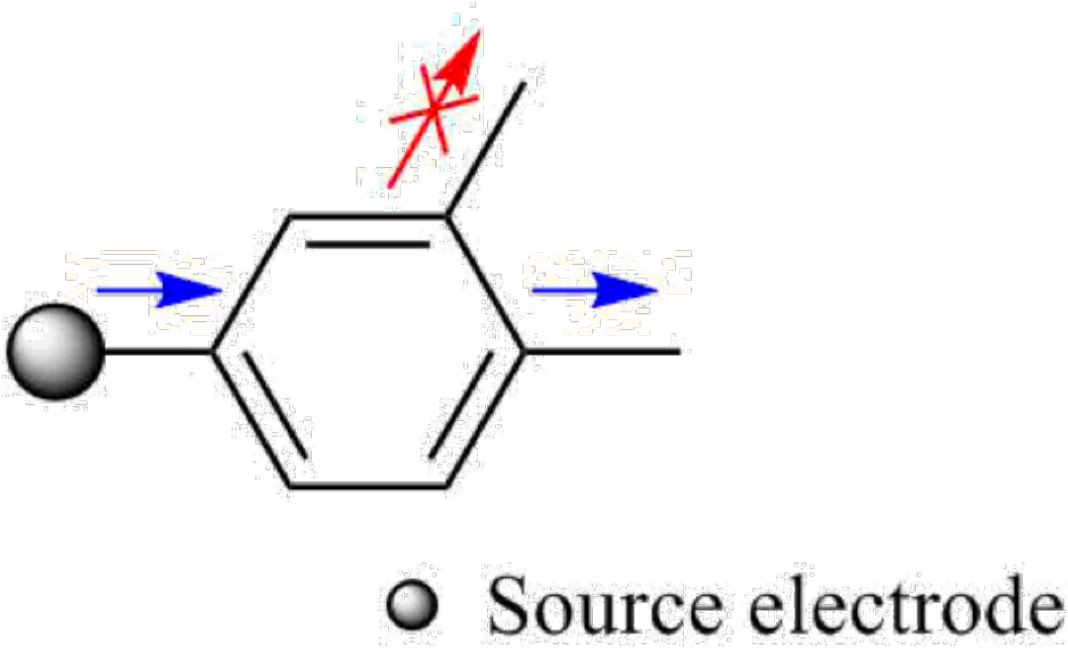

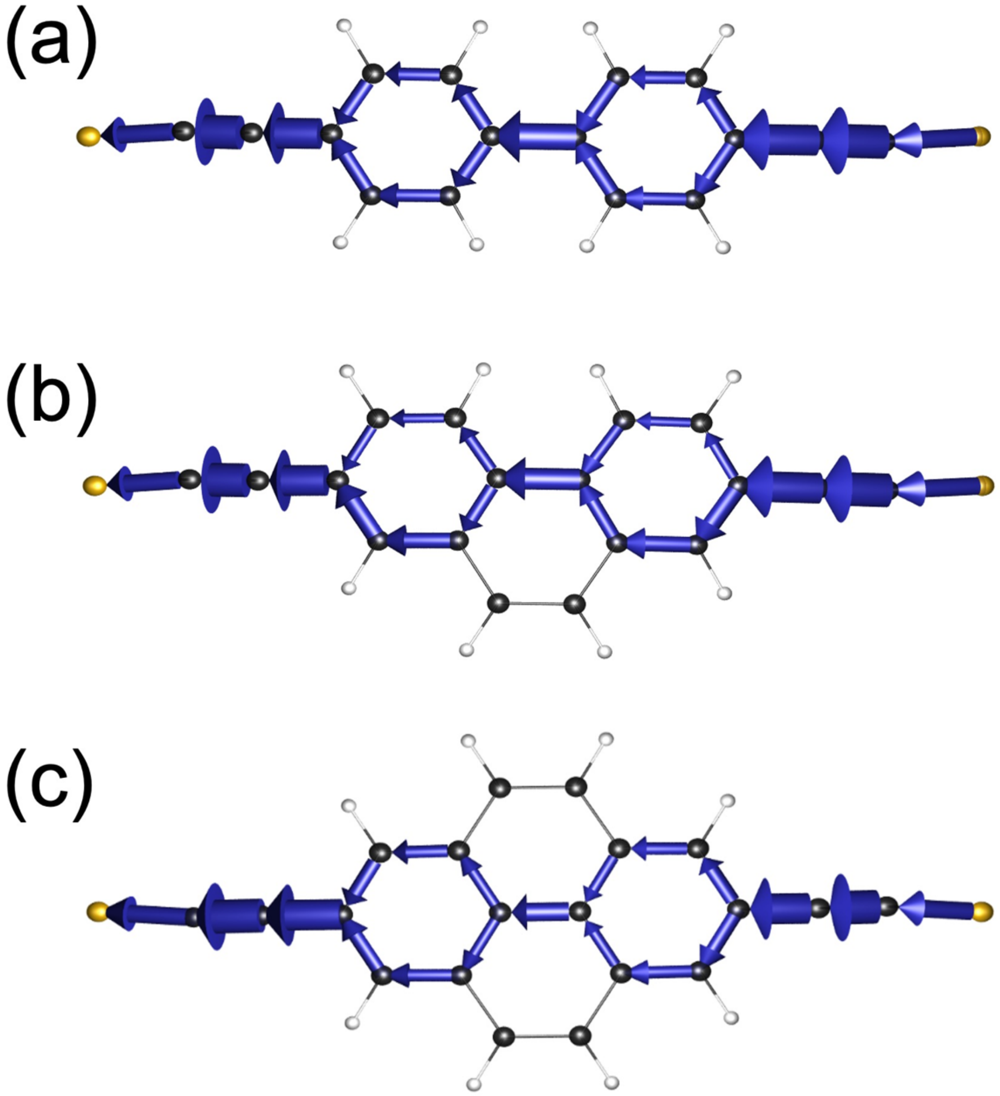

Figure 3.9. Local transmission contributions in (a) biphenyl, (b) phenanthrene, and (c) pyrene evaluated at the Fermi level. Black, white, and gold balls denote C, H, and S atoms, respectively. The thickness of the arrows is proportional to the magnitude of contribution to the total transmission. The local transmission contributions are depicted only if they are above a threshold value of 0.1.

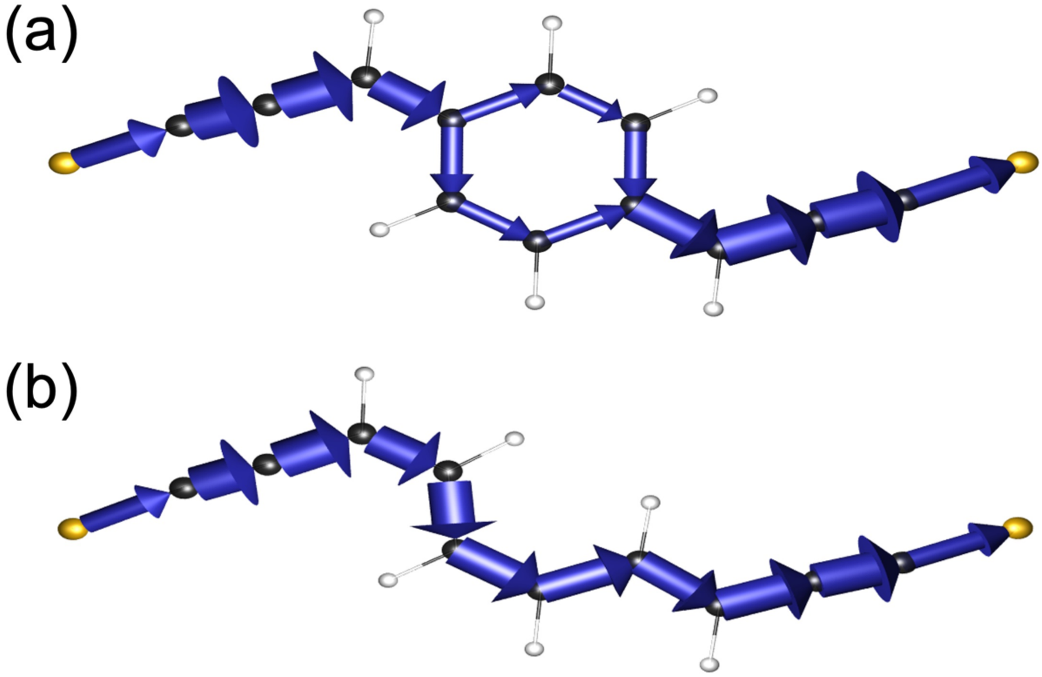

Figure 3.10. Local transmission contributions for (a) *p*-quinodimethane and (b) hexatriene at the Fermi level.

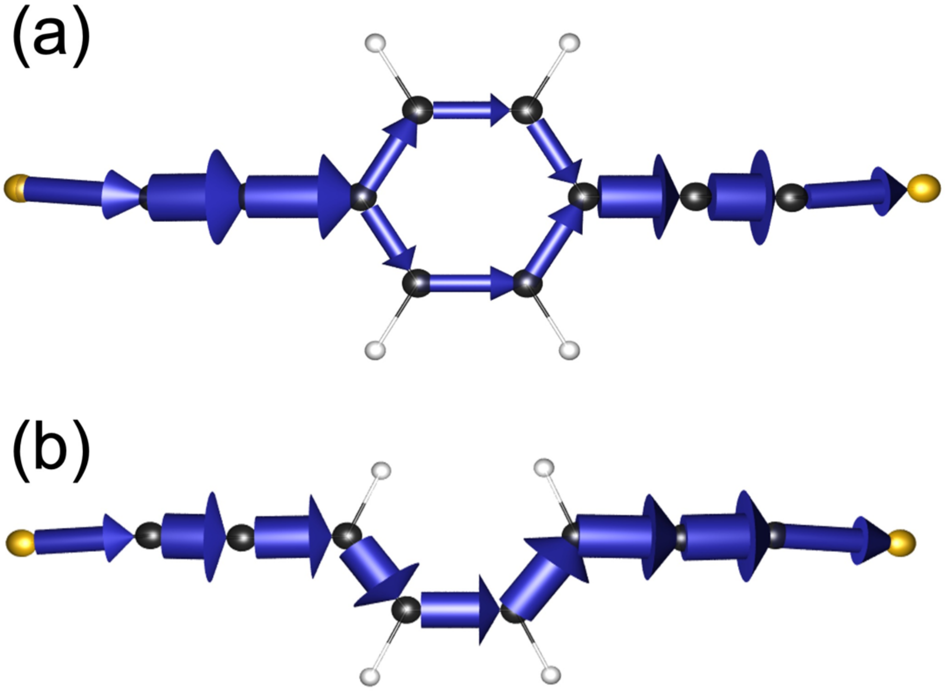

Figure 3.11. Local transmission contributions for (a) benzene and (b) butadiene at the Fermi level.

3.3.4. Conductance of Anti-Aromatic Parallel Circuits

The author has consistently described the decrease in conductance due to aromaticity. It would be natural that one should wonder what the transmission change would look like in the case where an anti-aromatic compound is generated in the ring formation upon the parallelization of the molecular graph circuit. The author considers allyl radical, whose parallel circuit analogue is cyclobutadiene, a typical anti-aromatic molecule (see Scheme 3.8). The author is aware of the instability of these molecules, but this thought experiment approaching a limit will lead us to a fruitful result, as one can see later.

Scheme 3.8. Kekulé structures of allyl radical and cyclobutadiene. Arrows show the connection point with the electrode.

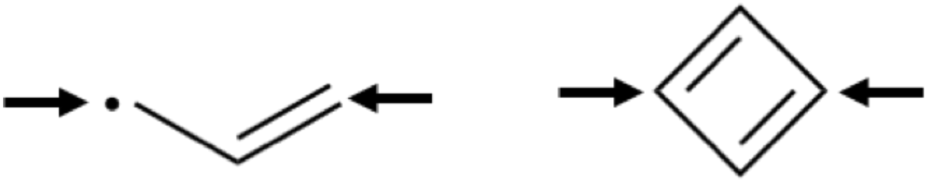

Figure 3.12 shows the transmission spectra for cyclobutadiene and allyl radical. The allyl radical and cyclobutadiene have one and two non-bonding MOs (NBMOs) at the Fermi level, respectively. Since $E_\mathrm{F} - \epsilon_\mathrm{k}$ becomes zero in the denominator of eq. 2.24, the singularity is observed at $E = E_\mathrm{F}$. Thus, the electron transmission probability of both allyl radical and cyclobutadiene at the Fermi level is as high as 1.[85]

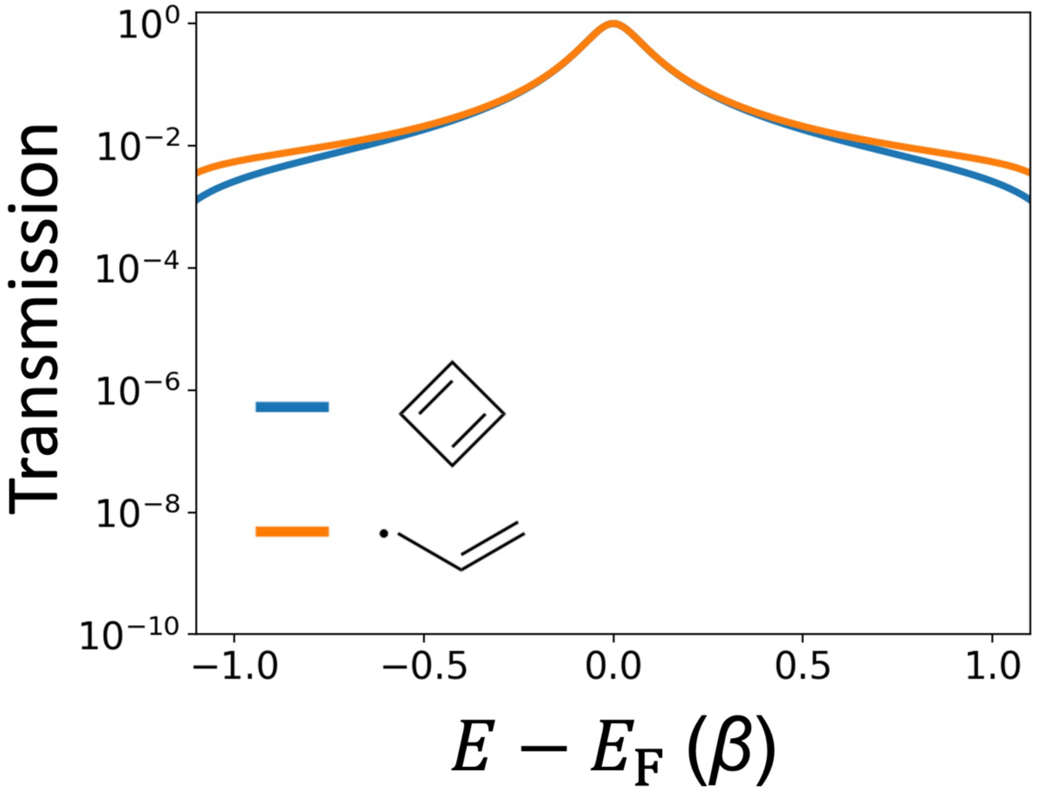

Figure 3.12. Transmission spectra for cyclobutadiene (blue line) and allyl radical (orange line) calculated by using the NEGF–HMO.

It is known that the anti-aromatic molecules including cyclobutadiene have high conductivity.[86,87] The author will consider a more general case of [4n] annulene, a series of anti-aromatics (see Scheme 3.9 for its graph theoretic representation). The filled nodes are supposed to be connected with the electrodes so that one can see two paths between the two nodes. From this model, one can generate a single path subgraph terminated by the two filled nodes. The number of nodes or carbon atoms in this chain is denoted as m_1, while that in the other subgraph is m_2. The relation between m_1 and m_2 is clear: $m_2 = m_1 - 2$. The longer and shorter subgraphs represent linear C_{m_1} and C_{m_2} chains, respectively.

Since the total number of nodes in the ring is 4n, a little of algebra leads to $m_1 = 2n + 1$ and $m_2 = 2n - 1$. It is clear that m_1 and m_2 are odd numbers, so both shorter and longer linear chains have an NBMO at the Fermi level.

The MO diagrams for π-conjugated linear carbon chains are shown in Figure 3.13. When one moves from the lowest MO level to the highest, one can see an alternation of the symmetry species. The *k*th MO has the symmetry of A if *k* is an even number; otherwise, it has the symmetry of S. Since the $\frac{1}{2}(m+1)$th orbital corresponds to the NBMO, the *n*th and (*n*+1)th orbitals are the NBMOs in the C_{m_2} and C_{m_1} chains, respectively. If *n* is even, the NBMOs of the C_{m_2} and C_{m_1} chains have the A and S symmetries, respectively; otherwise, the symmetries are switched. What is important is that they do not share the same symmetry, so they cannot interact with each other upon the ring formation. NBMO levels stay at the Fermi level, be they linear or cyclic, resulting in a singularity in the transmission spectrum at the Fermi level regardless of the number of paths available between the two connection nodes. Thus, the transmission probability remains unity before and after the parallelization.

Scheme 3.9. Molecular graph of a ring with antiaromaticity and its two fragments. m_1 and m_2 represent the number of nodes in each fragment. Filled nodes denote where the electrode is attached.

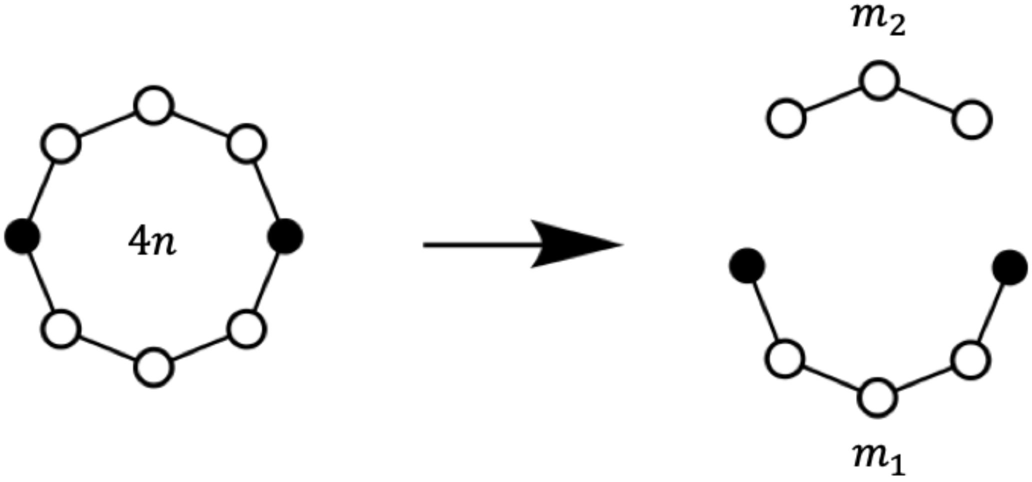

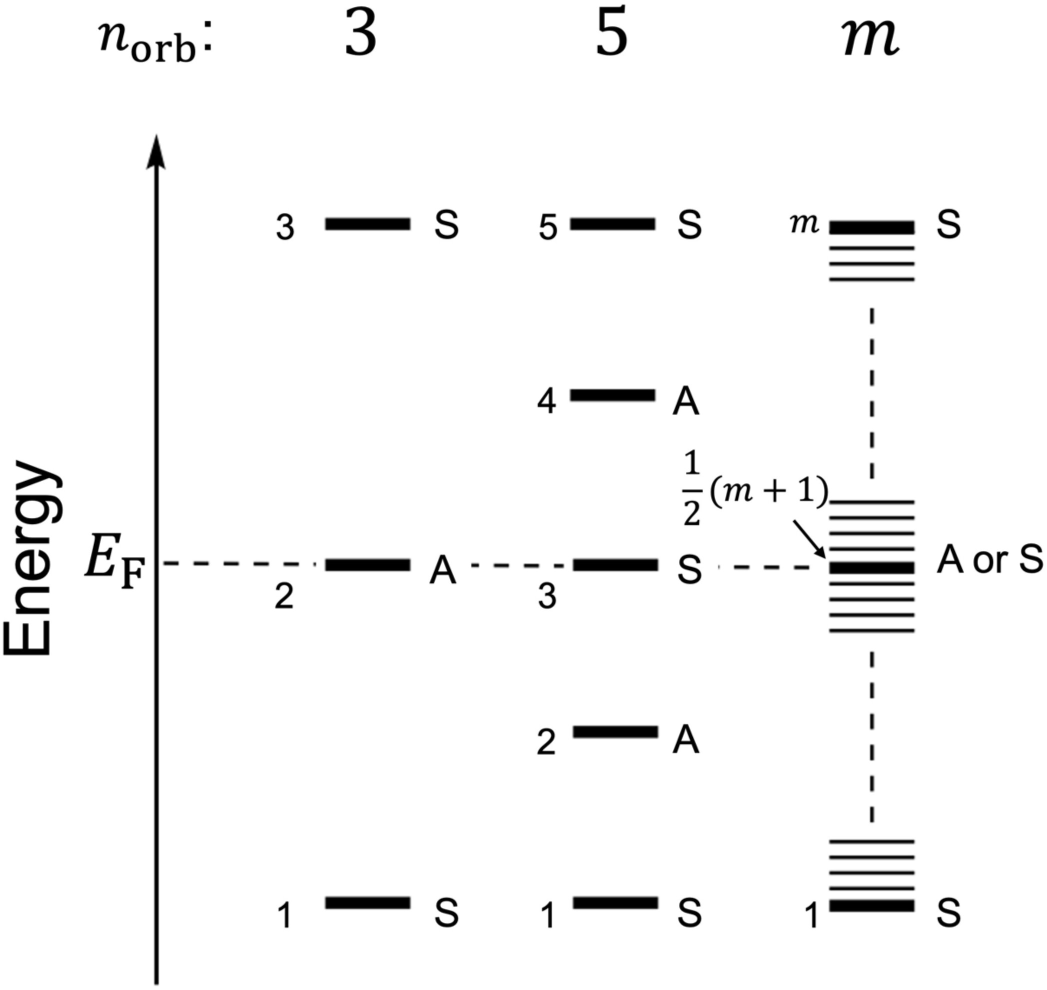

Figure 3.13. MO level diagram of π-conjugated molecules with an odd number of carbon atoms.

3.4. Conclusions

In this study, the author investigated the relation between the number of graph theoretic paths and conductance by using the Green's function methods combined either with Hückel or DFT. When the number of paths increases, the change in conductance can be classified into three cases: in the first case, the conductance increases, as expected and exemplified by the hexatriene–*p*-quinodimethane system; in the second case, the conductance decreases, as unexpected and exemplified by the benzene–butadiene system; and the last but not least, there are cases where the conductance remains unchanged, as demonstrated by using the biphenyl–phenanthrene–pyrene as well as allyl radical–cyclobutadiene systems. In the systems where the conductance changes, whether increasing or decreasing, the author carried out a PMO analysis with *p*-quinodimethane divided into hexatriene and ethylene fragments and with benzene divided into butadiene and ethylene fragments. The PMO analysis has revealed that the HOMO–HOMO and LUMO–LUMO interactions between the fragments cause an increase in conductance, while the HOMO–LUMO interaction causes a decrease in conductance. Since the symmetry of the ethylene's HOMO is S and its LUMO is A, the interaction pattern, whether the HOMO–HOMO and LUMO–LUMO interactions or the HOMO–LUMO interaction, is determined by the symmetry of the frontier orbitals of the other fragment. In the biphenyl–phenanthrene–pyrene system, the author performed a local transmission analysis. This method has elucidated that even if a path is added, the current flow is unlikely to pass through the added path because of the path selectivity of electron transfer. Anti-aromatic molecules can be formed by combining two linear molecules which are composed of an odd number of conjugated carbon atoms. The electron transmission probabilities of both the anti-aromatic molecule and the two constituent linear molecules are unity at the Fermi level due to the presence of NBMO levels at the corresponding energy region. Thus, in the allyl radical–cyclobutadiene system, the conductance can be said to remain unchanged even if the number of paths increases.

3.5. Appendix

3.5.1. Resistance Distance

The resistance distance is a measure of the topological distance between two nodes in a graph.[30,31] When the edges of the graph with n nodes is replaced by unit resistors, the resistance distance between the two nodes i and j, $(\mathbf{\Omega})_{ij}$, is given by

$$(\mathbf{\Omega})_{ij} = (\mathbf{L})^{-1}_{ii} + (\mathbf{L})^{-1} - 2(\mathbf{L})^{-1}_{ij} \tag{A3.1}$$

where **L** is the Laplacian matrix of the graph. The Laplacian matrix is defined as follows:

$$\mathbf{L} = \mathbf{D} - \mathbf{A} \tag{A3.2}$$

where $\mathbf{D} = \mathrm{diag}(d_1, \cdots, d_n)$ is the degree matrix and **A** is the adjacency matrix. The ith element of the degree matrix is the number of graph edges which connect the ith node. Let us take butadiene as an example (see Scheme 3.2 for the atom numbering), the adjacency matrix and the degree matrix are, respectively, given by

$$\mathbf{A} = \begin{pmatrix} 0 & 1 & 0 & 0 \\ 1 & 0 & 1 & 0 \\ 0 & 1 & 0 & 1 \\ 0 & 0 & 1 & 0 \end{pmatrix}, \text{and } \mathbf{D} = \begin{pmatrix} 1 & 0 & 0 & 0 \\ 0 & 2 & 0 & 0 \\ 0 & 0 & 2 & 0 \\ 0 & 0 & 0 & 1 \end{pmatrix} \tag{A3.3}$$

In Eq. A3.3, the Laplacian matrix and the inverse matrix of **L** are, respectively, given by

$$\mathbf{L} = \begin{pmatrix} 1 & -1 & 0 & 0 \\ -1 & 2 & -1 & 0 \\ 0 & -1 & 2 & -1 \\ 0 & 0 & -1 & 1 \end{pmatrix}, \text{and } \mathbf{L}^{-1} = \begin{pmatrix} \frac{7}{8} & \frac{1}{8} & -\frac{3}{8} & -\frac{5}{8} \\ \frac{1}{8} & \frac{3}{8} & -\frac{1}{8} & -\frac{3}{8} \\ -\frac{3}{8} & -\frac{1}{8} & \frac{3}{8} & \frac{1}{8} \\ -\frac{5}{8} & -\frac{3}{8} & \frac{1}{8} & \frac{7}{8} \end{pmatrix} \tag{A3.4}$$

Since the two electrodes connect with the 1st and 4th nodes, the resistance distance between these two nodes $(\Omega)_{1,4}$ is calculated as $\frac{7}{8}+\frac{7}{8}-2\left(-\frac{5}{8}\right)=3$. Thus, the conductance g, which is the inverse of the resistance, is 0.333.

Chapter 4

Frontier Orbital View of Conductivity in Highly Conductive Single-Molecule Wires Based on One-Dimensional Topological Insulators

In normal single-molecule wires, the conductance of the molecular chain decays exponentially as the length of the molecular chain increases. Recently, single-molecule wires have been discovered that achieve reversed conductance decay, the behavior in which the conductance of the molecular chain increases as the length of the molecular chain increases. However, highly conductive wires that exhibit reversed conductance decay lose their reversed decay property when the chain length increases beyond certain lengths. In this study, the author shows that the loss of the reversed conductance decay can be reproduced by modifying the relation between the bond alternation and the conductance. Furthermore, the author shows that in the derivation process of the relation, it corresponds to the introduction of heteroatoms in the Hückel method and propose a means to maintain the inverse conductance damping based on them.

4.1. Introduction

The electrical conductivity of π-conjugated single-molecule junctions cannot ignore the influence of the wave property of electrons. In particular, it is known that the conductance decays exponentially due to the tunneling effect[88–93] and that the conductivity changes due to the interference of electron waves.[15,46,84,94] The relationship between the wire length L and the conductance g of a single molecule wire is as follows:

$$g = g_0 \exp(-\beta L) \tag{4.1}$$

where g_0 is the contact conductance and β is the conductance decay factor, which is generally positive. β is a molecule-specific value, and β generally has smaller values for π-conjugated wires than for σ-based wires.[95,96] If β is low, the conductance attenuation is small even when a wire is long. Therefore, it is necessary to design molecular structures that exhibit low β in order to realize single-molecule electronics.

In π-conjugated systems, several molecular structures have been theoretically proposed that exhibit negative β, i.e., the reversed conductance decay.[97–102] Based on the Hückel molecular orbital (HMO) method, the relationship between the conductance and the resonance integrals t_A and t_B in polyene wires is expressed as follows:[96]

$$g = \frac{2e^2}{h} \gamma_\mathrm{L} \gamma_\mathrm{R} \frac{1}{t_\mathrm{B}^2} \left(\frac{t_\mathrm{B}}{t_\mathrm{A}}\right)^{2n} \tag{4.2}$$

where $\gamma_\mathrm{L/R}$ is the broadening function and n is the number of polyene unit iterations. t_A and t_B are positive values because the energy unit is set to the resonance integral $t\ (< 0)$ between adjacent 2pπ orbitals of the benzene ring. From eqs. (4.1) and (4.2), β is expressed as follows:

$$\beta = -2 \ln\left(\frac{t_\mathrm{B}}{t_\mathrm{A}}\right) \tag{4.3}$$

Eq. (4.3) suggests that β is negative when $t_\mathrm{A} < t_\mathrm{B}$. Scheme 4.1 shows the relationship between t_A and t_B, and the corresponding resonance structure of the polyene wire. The tight-binding model for polyene wires as shown in Scheme 4.1 is called the finite Su-Schrieffer-Heeger (SSH) model.[103,104] In the finite SSH model, $t_\mathrm{A} > t_\mathrm{B}$ is called the trivial state, $t_\mathrm{A} = t_\mathrm{B}$ the metallic state, and $t_\mathrm{A} < t_\mathrm{B}$ the topological state. Polyene wires in the topological state are conductive at both terminal atoms and insulating at the other atoms. Materials that exhibit such properties are called one-dimensional topological insulators (1D-TIs).[105–108] As shown in Scheme 4.1, polyene wires in the topological state have electronic states such that there are radicals on the carbon atoms at both ends. Stuyver et al. show that β is negative for biradicals with radicals at both ends of the wire.[109] Garner et al. demonstrated the validity of the relationship shown by Tsuji et al. by using the NEGF–DFT calculations.[110]

Recently, molecular structures with negative β have been discovered by single molecule measurement techniques.[111,112] [n]cumulene has been shown to exhibit negative β by conductance measurements using the STM–BJ technique and DFT calculations.[113,114] Other compounds such as fused porphyrin,[115,116] cyanine,[117,118] and oxidized oligophenylene-bridged bis(triarylamines)[7] have also been reported to have negative β. However, it has been shown that the reversed conductance decay disappears at chain lengths above a certain level. Bajaj et al. reported that the disappearance of the reversed decay is due to the localization of frontier orbitals as a result of the change from the closed-shell to the open-shell state.[119] Li et al. demonstrated, using the tight-binding approximation and NEGF, that the disappearance of the reversed attenuation is due to contact with the electrode.[120] The results of Li et al. indicate that the reversed attenuation disappears although it is within the tight-binding approximations. Here, the author extends eq. (4.2) and shows that it can reproduce the vanishing of the reversed conductance decay in finite polyene wires. Furthermore, the author shows the relationship between the disappearance of the reversed conductance decay and the molecule-electrode interaction in polyene wires based on the orbital rule for the electron transport.[20,23,55]

Scheme 4.1. Resonance structures of a (3E,5E,7E)-1,3,5,7,9-decapentaene wire corresponding to the relationship between the resonance integral t_A and t_B.

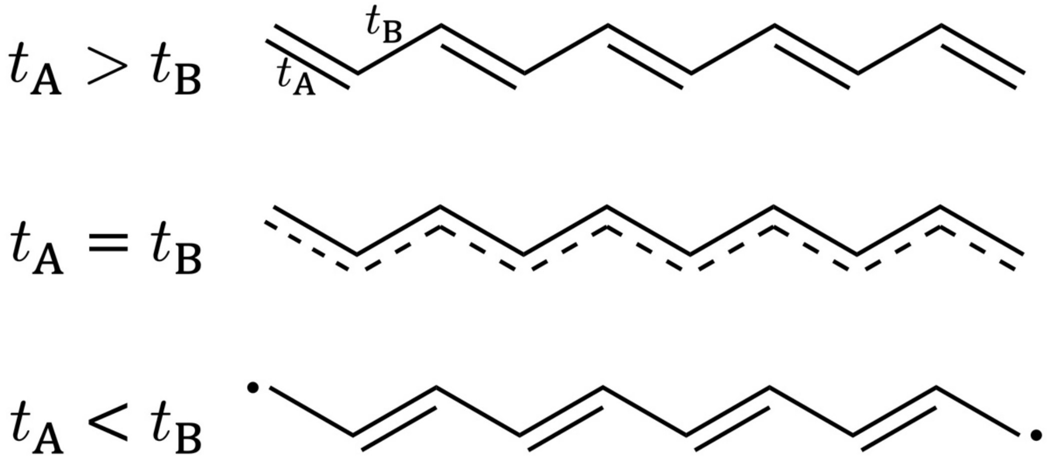

4.2. Results and Discussion

4.2.1. Derivation of the Modified Relation between the Conductance and the Resonance Integrals for Polyene Wires.

First, the author derives the relation that includes the interaction with the electrode by extending eq. (4.2). The polyene wire to be calculated consists of $2n$ carbon atoms, as shown in Figure 4.1. The electrode connects to both ends of the polyene wire.

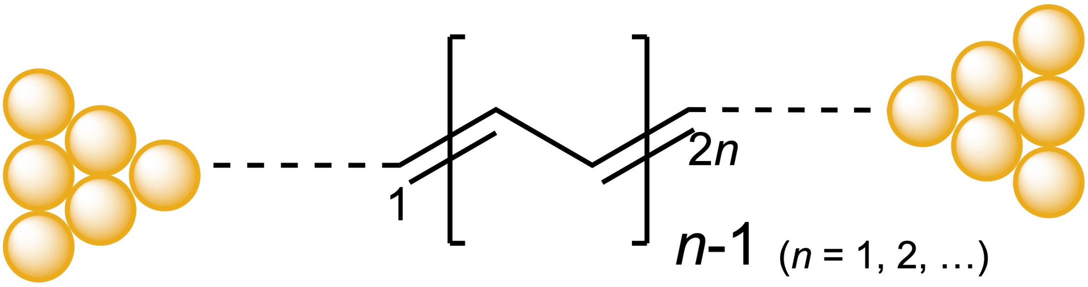

Figure 4.1. Schematic representation of a finite polyene wire junction.

The conductance of the single-molecule junction can be expressed using the NEGF. The Green's function used to calculate conductance is as follows:

$$\mathbf{G} = [E_{\mathrm{F}}\mathbf{I} - \mathbf{H} - \mathbf{\Sigma}_{\mathrm{L}} - \mathbf{\Sigma}_{\mathrm{R}}]^{-1} \tag{4.4}$$

where E_{F} is the Fermi energy, **I** is the identity matrix, **H** is the Hückel Hamiltonian of the molecule, and $\mathbf{\Sigma}_{\mathrm{L/R}}$ is the self-energy matrix for the left/right electrode. The self-energy matrix is the complex matrix representing the interaction between the molecule and the electrode. In the process of deriving eq. (4.2), the ZOGF used as shown below:

$$\mathbf{G} = -\mathbf{H}^{-1} \tag{4.5}$$

Here, the author simplifies the equation by placing $E_{\mathrm{F}} = 0$. Eq. (4.5) does not include the molecule–electrode interaction. In this study, the molecule–electrode interaction is assumed to be simple perturbations and the self-energy matrix is treated as the real matrix and incorporated into the effective Hamiltonian.

$$\mathbf{H}_{\text{eff}} = \mathbf{H} + \text{Re}[\mathbf{\Sigma}_{\text{L}}] + \text{Re}[\mathbf{\Sigma}_{\text{R}}] \tag{4.6}$$

In this system, $\text{Re}[\mathbf{\Sigma}_{\text{L}}]$ and $\text{Re}[\mathbf{\Sigma}_{\text{R}}]$ are matrices with parameters δ_{L} and δ_{R} in the (1,1) and (2*n*,2*n*) components, respectively, and zero for the other components. δ_{L} and δ_{R} are parameters related to the strength of the molecule–electrode interaction. Let t_{A} and t_{B} be the double bond and the single bond of the polyene wire, respectively, the effective Hamiltonian is represented by the following matrix.

$$\mathbf{H}_{\text{eff}} = \begin{pmatrix} \delta_{\text{L}} & t_{\text{A}} & 0 & 0 & \cdots & 0 \\ t_{\text{A}} & 0 & t_{\text{B}} & 0 & \cdots & 0 \\ 0 & t_{\text{B}} & 0 & t_{\text{A}} & \cdots & 0 \\ 0 & 0 & t_{\text{A}} & \ddots & \ddots & \vdots \\ \vdots & \vdots & \vdots & \ddots & 0 & t_{\text{A}} \\ 0 & 0 & 0 & \cdots & t_{\text{A}} & \delta_{\text{R}} \end{pmatrix} \tag{4.7}$$

Eq. (4.7) shows that $\delta_{\text{L/R}}$ formally corresponds to the change in the Coulomb integrals of the carbon atoms at both ends.[121]

Next, the inverse matrix of $\mathbf{H}_{\text{eff}}$ is calculated to obtain the Green's function for this model. Eq. (4.7) is a tridiagonal matrix. The inverse of the matrix can be calculated using Usmani's formula.[122,123] Thus, the (1,2*n*) components of the Green's function for the polyene wire are expressed as follows:

$$(\mathbf{G})_{1,2n} = (-1)^{n+1} \frac{t_{\text{A}}^{n} t_{\text{B}}^{n-1}}{t_{\text{A}}^{2n} - \delta_{\text{L}}\delta_{\text{R}} t_{\text{B}}^{2n-2}} \tag{4.8}$$

The Green's function of the polyene wire has been obtained and the conductance can be calculated. The conductance of a single-molecule junction can be approximated as follows:

$$g = \frac{2e^2}{h} T(E_{\text{F}}) \approx \frac{2e^2}{h} \gamma_{\text{L}}\gamma_{\text{R}} \left|(\mathbf{G})_{1,2n}\right|^2 \tag{4.9}$$

Substituting eq. (4.8) into eq. (4.9), the modified relationship between the conductance and the resonance integrals in polyene wires is obtained.

$$g = \frac{2e^2}{h} \gamma_{\mathrm{L}} \gamma_{\mathrm{R}} \left(\frac{t_{\mathrm{A}}^{n} t_{\mathrm{B}}^{n-1}}{t_{\mathrm{A}}^{2n} - \delta_{\mathrm{L}} \delta_{\mathrm{R}} t_{\mathrm{B}}^{2n-2}} \right)^2 \tag{4.10}$$

Eq. (4.10) is consistent with eq. (4.2) when $\delta_{\mathrm{L}} = \delta_{\mathrm{R}} = 0$. When the molecule–electrode interaction is considered, the denominator term $-\delta_{\mathrm{L}} \delta_{\mathrm{R}} t_{\mathrm{B}}^{2n-2}$ appears. Due to this term, the conductance at $t_{\mathrm{A}} \rightarrow 0$ does not diverge.

4.2.2. Comparison between Eq. (4.10) and the Results by the NEGF–HMO

The relationship between the number of carbon atoms and the transmission probability at the Fermi energy obtained from eqs. (4.2) and (4.10), and the NEGF–HMO method is shown in Figure 4.2. To clearly see the relationship between t_A and t_B in these calculations, the following relation between t_A and t_B is imposed as the constraint.

$$t_\mathrm{A} + t_\mathrm{B} = 2 \tag{4.11}$$

From eq. (4.11), $t_\mathrm{A} > 1$ corresponds to the trivial state and $t_\mathrm{A} < 1$ to the topological state. In this study, it is assumed that the same electrodes are used in the left and right sides. Therefore, in eq. (4.10), $\delta_\mathrm{L/R}$, which represents the interaction between the left and right electrodes and molecules, is set to the same value, $\delta_\mathrm{L} = \delta_\mathrm{R} = 0.1$. Note that the term for the molecule–electrode interaction in eq. (4.10) is always positive, regardless of the sign of $\delta_\mathrm{L/R}$, because only the product of δ_L and δ_R exists. When $t_\mathrm{A} > 1$, $T(E_\mathrm{F})$ decreases in both Figures 4.2a and 4.2b, corresponding to an increase in the number of carbon atoms. The gradient of $T(E_\mathrm{F})$ at $t_\mathrm{A} = 1.1$ is smaller than that at $t_\mathrm{A} = 1.2$. As the resonance integrals for the double and single bonds approach the same value, β becomes smaller. This trend is consistent with eq. (4.3). When $t_\mathrm{A} = 1.0$, both $T(E_\mathrm{F})$ remain unchanged as the number of carbon atoms increases. When $t_\mathrm{A} < 1$, i.e., topological state, there is a difference between eq. (4.2) and the other trends. In the plot using eq. (4.2), $T(E_\mathrm{F})$ increases monotonically with carbon chain length. On the other hand, plots using eq. (4.10) and the NEGF–HMO method show reversed conductance decay in the short carbon chain length range and normal conductance decay in the long carbon chain length range. The graph obtained from eq. (4.10) and that obtained by using the NEGF–HMO method have different shapes. The graph obtained from eq. (4.10) diverges at $t_\mathrm{A}^{2n} = \delta_\mathrm{L}\delta_\mathrm{R}t_\mathrm{B}^{2n-2}$ and therefore has a sharper peak than the graph obtained from the NEGF–HMO method calculation. However, the existence of maxima in both graphs indicates that they are qualitatively identical. In Figure 4.2a, when t_A = 0.9, 0.8, and 0.7, $T(E_\mathrm{F})$ has maxima at 22, 12, and 8 carbon atoms, respectively. It can be seen that as t_D decreases, the carbon chain length that can keep the reversed conductance decay becomes shorter. The same trend is observed in the results obtained by the NEGF–HMO method.

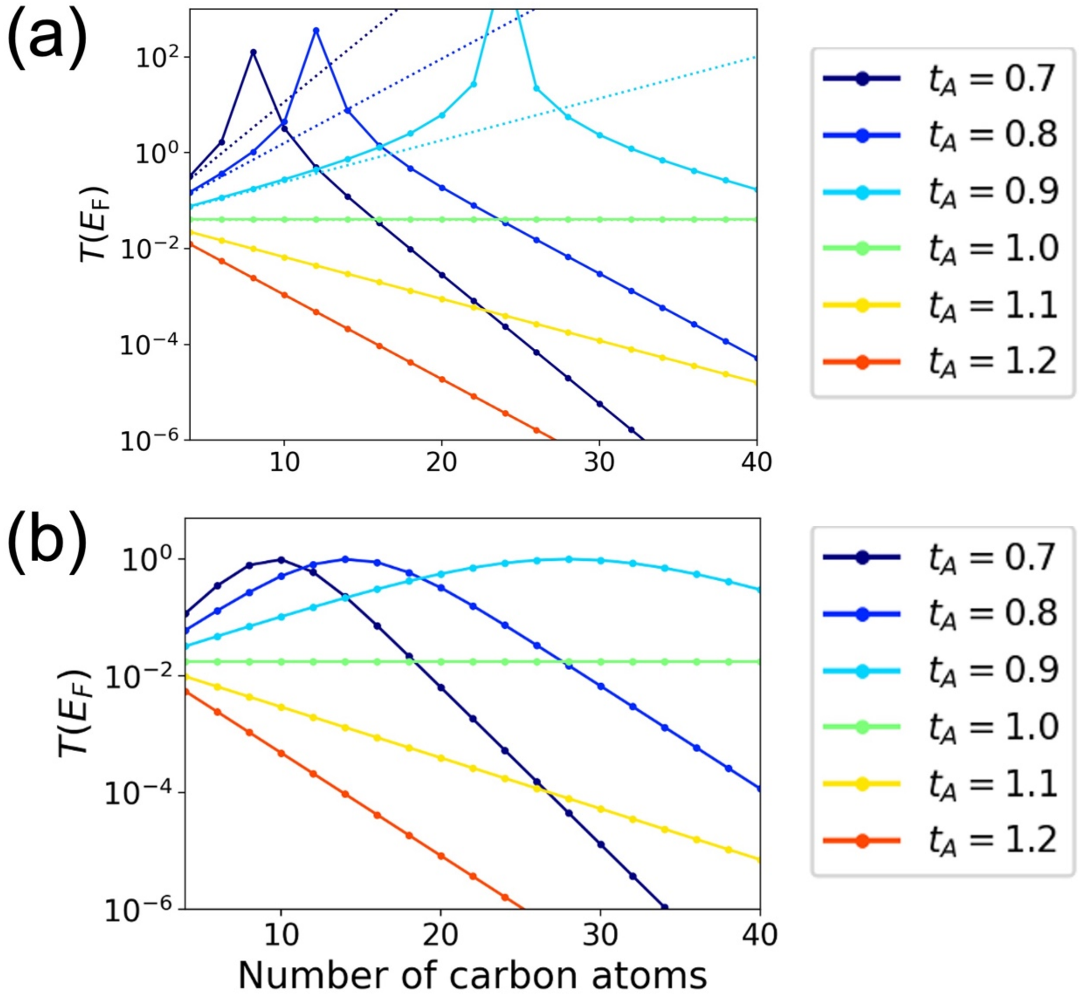

Figure 4.2. Transmission probability at the Fermi energy as a function of the number of carbon atoms for each t_{A} obtained by using (a) eq. (4.10) (solid lines), eq. (4.2) (dotted lines), and (b) the NEGF–HMO method.

Figure 4.3 shows the relationship between the number of carbon atoms in the polyene wire and the electron transmission probability at the Fermi energy for the finite polyene wire with different molecule–electrode interactions. In Figure 4.3, t_{A} is fixed at 0.8. The plots for $\delta_{\mathrm{L/R}} = 0.0$ and 0.1 are the same as the blue dotted and solid lines in Figure 4.2a, respectively. When $\delta_{\mathrm{L/R}} = 0.2$, the carbon chain length at which the reversed conductance decay disappears is shorter than that at $\delta_{\mathrm{L/R}} = 0.1$. Since $\delta_{\mathrm{L/R}}$ is the strength of the molecule–electrode interaction, the stronger this interaction becomes, the shorter the carbon chain length at which the reversed conductance decay disappears. This trend is consistent with the results shown by Li et al.[120] Therefore, it is clear that polyene wires in which the interaction between the molecule and the electrode is introduced in the form of the parameter can reproduce the disappearance of the reversed conductance decay.

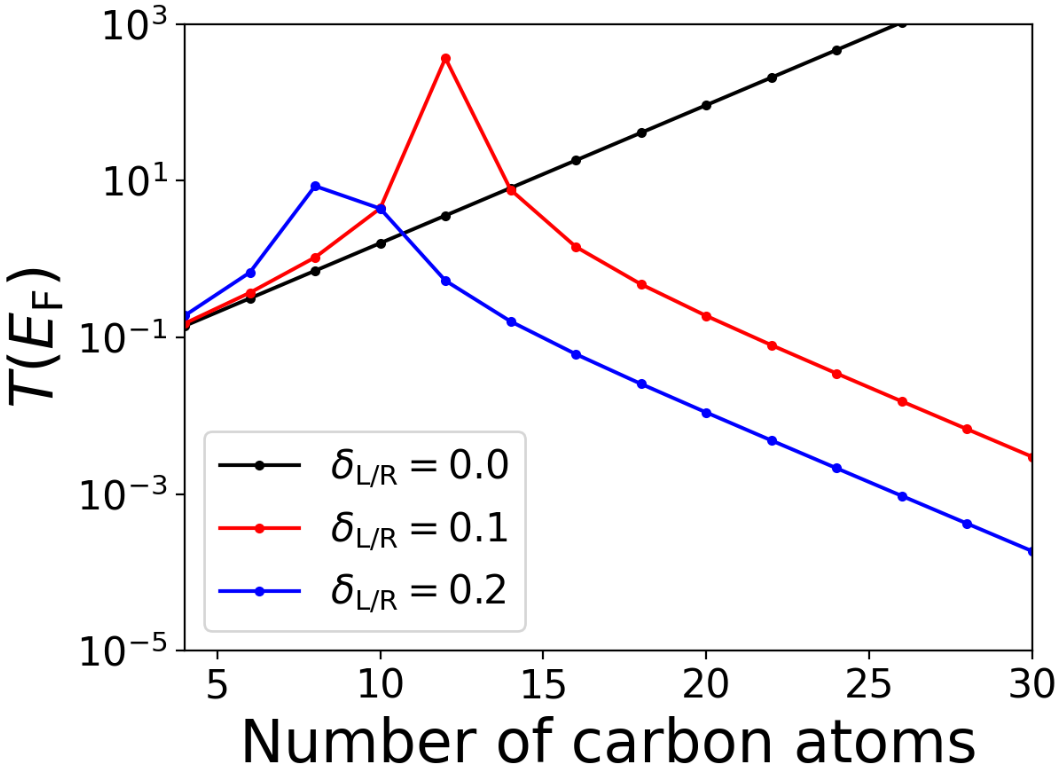

Figure 4.3. Relationship between the number of carbon atoms and transmission probabilities at the Fermi energy for the finite polyene wire junctions obtained by eq. (4.10). Black, red, and blue lines indicate $\delta_{\mathrm{L/R}} = 0.0$, 0.1, and 0.2, respectively.

4.2.3. Frontier Orbital Analysis for the Wire

The author has successfully reproduced the disappearance of the reversed conductance decay of the finite polyene wire considering the interaction between the molecule and the electrode. Eq. (4.10) is a simple extension of the Hückel Hamiltonian of finite polyene wires by adding perturbation terms to the elements of carbon atoms at both ends. It is now possible to use that Hamiltonian to discuss the vanishing of the conductance reversed conductance decay. The author discusses the mechanism of the vanishing of the reversed conductance decay by the introduction of $\delta_{\mathrm{L/R}}$ based on the orbital rule for electron transports.

When the electrodes are connected to atoms *r* and *s* in the molecule, the conductance is expressed by the following relation:[20,23]

$$g \propto \left| \frac{C_{r,\mathrm{HOMO}} C_{s,\mathrm{HOMO}}}{E_{\mathrm{F}} - \varepsilon_{\mathrm{HOMO}}} + \frac{C_{r,\mathrm{LUMO}} C_{s,\mathrm{LUMO}}}{E_{\mathrm{F}} - \varepsilon_{\mathrm{LUMO}}} \right|^2 \tag{4.12}$$

where $C_{r(s),\mathrm{HOMO(LUMO)}}$ is the orbital coefficient of the atom $r(s)$ in HOMO (LUMO) and $\varepsilon_{\mathrm{HOMO(LUMO)}}$ is the orbital energy level of HOMO (LUMO). Eq. (4.12) can be used to predict the trend of conductance.

From the previous discussion, it is clear that the carbon chain length at which the reversed conductance decay disappears becomes shorter as t_{A} decreases. By varying t_{A} for the single molecule of appropriate length, one can compare the electronic structures of molecules when the reversed conductance decay is observed and when the reversed conductance decay disappears. The author analyzed the relationship between t_{A} is 0.8 and 0.9, and to the region of vanishing reversed conductance decay when t_{A} is 0.7. It will be clarified whether there is difference in the electronic structure when belonging to each region.

Figure 4.4 shows the electron transmission probability and molecular orbitals of $C_{10}H_{12}$ wire at the Fermi energy. When $\delta_{\mathrm{L/R}} = 0.0$, $T(E_{\mathrm{F}})$ increases monotonically as t_{A} decreases (solid black line in Figure 4.4a). On the other hand, when $\delta_{\mathrm{L/R}} = 0.1$, $T(E_{\mathrm{F}})$ for the $C_{10}H_{12}$ wire increases as t_{A} decreases from the trivial state and reaches the maximum at $t_{\mathrm{A}} = 0.75$ (dashed line). Then, as t_{A} decreases further, $T(E_{\mathrm{F}})$ also decreases (solid red line in Figure 4.4a). It will be discussed these trends based on eq. (4.12). The author will be discussed the sign of the sign of the numerator in eq. (4.12). For both $\delta_{\mathrm{L/R}}$ = 0.0 and 0.1, the product of the orbital coefficients of the atoms connected to the electrode at HOMO and LUMO for any t_{D} are (+)(+) and (+)(–), respectively (Figure 4.4c). In these cases, the numerator has the same sign, but the sign of the denominator, i.e., the relationship between the Fermi energy and the orbital energy, shows different trends (Figure 4.4b). When $\delta_{\mathrm{L/R}} = 0.0$, for any t_{D}, the denominator is positive because the HOMO energy level is always below the E_{F} and negative because the LUMO energy level is always above the E_{F}. As t_{D} decreases, the HOMO and LUMO approach the Fermi energy, so the value of eq. (4.12) increases. On the other hand, when $\delta_{\mathrm{L/R}} = 0.1$, the behavior is different. When $t_{\mathrm{A}} > 0.75$, the denominator is positive because the HOMO energy level is below the E_{F}, and negative because the LUMO energy level is above the E_{F}. Both the HOMO and LUMO terms in eq. (4.12) are positive. As t_{A} decreases, the HOMO–LUMO gap decreases, so the absolute values of both terms in eq. (4.12) increase, indicating an increase in conductance. When $t_{\mathrm{A}} < 0.75$, the orbital phase and the relationship between the HOMO energy level and the Fermi energy remain unchanged, but the LUMO energy level is located below E_{F}. The LUMO term in eq. (4.12) changes to the negative value. As a result, the HOMO and LUMO terms cancel each other and the conductance decreases. Thus, it is clear that the disappearance of the reversed conductance decay is due to the change in the sign of eq. (4.12) due to the change in the energy level of the orbital.

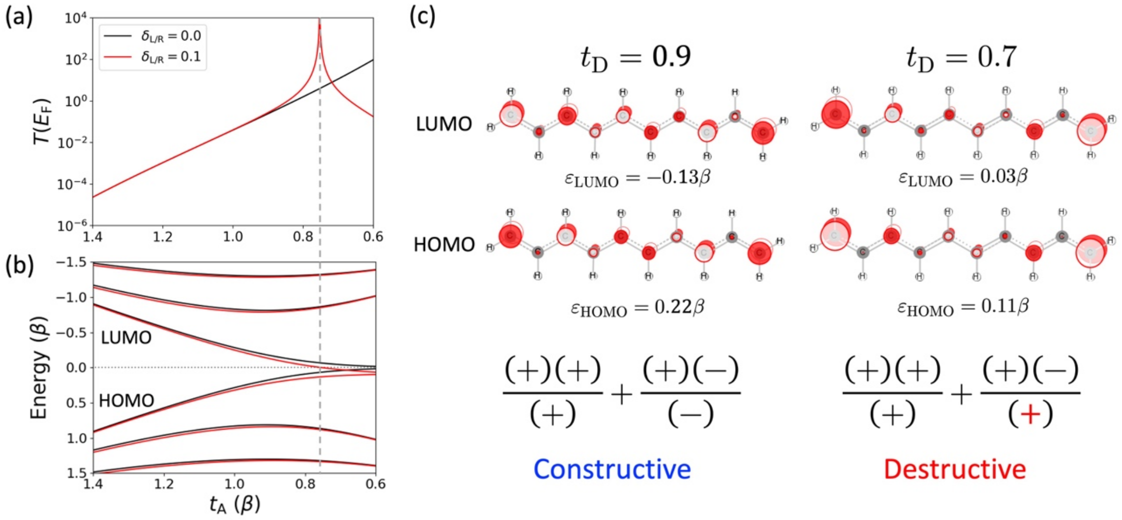

Figure 4.4. (a) Transmission probability at the Fermi level, (b) the orbital energy diagram as a function of t_A, and (c) frontier orbitals at t_A = 0.9 and 0.7 for a linear $C_{10}H_{12}$ wire. Black and red lines indicate $\delta_{L/R}$ = 0.0 and 0.1, respectively.

4.3. Conclusions

The author has improved the relation between bond alternation and conductance for finite SSH model by Tsuji et al. By using the effective Hamiltonian that replaces the electrode interaction as simple parameters, the disappearance of the reversed conductance decay can be reproduced. The author compared the plot of the electron transmission probability obtained from the NEGF-HMO method with a plot of the improved relation by imposing a constraint between the resonance integral of the double bond and the resonance integral of the single bond. The improved analytical equation is qualitatively consistent with the results using the NEGF-HMO method. This modification made it possible to analyze the conduction properties using the orbital law for electron transport. According to the improved relation, the chain length that switches from the reversed conductance decay to the normal decay becomes shorter as the interaction with the electrode becomes stronger. According to the improved relation, as the interaction with the electrode becomes stronger, the chain length that switches from inversion of conductance decay to normal decay becomes shorter. This trend is also consistent with the results obtained by the NEGF-HMO method. Furthermore, the author applied orbital rules for electron transport using molecular orbitals obtained from the effective Hamiltonian. In the region of reversed conductance decay, the HOMO and LUMO contributions in the ZOGF cause constitutive quantum interference, increasing the conductance of the single molecular wire. On the other hand, in the region of normal conductance decay, the phases of the HOMO and LUMO contributions of the ZOGF are opposite, resulting in destructive quantum interference and conductance decrease.

Chapter 5

Graph Theoretical Study on the Conduction Properties of Heteroatom Containing Single-Molecule Junctions

Based on Sachs' graph theory, the author formulated the conduction properties of a single molecular junction consisting of a molecule in which one carbon atom of the alternant hydrocarbon is replaced with a heteroatom. The derived formula includes odd and even powers of the adjacency matrix, unlike that for the graph of the parental structure. These correspond to the odd- and even-length walks. Also, since the heteroatom is represented as a self-loop of length 1 in the graph, an odd number of passes of the self-loop will change the parity of the length of the walk. In order to confirm the above effect of the heteroatom in a concrete example, the conduction behavior of meta-connected molecular junctions consisting of a hetero six-membered ring, whose conductive properties have already been measured in an experiment, was analyzed based on counting the number of walks.

5.1. Introduction

Single molecule junctions exhibit unique electron transport properties that are not found in extended systems, such as solids and polymers.[1,2,15,26,28,46,124–127] One of the unique transport properties there is the phenomenon of interference between transporting electrons. This is called quantum interference (QI) and is due to the quantum phase of the electrons caused by the wave and particle duality.[15,28,46,128] There are two types of QI: constructive QI, which occurs when the electron phases are the same,[15,32] and destructive QI, which occurs when the electron phases are opposite.[46,129,130] In this chapter, the author will refer to destructive QI simply as QI.

A graph-theoretic approach has been proposed as one way to predict whether or not QI will occur in single-molecule junctions.[24] Graph theory is a field of mathematics that uses graphs, a mathematical tool for modeling pairwise relationships between objects.[131] The graph is a set of vertices and edges, where an edge can connect two vertices, or start from a vertex and return to itself. Graph theory can be applied to chemistry using the adjacency matrix $\mathbf{A}$,[24,132–137] which is a matrix with entries of +1 if the pair of atoms are connected, while 0 if they are not. By treating atoms as vertices and bonds as edges (see Figure 5.1a), one can reveal the topological properties of molecules.[132]

QI can be explained using the concept of a walk on the molecular graph.[24,131,138,139] In the graph represented by $\mathbf{A}$, the number of walks of length k starting at node i and ending at j is equal to the (i, j) element of the kth power of the adjacency matrix, i.e., $(\mathbf{A}^k)_{ij}$.[138] Using molecular graphs for alternant hydrocarbons, which do not contain any odd-membered rings and heteroatoms, their single-molecule conductivity can be related to the presence of odd-length walks on their graphs (see Figure 5.1a for an example).[24,123] In benzene, there are odd-length walks between the two carbon atoms in the para position (Figure 5.1b, left) while even-length walks between the two carbon atoms in the meta position (Figure 5.1b, right). Therefore, the molecular junction becomes conductive when the electrodes are connected to the two carbon atoms in the para position of the benzene ring, and insulative when connected to the carbon atoms in the meta position.[140–143]

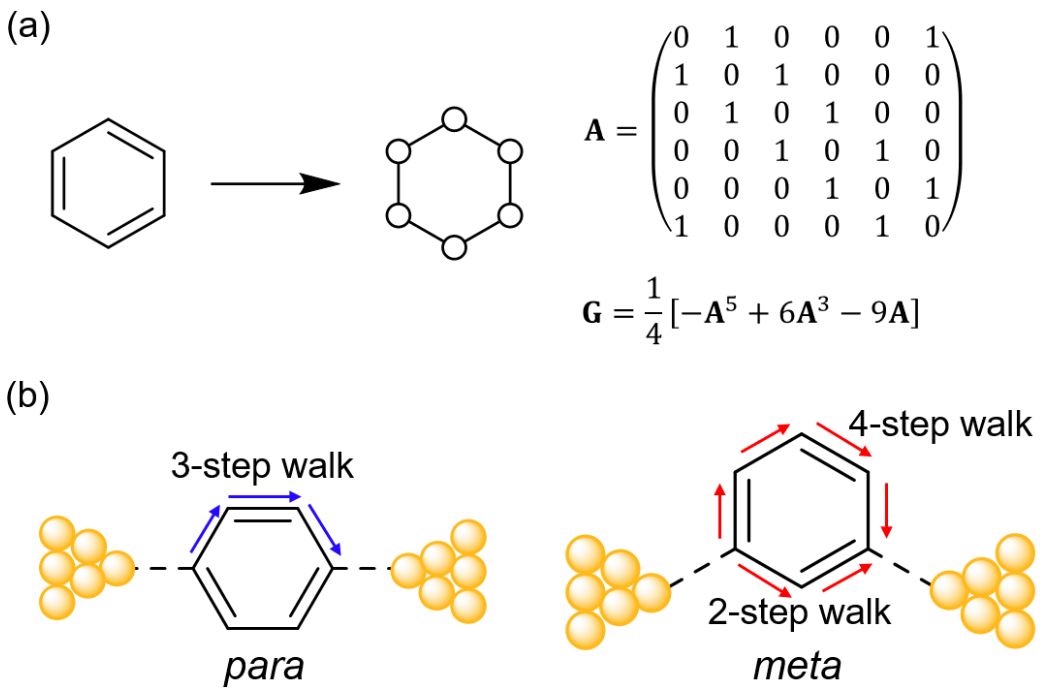

$$\mathbf{A} = \begin{pmatrix} 0 & 1 & 0 & 0 & 0 & 1 \\ 1 & 0 & 1 & 0 & 0 & 0 \\ 0 & 1 & 0 & 1 & 0 & 0 \\ 0 & 0 & 1 & 0 & 1 & 0 \\ 0 & 0 & 0 & 1 & 0 & 1 \\ 1 & 0 & 0 & 0 & 1 & 0 \end{pmatrix}$$

$$\mathbf{G} = \frac{1}{4}[-\mathbf{A}^5 + 6\mathbf{A}^3 - 9\mathbf{A}]$$

Figure 5.1. (a) Graph representation corresponding to benzene, its adjacency matrix **A**, and its ZOGF **G** expanded in a series of **A**. Note that only odd powers of **A** contribute to **G**. (b) Examples of walks on benzene molecular graphs connected with two electrodes in two different manners (para and meta).

The above is a very intuitive interpretation of QI, but unfortunately, this method cannot be directly applied to molecules containing heteroatoms, because the electron-hole symmetry is often broken in such molecules.[144,145] In this study, the author uses a graph-theoretic method called Sachs graph to solve this problem and try to open up a new aspect of QI by relating the conduction behavior of single-molecule junctions containing a heteroatom to walks on the graph.

5.2. Results and Discussion

5.2.1. Derivation of ZOGF Based on the Graph Theory

The author begins with a brief review of the relationship between the theory of molecular conduction and graph theory. The conductance of a single molecule, g, can be calculated from Landauer formula[14,25] combined with the NEGF.[26,146,147] Landauer formula is given by

$$g_{ij} = \frac{2e^2}{h} T_{ij}(E_\mathrm{F}), \tag{5.1}$$

where the (i, j) entry corresponds to the sites of i and j in the molecule connected with the two electrodes, $2e^2/h$ quantum conductance, and $T_{ij}(E_\mathrm{F})$ the transmission probability at the Fermi energy. The transmission probability can be proportional to the (i, j) entry of the ZOGF, G_{ij}, as follows:[148]

$$T_{ij}(E_\mathrm{F}) \propto \left|G_{ij}\right|^2. \tag{5.2}$$

If the Fermi energy is assumed to be located at $E = 0$, ZOGF takes the following simple form:[123]

$$\mathbf{G}(E_\mathrm{F}) = -\mathbf{H}^{-1}. \tag{5.3}$$

In this study, the Hückel Hamiltonian, $\mathbf{H}$, is used to describe the electronic structure of π systems. If the on-site Coulomb energies of all the sp^2 carbon atoms are the same and their values can be set to zero without loss of generality, then the diagonal elements of $\mathbf{H}$ are all zero. $\mathbf{H}$ can be written as

$$\mathbf{H} = \beta\mathbf{A}, \tag{5.4}$$

where β is the resonance integral between adjacent carbon 2pπ orbitals and $\mathbf{A}$ is the adjacency matrix for the molecular graph. If β is used as the unit of energy, the Hamiltonian can be simplified as **H** = **A**. Thus, ZOGF is rewritten as

$$\mathbf{G}(E_\mathrm{F}) = -\mathbf{A}^{-1}. \tag{5.5}$$

By examining the inverse of the adjacency matrix, one can predict the conductive properties of molecular junctions. Thus, the topology of the π-conjugated network can be linked to the molecular conductivity.

The topological properties of a graph can be revealed by examining the characteristic polynomial, $p(\lambda)$, which is defined as follows:[149]

$$p(\lambda) = \det|\lambda\mathbf{I} - \mathbf{A}| = \sum_{n=0}^{N} a_n \lambda^{N-n} = 0 \tag{5.6}$$

where **I** is the identity matrix, N is the total number of sp^2 carbon atoms in the π-conjugated network, and an is the coefficient of the ($N - n$)-th power term of λ.

Let us consider molecular junctions of closed-shell alternant hydrocarbons: N must be an even number. Applying the Cayley-Hamilton theorem[150] to eq. 5.6, one obtains

$$-\mathbf{A}^{-1} = \frac{1}{a_N} \sum_{n=0}^{N-1} a_n \mathbf{A}^{N-n-1}. \tag{5.7}$$

From eqs. 5.5 and 5.7, ZOGF is obtained in the form of a series expansion in terms of **A**. The coefficients in the characteristic polynomial can be obtained on the basis of the topology of the molecular graph, according to Sachs' formulation.[134,151] This process involves so-called Sachs graphs, which have two components: a complete graph K_2 consisting of two vertices and a cycle C_m consisting of m vertices.[151]

For alternant hydrocarbons without heteroatoms, the coefficients of the terms in the characteristic polynomial can be calculated using Sachs' formula[134,151,152] as follows:

$$a_n = \sum_{s \in S_n} (-1)^{c(s)} 2^{r(s)}, \tag{5.8}$$

where s is a Sachs graph, S_n a set of all Sachs graphs with n vertices, $c(s)$ the total number of components in s (i.e., how many K_2's and C_m's are included), and $r(s)$ the number of cycles with three or more nodes in s (i.e., how many C_m's where $m \geq 3$ are included). Note that $a_0 = 1$ by definition.[151]

If S_n does not contain any Sachs graphs with odd-membered rings, that is, if the molecule represented by the chemical graph in question corresponds to an alternant hydrocarbon, then S_n consists only of those with an even number of vertices. In other words, S_n will not contain any Sachs graphs with an odd number of vertices; S_n with n odd will be the empty set. Since Sachs graphs may be unfamiliar to beginners, an example using benzene is shown in Figure 5.2a. The reader is invited to work out how it works.

Due to alternancy, a_n with n odd is zero. Only when n is even, a_n contributes to the characteristic polynomial and then to ZOGF. Hence, the right-hand side of eq. 5.7 for alternant hydrocarbons consists only of odd powers of **A**. Note that the exponent of **A** is $N - n - 1$, which is odd when n of a_n is even. This is why the ZOGF expression in Figure 5.1a contains only odd powers of **A**.

The elements of the nth power of **A** count the number of walks starting at one node of the graph and ending at the starting point or another node in n steps. If there are only walks of even length between nodes i and j, the (i, j) entry of ZOGF for alternant hydrocarbons is zero because ZOGF does not contain even powers of **A**.[24] In such a case, molecular conductance is predicted to be small. This is exactly the graph-theoretic explanation of QI.

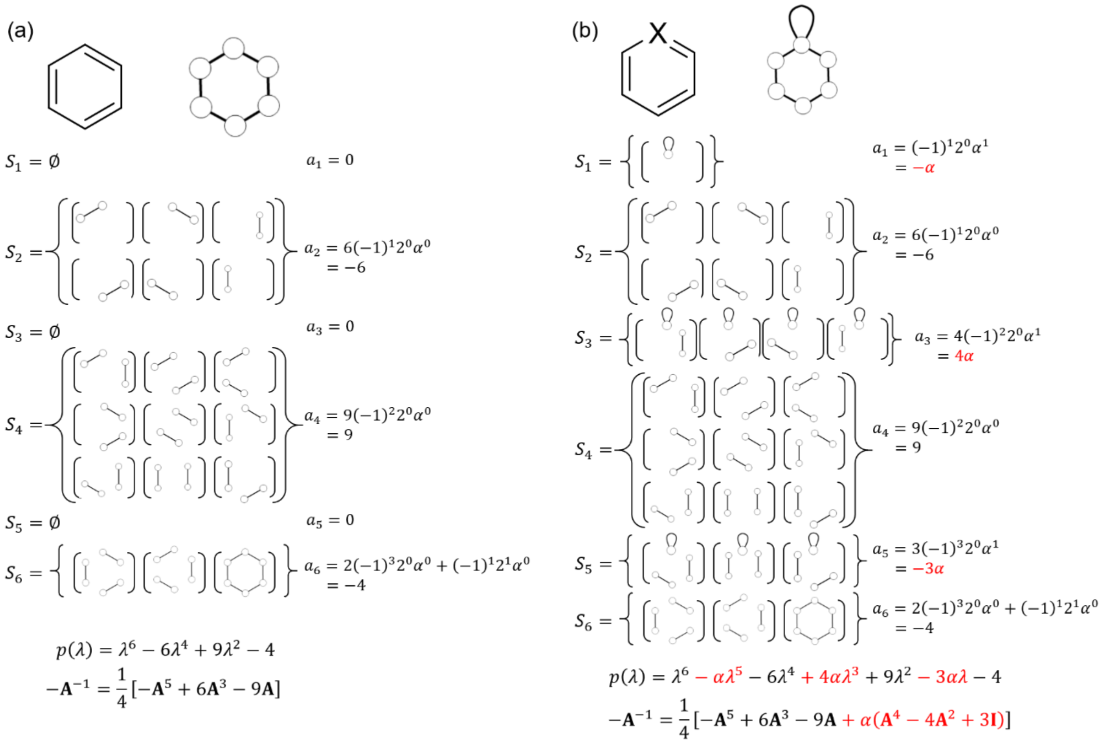

Figure 5.2. How the Sachs graph can be used to calculate the coefficients of the characteristic polynomial $p(\lambda)$, i.e., the coefficients for the powers of $\mathbf{A}$ in the ZOGF expression for (a) benzene and (b) its heterocyclic analogue obtained by replacing one carbon atom with a heteroatom X, whose effect on the equations is described by the heteroparameter of α. Terms involving α are shown in red.

5.2.2. Derivation of ZOGF for a Single-Molecule Junction with a Heteroatom

Now, let us take a look at the effect of the introduction of a heteroatom on what the author has discussed so far. To calculate the characteristic polynomial for a molecular graph with a heteroatom introduced, one needs to define the adjacency matrix for such molecular graphs. Hetero-conjugated molecules can be represented by edge-weighted graphs in which one or more edges are weighted to distinguish them from other edges. The weighted edge starts at the node corresponding to the heteroatom and ends at itself. The weight is identified by a parameter of α, specific to the type of heteroatom. The weighted edge for a heteroatom in a molecular graph is visually identified by a loop (a cycle of one node, a.k.a. self-loop).[132,135,149] An edge-weighted graph is given as an example in Scheme 5.1.

Scheme 5.1. Edge-weighted graph representation for a heterocyclic analogue of benzene. X indicates the heteroatom, which is represented by a loop in the graph.

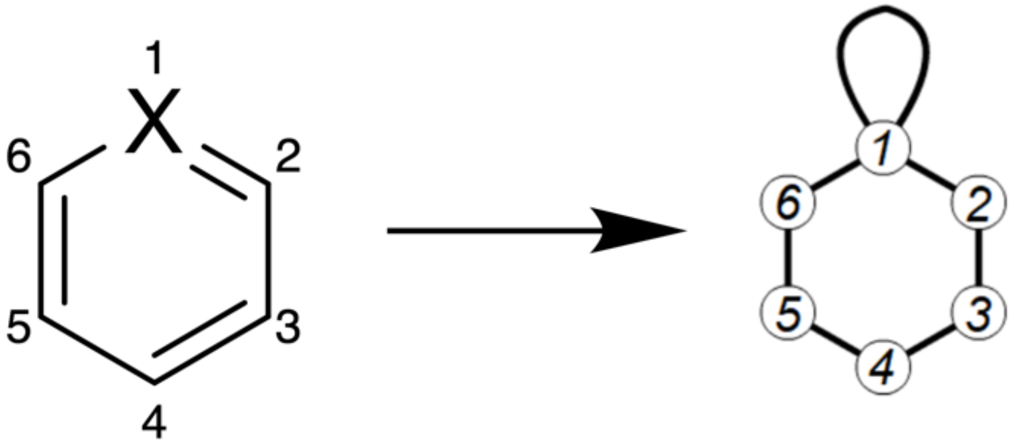

The adjacency matrix for the molecule shown in Scheme 5.1 is written as

$$\mathbf{A} = \begin{pmatrix} \alpha & 1 & 0 & 0 & 0 & 1 \\ 1 & 0 & 1 & 0 & 0 & 0 \\ 0 & 1 & 0 & 1 & 0 & 0 \\ 0 & 0 & 1 & 0 & 1 & 0 \\ 0 & 0 & 0 & 1 & 0 & 1 \\ 1 & 0 & 0 & 0 & 1 & 0 \end{pmatrix}. \tag{5.9}$$

Since the diagonal entries of the adjacency matrix can be traced back to the Coulomb integrals for the corresponding atoms. Given the heteroatom of X is described by the Coulomb integral of α_{X} different from that for the carbon atom, α_{C}, the parameter of α is related with these Coulomb integrals as follows:[135,153]

$$\alpha = \frac{\alpha_{\mathrm{X}} - \alpha_{\mathrm{C}}}{\beta}, \tag{5.10}$$

The introduction of a heteroatom causes electronegativity perturbation, which breaks the electron-hole symmetry characteristic of alternant hydrocarbons.[154] The middle point of the HOMO–LUMO gap, at which the author assumes the Fermi energy to be located, will not necessarily coincide with $E = 0$. However, since the author is only considering the introduction of a single heteroatom for now, the change in Fermi energy, if any, will not be so significant. As such, it would still be reasonable to set the Fermi energy of the hetero-conjugated system at $E = 0$. Indeed, such an assumption has been used in previous studies.[144,155,156] The author will continue to try to understand the conductivity using eqs. 5.5 through 5.7. The author is currently conducting a graph-theoretic study of QI at energies other than $E = 0$, the results of which will be reported elsewhere.

The coefficients of the terms in the characteristic polynomial calculated using eq. 5.8 need to be modified when a heteroatom is introduced. For this purpose, a modified Sachs graph was proposed as follows:[135]

$$a_n = \sum_{s \in S_n} (-1)^{c(s)} 2^{r(s)} \alpha^{l(s)}, \tag{5.11}$$

where $l(s)$ is the number of self-loops in s. Note that the number of self-loops is not accounted for in $r(s)$. In this study, for starters, the author investigates molecules without odd-membered rings, so Sachs graphs with an odd number of nodes are solely due to the self-loop corresponding to the heteroatom (see Figure 5.2b for an example).

For a molecule containing only one heteroatom, $l(s)$ can take the value of 0 or 1. $l(s) = 1$ when n of S_n is odd; otherwise, $l(s) = 0$ when n is even. Thus, $l(s)$ may be expressed as $\frac{1-(-1)^n}{2}$. From the above discussion, one can see that ZOGF for an alternant hydrocarbon with a carbon atom replaced with a heteroatom can be expressed as[1]

$$\mathbf{G} = \frac{1}{a_N} \sum_{n=1}^{N/2} \left(a_{2n-2} \mathbf{A}^{N-2n+1} + \alpha a_{2n-1} \mathbf{A}^{N-2n} \right). \tag{5.12}$$

In this equation, there are even powers of **A**, which are not present in the ZOGF expression for alternant hydrocarbons without heteroatoms. One should notice that the even powers of **A** in this equation are always multiplied by α.

The odd powers of **A** in eq. 5.12 are not multiplied by α, and their coefficients can be traced back to what is shown by eq. 8. This means that the coefficients of the odd power terms of **A** in eq. 5.12 are the same as those calculated for the molecule obtained by converting the introduced heteroatom back to a carbon atom. To put it another way, the introduction of the heteroatom does not change the coefficients of the odd powers of **A** in ZOGF.

The effect of the heteroatom on ZOGF appears primarily through the coefficients of the even powers of **A**. However, it is also important to note that it is not only the even powers of **A** that are involved in the process of incorporating the heteroatom effect into ZOGF. With the introduction of the heteroatom, the self-loop is added to the molecular graph. Therefore, walks traversing the self-loop must also be considered. The number of steps required to pass through the self-loop part is one, so each time one passes through

---

[1] Note that $\mathbf{G} = \frac{1}{\sum_{s \in S_N} (-1)^{c(s)} 2^{r(s)}} \left(\mathbf{A}^{N-1} + \sum_{n=1}^{N-1} \sum_{s \in S_n} (-1)^{c(s)} 2^{r(s)} \alpha^{\frac{1-(-1)^n}{2}} \mathbf{A}^{N-n-1} \right) = \frac{1}{\sum_{s \in S_N} (-1)^{c(s)} 2^{r(s)}} \sum_{n=1}^{N/2} \left[\sum_{s \in S_{2n-2}} (-1)^{c(s)} 2^{r(s)} \mathbf{A}^{N-2n+1} + \alpha \sum_{s \in S_{2n-1}} (-1)^{c(s)} 2^{r(s)} \mathbf{A}^{N-2n} \right]$.

the self-loop, the length of the walk increases by one.

If there are only even-length walks between two nodes on a bipartite graph, conduction between them is forbidden due to QI. When a heteroatom is introduced, even powers of **A** appear in the ZOGF formula, so that conduction between the two can be allowed. On top of that, if there is a self-loop due to the heteroatom in the middle of the even-length walk, it can change into an odd-length walk after passing through it once, contributing to the ZOGF formula through the odd powers of **A**. This is also one of the reasons why conduction between the two gets allowed.

5.2.3. Application to the Six-Membered Ring Systems

In recent years, researchers have paid attention to the conductance of heterocyclic compounds, especially their QI properties.[144,157–161] Eq. 12, which the author has derived in this study, is useful for understanding the conduction properties of even-membered heterocyclic compounds containing one heteroatom. Conductance calculations[144] and measurements[157] have been made for the heterocyclic analogue of benzene. Let us see in the following whether eq. 12 is effective in rationalizing the known facts in these previous studies.

Suppose that the benzene-like heterocycle is numbered as in Scheme 5.1. When electrodes are connected to the second and fourth sites or the second and sixth sites, meta-connected molecular junctions are formed, but it has been experimentally confirmed that the conductivity of these molecular junctions is higher than that of a meta-connected molecular junction consisting of a benzene ring.[157] This experimental result is interpreted as a loss of QI properties due to the introduction of the heteroatom. On the other hand, it has also been found that when electrodes are connected to the third and fifth sites, the measured conductance is almost identical to that of the meta-connected benzene molecular junction. In the literature, one can find a theoretical study by Sangtarash et al.[162] who, with a beautiful formulation using the Dyson equation, reduced the problem of QI in molecular junctions containing a heteroatom to the problem of parity of connection sites. Their results are also consistent with the experiment.

Now the author will see if our formulation can provide insight into the experimental results. From eq. 12, one can obtain a series expansion of the ZOGF for the heterocyclic analogue of benzene as follows:

$$\mathbf{G} = \frac{1}{4}[-\mathbf{A}^5 + 6\mathbf{A}^3 - 9\mathbf{A} + \alpha(\mathbf{A}^4 - 4\mathbf{A}^2 + 3\mathbf{I})] \tag{5.13}$$

As a natural consequence of eq. 12, the author sees that this equation contains even powers of $\mathbf{A}$, and they are multiplied by the heteroparameter of α.

The matrix representation of the ZOGF for the molecule is written as follows:

$$\mathbf{G}=\frac{1}{2}\begin{pmatrix} 0 & -1 & 0 & 1 & 0 & -1 \\ -1 & \frac{\alpha}{2} & -1 & -\frac{\alpha}{2} & 1 & \frac{\alpha}{2} \\ 0 & -1 & 0 & -1 & 0 & 1 \\ 1 & -\frac{\alpha}{2} & -1 & \frac{\alpha}{2} & -1 & -\frac{\alpha}{2} \\ 0 & 1 & 0 & -1 & 0 & -1 \\ -1 & \frac{\alpha}{2} & 1 & -\frac{\alpha}{2} & -1 & \frac{\alpha}{2} \end{pmatrix}. \tag{5.14}$$

This formula can be obtained by inverting the adjacency matrix shown in eq. 9 or by substituting it into **A**'s in eq. 13. The absolute value of the matrix element $(\mathbf{G})_{ij}$ is a rough guide to predict whether the conductivity will be high or low when the electrodes are connected to the i-th and j-th sites in the molecule.

Consider the case where the electrodes are connected to the meta-position. That is, the author considers electron transport between sites separated by only even-length walks along the ring aside from the walk through the self-loop. For the 2-4, 2-6, and 4-6 connections, the corresponding matrix element of **G** is either α/4 or -α/4. In these connection patterns, the larger the absolute value of the parameter α, the larger the value of conductance. This means that the conductance depends on the nature of the heteroatom. For the 1-3, 1-5, and 3-5 connections, the corresponding matrix element of **G** is 0. This means that in these connection patterns, the QI properties are maintained even when the heteroatom is introduced.

Consider the case where the electrodes are connected to the para-position. That is, the author considers electron transport between sites separated by only odd-length walks along the ring aside from the walk through the self-loop. The corresponding matrix element of **G** is 1/2. The value of the ZOGF does not change with the value of the heteroatom parameter.

The above is just a reproduction of experimentally known facts using the Hückel method. What the author really wants to do is not just to invert **A** to obtain **G**, but to provide insight into why the matrix elements of **G** should take the values they do. To this end, the author will analyze the difference between conductive and insulative connection modes using the path counting scheme as developed in the first half of this manuscript.

The meta-connections of electrodes in the heterocyclic analogue of benzene were represented by three types (see Figure 5.3): the 3-5 connection insulative is called meta1, and the 2-4 and 2-6 connections conductive are called meta2 and meta3, respectively.

In benzene, when electrodes are attached to the two carbon atoms in the meta-position, there are only even-length walks between the connected sites. However, it is also important to note that there is a self-loop in the heterocycle, so odd-length walks come in between the two sites.

First, the author considers walks in the 3-5 connection (meta1) as shown in Figure 5.3a. One can find one walk of length 2, which results in $(\mathbf{A}^2)_{3,5} = 1$, five walks of length 4, which result in $(\mathbf{A}^4)_{3,5} = 5$, and one walk of length 5 that includes one passage through the self-loop, which results in $(\mathbf{A}^5)_{3,5} = \alpha$. The cancellation between the contributions from the 2-step, 4-step, and 5-step walks is complete as shown at the bottom of Figure 5.3a, and the matrix element of the ZOGF becomes zero.

Next, the author considers walks in the 2-4 connection (meta2) as shown in Figure 5.3b. One can find one walk of length 2, which results in $(\mathbf{A}^2)_{2,4} = 1$, five walks of length 4, which result in $(\mathbf{A}^4)_{2,4} = 5$, and two walks of length 5 that include one passage through the self-loop for each, which result in $(\mathbf{A}^5)_{2,4} = 2\alpha$. The cancellation between the contributions from the 2-step, 4-step, and 5-step walks is not complete as shown at the bottom of Figure 5.3b, and the matrix element of the ZOGF becomes $-\alpha/4$. The difference in conduction behavior between meta1 and meta2 can be attributed to the difference in the number of walks of length 5, which include one passage through the self-loop corresponding to the heteroatom. Therefore, the resulting finite conductance in meta2 depends on the parameter of the heteroatom.

Finally, the author considers walks in the 2-6 connection (meta3) as shown in Figure 5.3c. One can find one walk of length 2, which results in $(\mathbf{A}^2)_{2,6} = 1$, one walk of length 3 that includes one passage through the self-loop, which results in $(\mathbf{A}^3)_{2,6} = \alpha$, six walks of length 4, including one walk with two passes of the self-loop, which result in $(\mathbf{A}^4)_{2,6} = \alpha^2 + 5$, and seven walks of length 5 that consists of one walk with three passes of the self-loop and six walks with one pass of the self-loop, which result in $(\mathbf{A}^5)_{2,6} = \alpha^3 + 6\alpha$. The cancellation between the contributions from the 2-step, 3-step, 4-step, and 5-step walks is not complete as shown at the bottom of Figure 5.3c, and the matrix element of the ZOGF becomes α/4. meta3 is different from the other connections in that there is a 3-step walk with one pass through the self-loop. It is also striking that there are walks that go through the self-loop not just once, but twice or three times. These result in the terms α^2 and α^3. However, they are not included in the final ZOGF formula because they cancel each other out.

When the electrodes are attached to two carbon atoms in para-position with respect to each other in benzene, there are only odd-length walks in between. However, there is a self-loop in the benzene-like heterocycle. Consequently, there are even-length and odd-length walks between the connection sites.

The author considers the path of one of the para-connections, the 2–5 connection of benzene (see Figure 5.4a). The 2–5 connection has two 3-step walks and ten 5-step walks. From Figure S1a, it is evident that the (2,5)-th element of the ZOGF becomes 1/2.

Thereafter, the author considers the walks for the 2–5 connection of the benzene-like heterocyclic molecule (see Figure 5.4b). Its 2–5 connection has two 3-step walks, one 4-step walk, and 11 5-step walks. The 4-step and 5-step walks give rise to α and α^2 terms, respectively, because they pass through the self-loop. The term derived from the even-length walk is further multiplied by α; therefore, the two cancel each other out in the final expression. Therefore, the absence of QI in the para-connections of benzene and the benzene-like heterocycle is predicted, which is consistent with the experimental results.

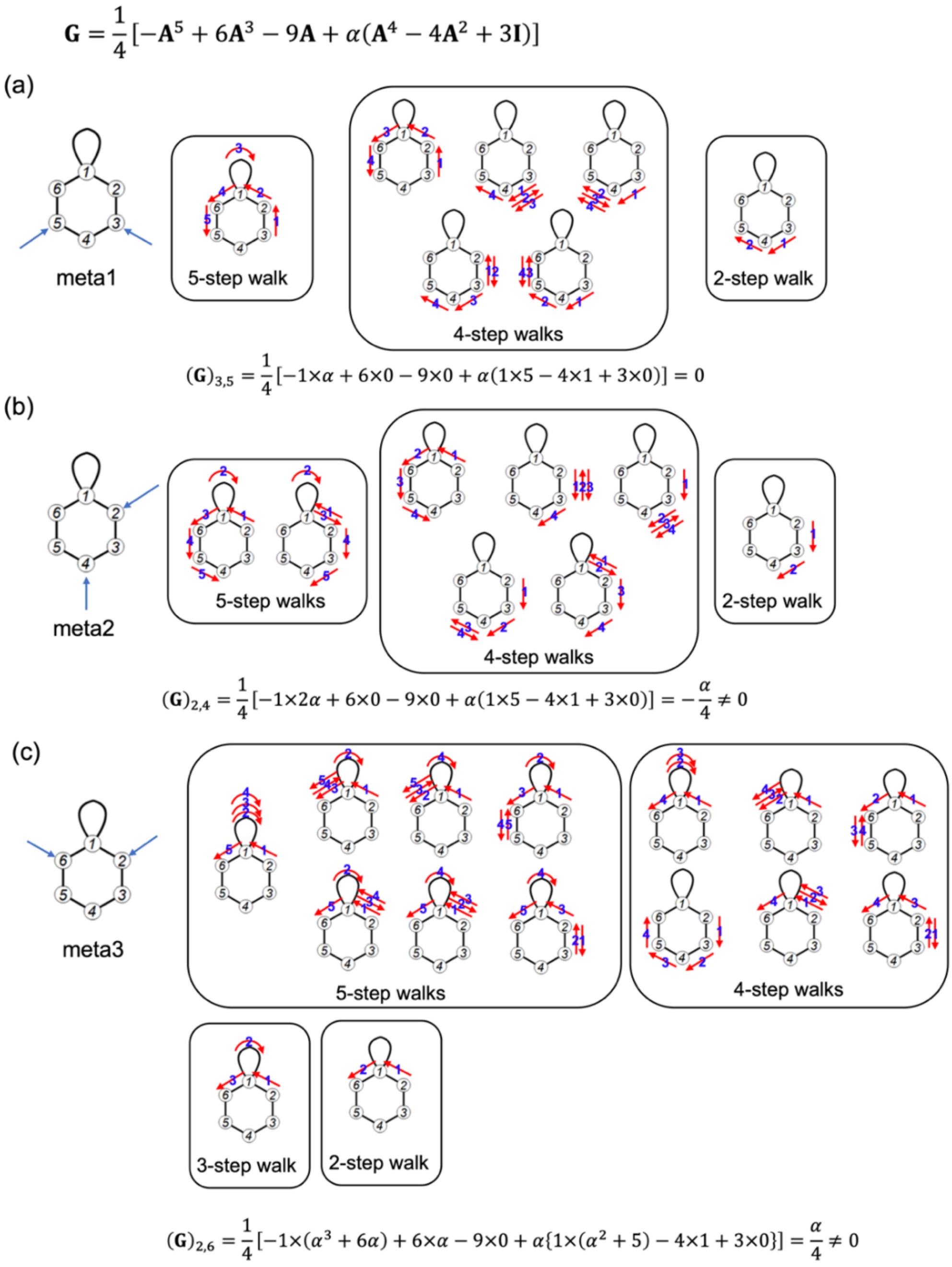

$$\mathbf{G} = \frac{1}{4}[-\mathbf{A}^5 + 6\mathbf{A}^3 - 9\mathbf{A} + \alpha(\mathbf{A}^4 - 4\mathbf{A}^2 + 3\mathbf{I})]$$

$$(\mathbf{G})_{3,5} = \frac{1}{4}[-1\times\alpha + 6\times0 - 9\times0 + \alpha(1\times5 - 4\times1 + 3\times0)] = 0$$

$$(\mathbf{G})_{2,4} = \frac{1}{4}[-1\times2\alpha + 6\times0 - 9\times0 + \alpha(1\times5 - 4\times1 + 3\times0)] = -\frac{\alpha}{4} \neq 0$$

$$(\mathbf{G})_{2,6} = \frac{1}{4}[-1\times(\alpha^3 + 6\alpha) + 6\times\alpha - 9\times0 + \alpha\{1\times(\alpha^2 + 5) - 4\times1 + 3\times0\}] = \frac{\alpha}{4} \neq 0$$

Figure 5.3. Visualizations of the walks on the molecular graph for the heterocycle (a) starting from the 3rd site and ending at the 5th site (meta1), (b) those starting from the 2nd site and ending at the 4th site (meta2), and (c) those starting from the 2nd site and ending at the 6th site (meta3).

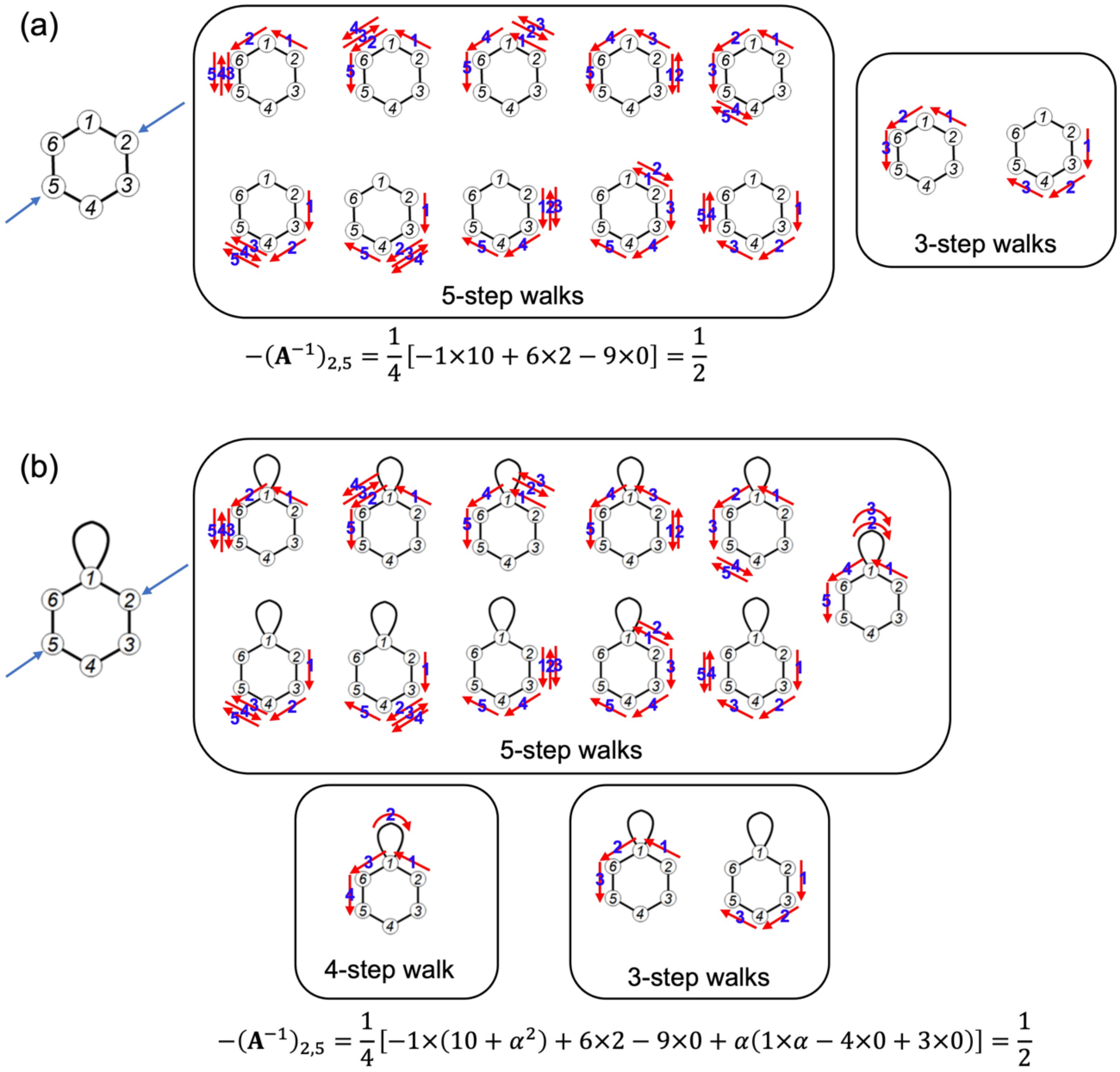

$$-(\mathbf{A}^{-1})_{2,5} = \frac{1}{4}[-1\times10 + 6\times2 - 9\times0] = \frac{1}{2}$$

$$-(\mathbf{A}^{-1})_{2,5} = \frac{1}{4}[-1\times(10+\alpha^2) + 6\times2 - 9\times0 + \alpha(1\times\alpha - 4\times0 + 3\times0)] = \frac{1}{2}$$

Figure 5.4. Visualizations of the walks on the molecular graph commencing from the 2nd atom and terminating at the 5th atom (para) for (a) benzene and (b) the heterocycle.

5.3. Conclusion

The author has investigated the conductance through a heteroatom-containing single-molecule junction by using the concept of Sachs graph and counting walks on the molecular graph. In order to incorporate the effect of the heteroatom on conductance, a weighted self-loop corresponding to it was introduced into the molecular graph. The author has shown that the ZOGF in such a situation can be expressed as the sum of the ZOGF for the parental graph without the heteroatom and the polynomial of even powers of the adjacency matrix multiplied by the heteroatom parameter. Since there is an experimental report on the measurement of conductance in several symmetrically distinct meta-type connection modes in a heterocyclic analog of benzene, the author tried to find the cause of the difference in conduction behavior by counting the walks on the molecular graph corresponding to the heterocycle on the basis of the ZOGF formula derived. In the meta-connected molecular junctions, the contributions of walks of different lengths to the ZOGF formula may or may not cancel each other out. In the former case, the ZOGF becomes zero and QI occurs, the conductance low, while in the latter case, higher conductance ensues. With the introduction of the heteroatom, even-length walks get to contribute to the ZOGF; on top of that, an odd number of passes through the self-loop corresponding to the heteroatom changes the parity of the walk on the graph corresponding to the parent structure without the heteroatom. This is the origin of the difference in conductance between molecular junctions consisting of meta-connected benzene and heterocyclic molecules.

Chapter 6

Frontier Orbital Insights into the Distance Dependence of the Appearance of Stacked Aromaticity

Recent research has both theoretically and experimentally validated the manifestation of stacked aromaticity through π-π stacking in antiaromatic molecules possessing 4n π electrons when arranged in a face-to-face configuration. However, the precise mechanisms underlying this phenomenon remain insufficiently explored. This study delves into the intricacies of stacked aromaticity by focusing on cyclobutadiene. In the face-to-face stacking, the orbital interactions between degenerate singly occupied molecular orbitals (SOMOs) of the monomer unit result in an increased energy gap between the degenerate highest-occupied molecular orbitals (HOMOs) and the lowest-unoccupied molecular orbitals (LUMOs) of the dimer. Despite this, antiaromatic molecules tend to be more stable in less symmetrical conformations primarily due to pseudo-Jahn-Teller distortions. In the case of cyclobutadiene, the two SOMOs of the monomer unit undergo splitting into HOMO and LUMO owing to bond alternation. In a face-to-face stacking arrangement, the HOMO-LUMO gap of the dimer is smaller than that of the monomer, a consequence of interactions between the HOMOs and LUMOs of the two monomer units. When the monomer units are positioned within a specific distance of each other, the HOMO and LUMO of the dimer, representing antibonding and bonding between the units, respectively, undergo interchange. This orbital alternation may contribute to an enhanced bond strength between the monomer units, thereby exhibiting stacked aromaticity. Our findings demonstrate the feasibility of manipulating the distance associated with stacked aromaticity by engineering the HOMO-LUMO gap of the monomer units.

6.1. Introduction

Aromaticity, a pivotal concept in organic chemistry, is employed to elucidate the distinctive stability of cyclic π-conjugated molecules. This stability is governed by the Hückel rule, indicating that planar π-conjugated cyclic molecules with 4n + 2 π electrons are stabilized (aromatic), while those with 4n π electrons are destabilized (antiaromatic).[163] This rule has been supported by theoretical approaches such as molecular orbital theory,[154,164–166] valence bond analysis,[167,168] and graph theory,[169–176] as well as experimental studies such as NMR peak shifts due to the presence of ring currents and analysis of carbon-carbon bond distances.[177]

Various strategies have been proposed to stabilize antiaromatic molecules, with recent focus on π-stacking as a means of achieving this stabilization. The superphane of an antiaromatic molecule exhibits aromatic-like properties, such as uniform bond distances and negative nucleus-independent chemical shift (NICS) values.[178] Further, it has been revealed that the stability point of cyclobutadiene dimers that are stacked in a face-face manner is at a π-stacking distance of 2.45 Å,[179] and that aromatic intermediate regions exist in the reaction pathway from the cyclobutadiene dimer to cubane.[180] The resulting aromaticity arising from the stacking of antiaromatic molecules is termed stacked aromaticity. Although its presence is explained through ring current analysis and graph theoretical approaches,[181,182] experimental observations related to stacked aromaticity are limited. [183–186]

Cyclophanes derived from the monomer unit of norcorrole, possessing antiaromatic properties, were successfully synthesized by Shinokubo et al. (Scheme 6.1a).[185] They observed the presence of face-to-face stacks, slipped stacks, and twisted stacks as the crystal structures. The HOMO and LUMO of the slipped and twisted stacks are derived from the HOMO and LUMO of the norcorrole monomer, respectively, while those of the face-to-face stack are derived from the LUMO and HOMO of the norcorrole monomer, respectively. Theoretical studies have also shown that orbital switching occurs when the π-stacking distance of Ni (II) norcorrole face-to-face stacking is reduced to 3.0 Å.[187] On the other hand, scanning tunneling spectroscopy shows that the HOMO-LUMO gap of the bilayers in antiaromatic meso-2-thioethyl-substituted 5,15-dioxaporphyrin is smaller than that of monolayers (Scheme 6.1b).[188] Despite stacking, these results demonstrate different properties among stacked antiaromatic molecules.

Scheme 6.1. Kekulé structures of (a) norcorrole and (b) 5,15-dioxaporphyrin and aromaticity of their monomers and dimers.

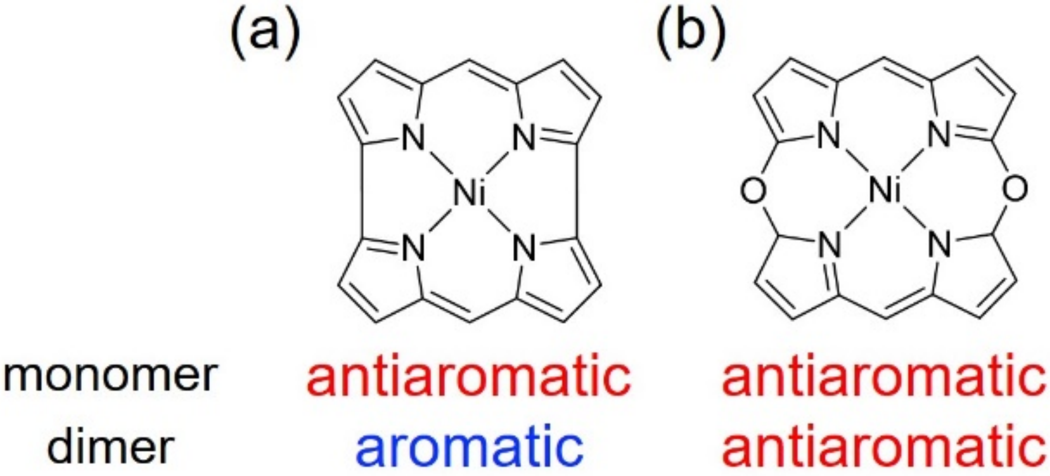

By examining both the π-stacking distance and the alterations in molecular orbitals, it may be feasible to elucidate the occurrence of stacking aromatization. In this investigation, the alterations in aromaticity and molecular orbitals within fully stacked dimer models featuring cyclobutadiene, the simplest antiaromatic molecule, were explored using density functional theory (DFT) calculations.[49,50] The study reveals that the π-stacking distance at which stacked aromaticity emerges varies based on the symmetry of cyclobutadiene, and the author elucidates its origin by considering the orbital interactions between monomer units. Orbital interaction analysis of cyclobutadiene dimers with D_{2h} and D_{4h} symmetries revealed a correlation between the HOMO-LUMO gap in the monomer and the π-stacking distance, which was analyzed in detail by adjusting the degree of bond alternation. These findings are anticipated to provide insights into molecular design strategies aimed at achieving stacked aromaticity.

6.2. Computational Details

These calculations were performed using B3LYP functional,[56,57] and 6-311+G** basis set,[58,59] implemented in the Gaussian 16 program package.[189] Generally, a structure wherein two monomers are connected by a carbon chain is used to reproduce realistic systems. However, in this study, the author performed single-point calculations in closed-shell singlet for a structure wherein the bridge is omitted, i.e., a model wherein the monomers are stacked such that they completely overlap, in order to investigate the impact of fine changes in the π-stacking distance.[190] Cyclobutadiene was employed as the monomer unit. The structure of cyclobutadiene possesses D_{2h} symmetry, wherein bond alternations occur in the closed-shell singlet state, and D_{4h} symmetry, wherein all CC bond distances are the same in the triplet state.[191–195] In the ground state, cyclobutadiene with D_{2h} symmetry is more stable than D_{4h}. However, all CC bond lengths in the cyclobutadiene ring in the optimized structures of cyclobutadiene dimers and superphanes are equal.[178–181] Thus, the author performed calculations for these two molecular structures as the monomer units in this study. The author refers to the dimer model with the D_{2h} unit as the D_{2h} model and the dimer model with the D_{4h} unit as the D_{4h} model. Cyclobutadiene molecules with D_{2h} and D_{4h} symmetry were obtained using geometry optimization in the closed-shell singlet and triplet states, respectively. The CC bond distance in the D_{4h} unit is 1.414 Å, while the distances for the single and double bonds in the D_{2h} unit are 1.577 Å and 1.333 Å, respectively. Interestingly, the single-bond distance is longer than that of ethane (1.54 Å). The closed-shell singlet state of cyclobutadiene is thus stabilized in energy by increasing the HOMO-LUMO gap caused by the significant bond alternation. These CC bond lengths are mostly consistent with those obtained from higher level calculations such as CCSD(T)[196] and CASPT2[195] calculations. To provide more robust validation for the presence of aromaticity, it is necessary to evaluate aromaticity using multiple methods.[163,197,198] The author employed $\mathrm{NICS(1)_{zz}}$,[71,199–202] iso-chemical shielding surface ($\mathrm{ICSS_{iso}}$) plots,[203,204] and anisotropy of the induced current density (ACID)[205,206] as indicators of aromaticity.

6.3. Results and Discussion

6.3.1. Evaluations of Aromaticity

Figure 6.1 shows $\mathrm{ICSS_{iso}}$ plots of cyclobutadiene dimers with D_{2h} and D_{4h} symmetry at π-stacking distances of 2.0 and 2.8 Å. Blue and yellow ICSS isosurfaces correspond to aromatic and antiaromatic, respectively. In the D_{4h} model, the ICSS appears only in blue at both π-stacking distances. From the figure, this model exhibits stacked aromaticity. Next, the author turns our attention to the ICSS of the D_{2h} model. The ICSS of the dimer at the π-stacking distance of 2.8 Å shows antiaromatic in the region that penetrates inside the two rings. On the other hand, the ICSS of the dimer at 2.0 Å appears only on the blue isosurface, similar to that of the D_{4h} model. Similar trends are obtained for results based on other indices of aromaticity (see Figure 6.2). The evaluation of aromaticity using DFT calculations may show different results due to different delocalization of π-electrons depending on the functional.[207] Thus the author performed $\mathrm{NICS(1)_{zz}}$ calculations using not only the B3LYP functional, but also CAM-B3LYP,[208] BHandHLYP,[209] and B3LYP-D3BJ,[210–212] and shows that the results for the B3LYP functional are qualitatively the same as for the other calculations (see Table 6.1 and 6.2). These outcomes indicate that the distance at which stacked aromaticity appears changes according to the symmetry.

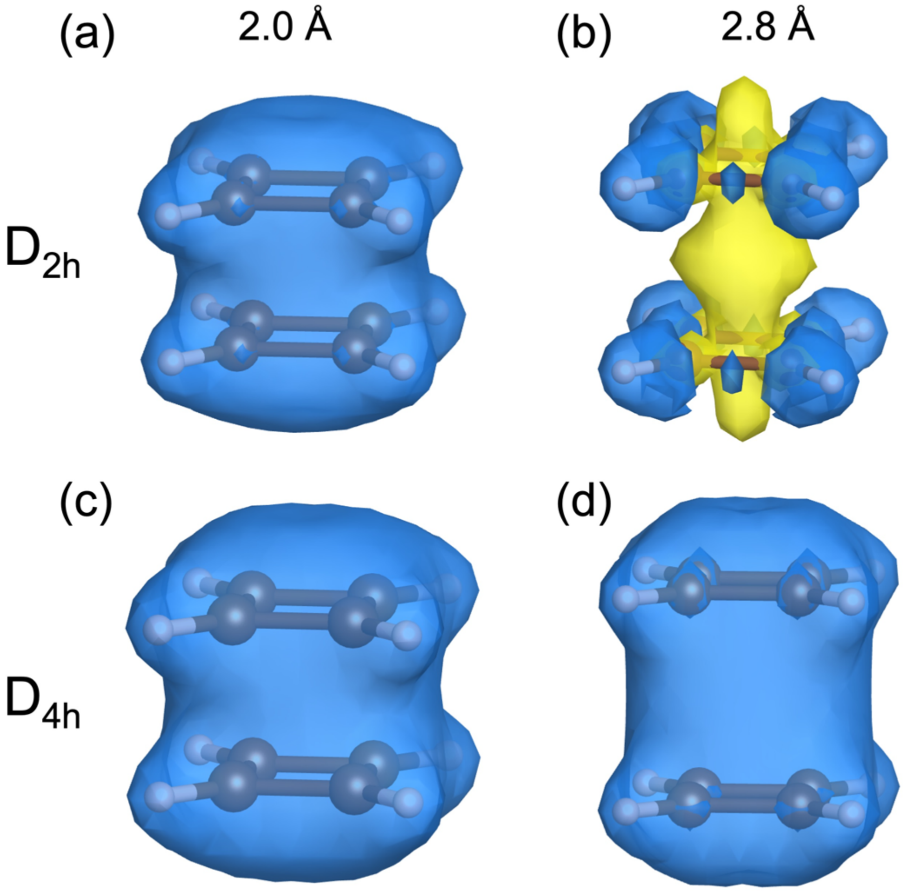

Figure 6.1. ICSS$_{\mathrm{iso}}$ plots for dimer of cyclobutadiene molecule with D$_{2h}$ (a, b) and D$_{4h}$ (c, d) symmetries at r = 2.0 and 2.8 Å. The isosurface value is set to 10 ppm. Blue and yellow surfaces are aromatic and antiaromatic regions, respectively. The structures were visualized by VESTA.[213]

Table 6.1. NICS(1)$_{zz}$ values for D$_{4h}$-cyclobutadiene dimers obtained by each functional at r = 2.0 and 2.8 Å.

	r = 2.0 Å		r = 2.8 Å	
	NICS(1)$_{\mathrm{in},zz}$	NICS(1)$_{\mathrm{out},zz}$	NICS(1)$_{\mathrm{in},zz}$	NICS(1)$_{\mathrm{out},zz}$
B3LYP	-35.1358	-17.8993	-29.9659	-19.7149
B3LYP-D3BJ	-35.0642	-17.8589	-29.9272	-19.6796
CAM-B3LYP	-36.3449	-18.2140	-30.9416	-20.0930
BHandHLYP	-37.8324	-19.2307	-32.0767	-21.0087

Table 6.2. NICS(1)$_{zz}$ values for D$_{2h}$-cyclobutadiene dimers obtained by each functional at r = 2.0 and 2.8 Å.

	r = 2.0 Å		r = 2.8 Å	
	NICS(1)$_{in,zz}$	NICS(1)$_{out,zz}$	NICS(1)$_{in,zz}$	NICS(1)$_{out,zz}$
B3LYP	-26.7943	-11.7544	65.4438	56.4281
B3LYP-D3BJ	-26.6330	-11.6485	64.9304	56.0003
CAM-B3LYP	-28.1494	-12.0854	66.3330	57.3142
BHandHLYP	-29.7486	-13.2138	67.1535	58.2389

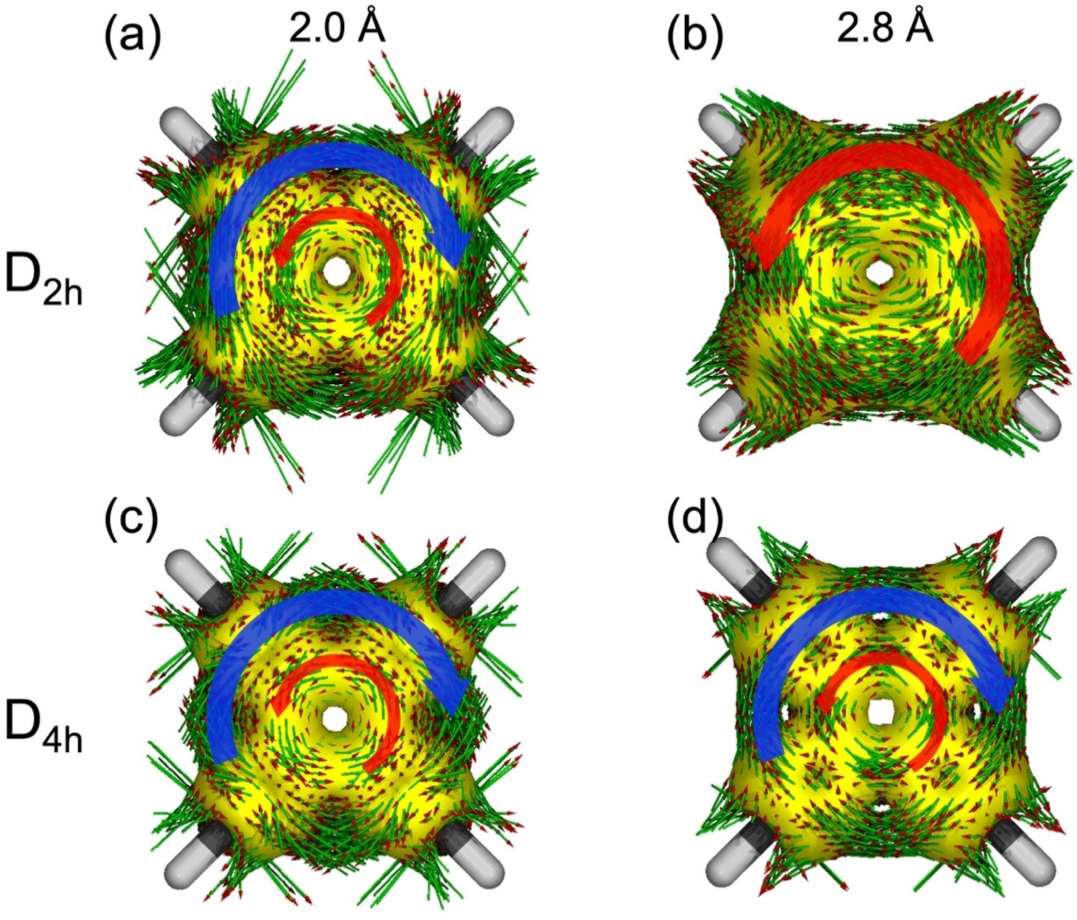

Figure 6.2. ACID of cyclobutadiene dimers with D$_{2h}$ (a, b) and D$_{4h}$ (c, d) symmetry at r = 2.0 (left) and 2.8 Å (right). Clockwise and counterclockwise ring currents correspond to aromatic and antiaromatic, respectively.

6.3.2. Frontier Orbital View for the D_{4h} Dimer

The author discusses the reasons behind the different manners in which the stacked aromaticity appears in different symmetries in accordance with the molecular orbitals. Figure 6.3 shows the relationship between the π-stacking distance and the energy levels of the Kohn-Sham orbitals in the D_{4h} model, HOMOs and LUMOs, and the orbital interactions between the two units in the D_{4h} model. In Figure 6.3a, the blue and red lines indicate the occupied and unoccupied orbitals, respectively. The HOMOs and LUMOs of the D_{4h} model are degenerate. The HOMO-LUMO gap of this model increases as the π-stacking distance decreases. The relationship between the π-stacking distance and the HOMO-LUMO gap can be explained according to the orbital interactions between the two monomers. The D_{4h}-cyclobutadiene has degenerate SOMOs (e_g). When the monomer units are π-stacked in a face-to-face orientation, the SOMOs of the monomers interact with each other to form symmetric (referred to as $S(e_g)$) and antisymmetric (referred to as $A(e_g)$) orbitals with respect to the symmetry plane between the monomer units (Figure 6.3b). Here, $S(e_g)$s are stabilized because they are bonding orbitals, whereas $A(e_g)$s are destabilized because they are antibonding orbitals. Consequently, $S(e_g)$s become HOMOs and $A(e_g)$s become LUMOs (Figure 6.3c). The orbital overlap between the two monomer units increases as the π-stacking distance decreases. Therefore, the orbital energies of $S(e_g)$s decrease and those of $A(e_g)$s increase. This is the primary reason why the HOMO-LUMO gap increases as the π-stacking distance decreases.

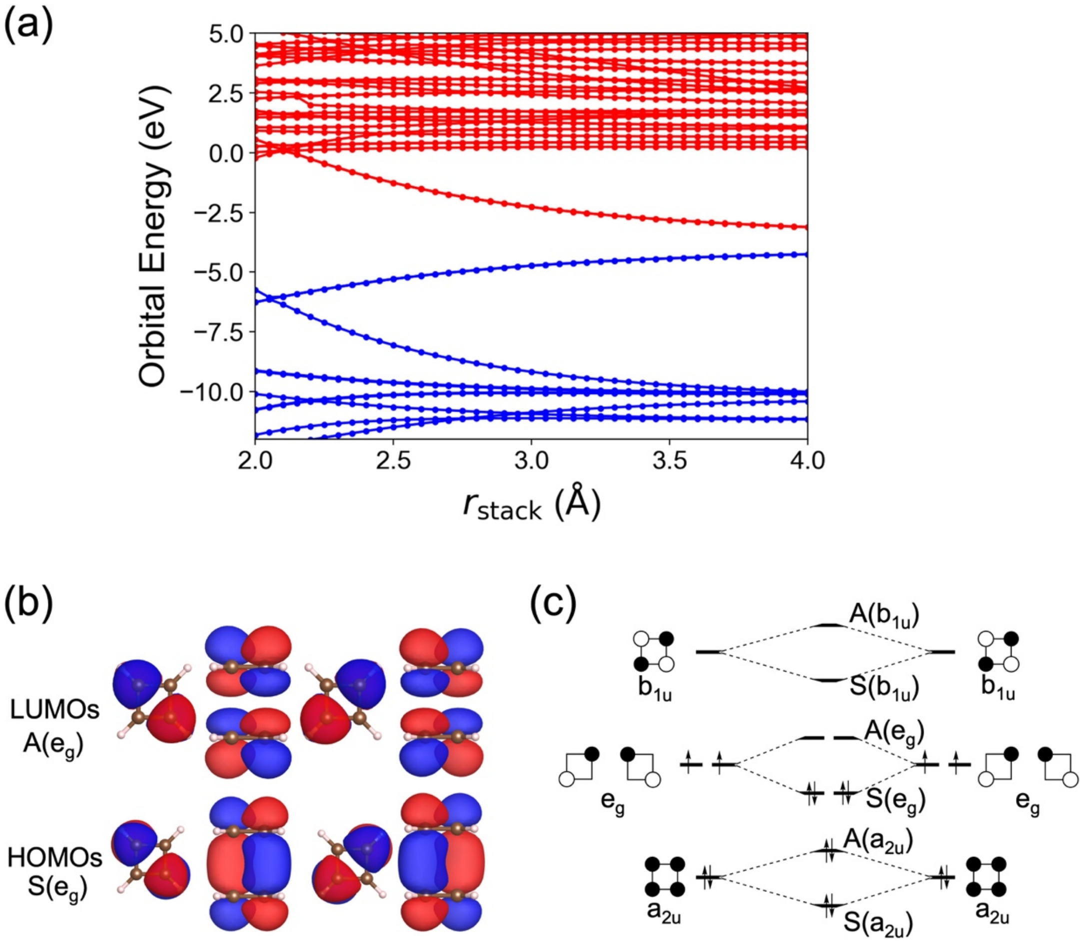

Figure 6.3. (a) Kohn-Sham orbital levels plotted as a function of the distance between D_{4h}-cyclobutadiene rings, (b) top (left) and side (right) views of frontier orbitals for D_{4h} model, (c) orbital interaction diagram between two D_{4h}-cyclobutadiene monomers. Blue and red lines in Figure 6.3a indicate the occupied and unoccupied orbitals, respectively. Labels of MOs in Figure 6.3b, and c are represented using symmetry of orbitals with respect to plane of symmetry between two monomer units (S/A) and symmetry of fragment orbital with monomer unit.

6.3.3. Frontier Orbital View for the D_{2h} Dimer

Figure 6.4 shows the relationship between the π-stacking distance and the energy levels of the Kohn-Sham orbitals in the D_{2h} model, HOMO and LUMO distributions at π-stacking distances of 2.8 Å and 2.0 Å, and the orbital interaction between the two units in the D_{2h} model. For π-stacking distances greater than 2.55 Å, the HOMO-LUMO gap of the dimer decreases with the π-stacking distance. For π-stacking distances less than 2.5 Å, the HOMO-LUMO gap of the dimer increases as the π-stacking distance decreases, and this behavior is similar to that of the D_{4h} model. From the molecular orbitals at π-stacking distances above 2.55 Å, it can be inferred that the HOMO and LUMO are antisymmetric ($A(b_{3g})$) and symmetric ($S(b_{2g})$) with respect to the symmetry plane between monomer units, respectively. On the other hand, at π-stacking distances less than 2.5 Å, the HOMO and LUMO are $S(b_{2g})$ and $A(b_{3g})$, respectively. These molecular orbitals indicate that orbital crossing occurs between 2.5 Å and 2.55 Å (Figure 6.4c and d). This orbital crossing causes the switching of the interaction between the units from antibonding to bonding. To verify the change in interaction between the units, the author performed an analysis using the Wiberg bond index (WBI)[214], which helps evaluate the bond strength from the electron density between two atoms (Figure 6.5). The WBI analysis was performed using NBO 7.0.[215] The author evaluated the WBI by calculating the average of the WBI between the carbon atom of one cyclobutadiene and the closest carbon atom in the other cyclobutadiene. The WBIs of the D_{4h} model are 0.2494 and 0.2537 at 4.0 Å and 2.5 Å, respectively. The WBIs of the D_{2h} model are 0.0007 and 0.0097 at 4.0 Å and 2.55 Å, indicating antiaromaticity, while they are 0.2528 at 2.5 Å, indicating aromaticity, respectively. The WBI in the antiaromatic region of the D_{2h} model is similar to that of the benzene face-to-face stack.[216] The values of the WBIs in the aromatic regions of the D_{4h} and D_{2h} models between the two monomer units are one. Therefore, in the aromatic region, the bond order is equivalent to a single bond through the rings. These outcomes indicate that the interactions between the units change because of the interchange of HOMO and LUMO. This further results in the through-space interaction between the two units, and this may result in stacked aromaticity, as reported in previous studies.[178,181,182]

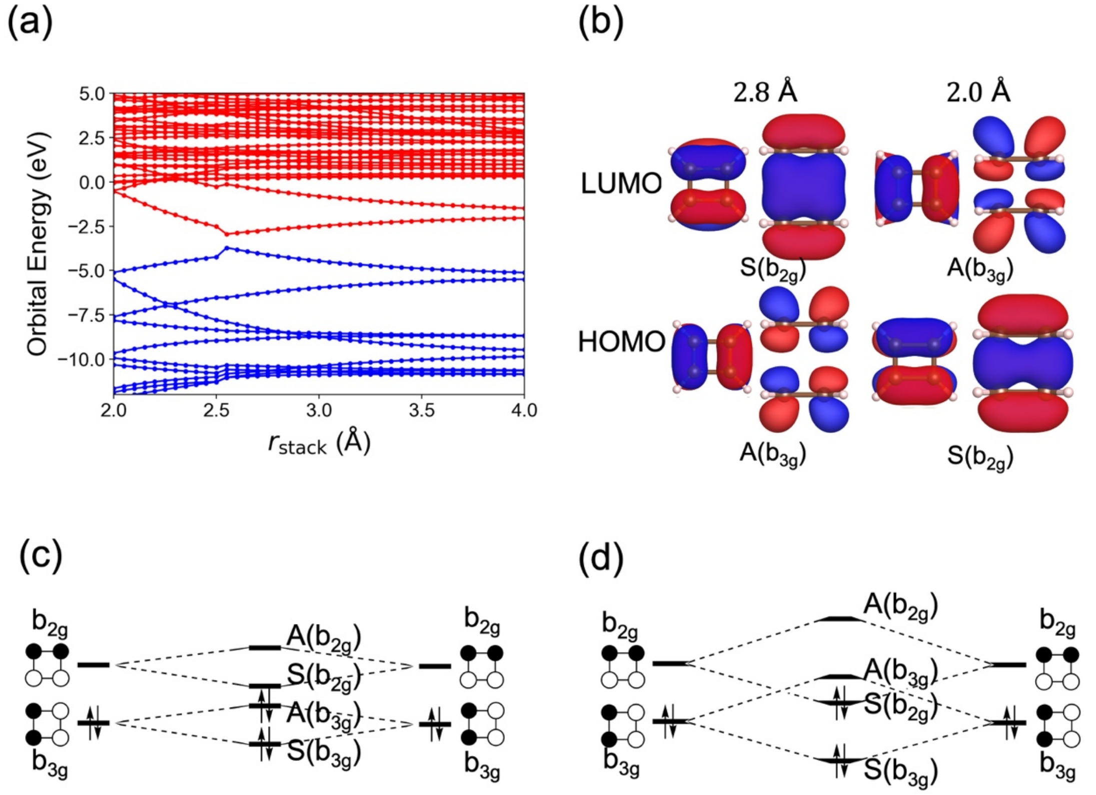

Figure 6.4. (a) Kohn-Sham orbital levels plotted as a function of the distance between D_{2h}-cyclobutadiene rings, (b) top (left) and side (right) views of frontier orbitals for D_{2h} model, (c) orbital interaction diagram between two D_{2h}-cyclobutadiene monomers. Blue and red lines in Figure 6.4a indicate occupied and unoccupied orbitals, respectively. Labels of MOs in Figure 6.4b, and c are represented by the symmetry of the orbitals according to the plane of symmetry between two monomer units (S/A) and symmetry of fragment orbital with monomer unit.

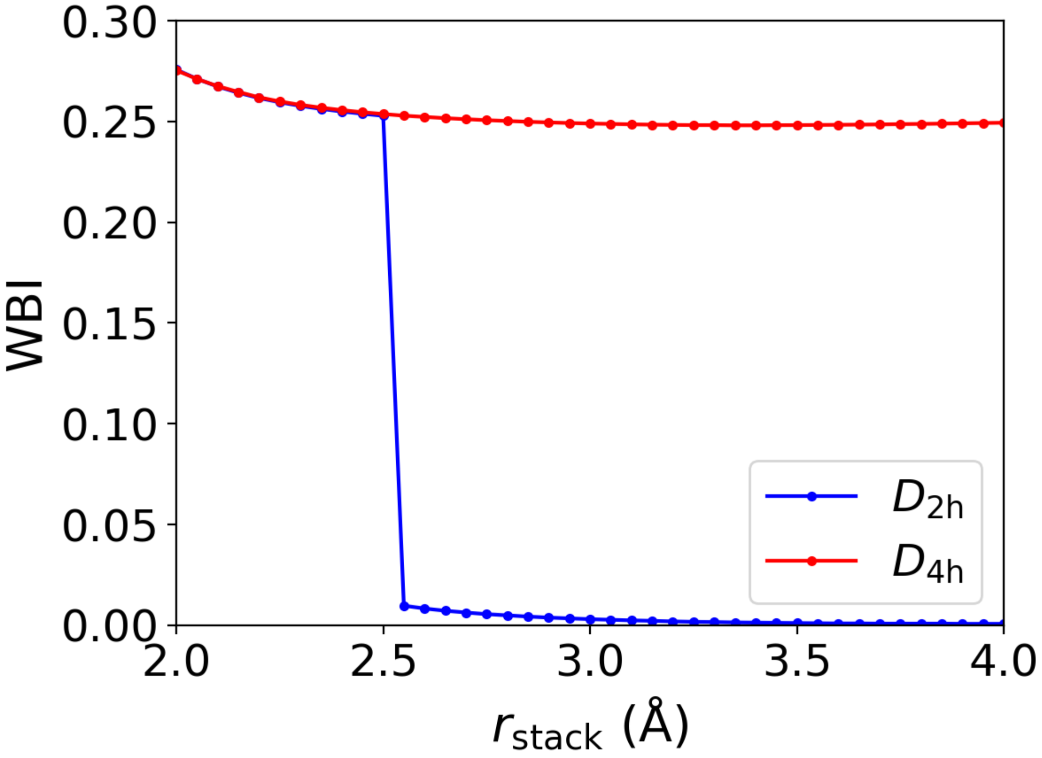

Figure 6.5. WBIs plot as a function of distance between two cyclobutadiene rings. WBIs were obtained by averaging WBIs between carbon atom of one cyclobutadiene the carbon atom closest to it in other cyclobutadiene.

6.3.4. Relationship between the Stacked Aromaticity and HOMO–LUMO gap of the monomer

The orbital interactions in the D_{2h} model suggest that the smaller the HOMO-LUMO gap of the monomer, the greater the maximum distance at which it exhibits stacked aromaticity. The D_{2h}-cyclobutadiene monomer used in this study possesses a HOMO-LUMO gap of 3.69 eV. The HOMO-LUMO gap of cyclobutadiene monomer is caused by bond alternation due to pseudo-Jahn-Teller distortion.[85,191–193,195] Thus, the HOMO-LUMO gap of cyclobutadiene can be changed by changing the degree of bond alternation, i.e., the CC bond length. The author has shown that the HOMO-LUMO gap of cyclobutadiene undergoing bond alternation is linearly correlated with the degree of bond alternation using the Hückel method. A detailed discussion is given in the Appendix 6.5.1. To evaluate the relationship between the HOMO-LUMO gap and the π-stacking distance at which stacked aromaticity develops, the author controlled the HOMO-LUMO gap by tuning the CC bond distance of cyclobutadiene, and the author investigated the maximum π-stacking distance at which stacked aromaticity is manifested when the molecule is used as a unit using DFT calculations. The long (short) bond length in cyclobutadiene in the intermediate state between the D_{4h} and D_{2h} units $r_{\mathrm{L(S)}}$ is defined as follows:

$$r_{\mathrm{L(S)}} = r_{\mathrm{D_{4h}}} + \delta\left(r_{\mathrm{L(S),D_{2h}}} - r_{\mathrm{D_{4h}}}\right), \tag{6.1}$$

where $r_{\mathrm{D_{2h}}}$ and $r_{\mathrm{D_{4h}}}$ are the CC bond length corresponding to r in D_{2h} and D_{4h}, and δ is a real number between 0 and 1, respectively. When δ is 0, it corresponds to D_{4h}-cyclobutadiene, and when δ is 1, it corresponds to D_{2h}-cyclobutadiene; the author thus refers to them as bond alternation indices. The author will refer to cyclobutadiene with δ greater than 0 and less than 1 as δ-cyclobutadiene. Here, D_{4h}-cyclobutadiene is stable in the triplet state. In the open-shell state, the HOMO-LUMO gap is not uniquely determined, unlike the HOMO-LUMO gap in the closed-shell state, because the orbital energy varies with the spin. For a clearer understanding of the relationship between the HOMO-LUMO gap and δ, the author compared the energies of the closed-shell singlet and triplet states of the cyclobutadiene molecule and used δ in the range where the closed-shell singlet is stable. Figure 6.6 shows the energy plots for all spin states of cyclobutadiene with all bond alternation indices. The r_{L} and r_{S} of δ-cyclobutadiene at δ = 0.4 are 1.479 and 1.382, respectively, which is roughly consistent with the CC bond length of the previous study (r_{L} = 1.488, r_{S} = 1.392).[217] Therefore, the author performed HOMO-LUMO gap calculations with cyclobutadiene as the unit in the δ range 0.4–1.0. Figure 6.7 shows the relationship between the unit δ and the HOMO-LUMO gap. The plot shows that δ and the HOMO-LUMO gap are linearly correlated (correlation coefficient is 0.9998). Thus, the HOMO-LUMO gap can be controlled by tuning δ in the DFT calculation and the Hückel method. The relationship between the HOMO-LUMO gap of the δ-cyclobutadiene monomer and the maximum distance at which the δ-cyclobutadiene dimer exhibits stacked aromaticity (r_{SA}) is plotted in Figure 6.8. The correlation coefficient between the HOMO-LUMO gap and r_{SA} of the δ-cyclobutadiene monomer is -0.9939. This further indicates that as the HOMO-LUMO gap of the monomer unit increases, r_{SA} decreases. Thus, it is clear that to develop stacked aromaticity over long distances, it is necessary to employ molecules with small HOMO-LUMO gaps as stacking units.

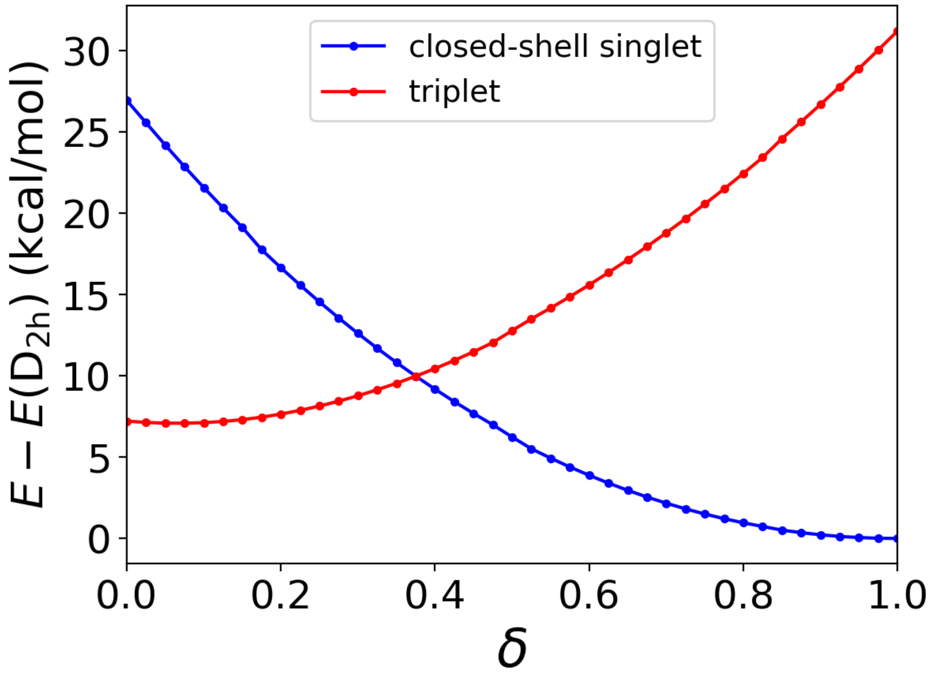

Figure 6.6. State energies for δ-cyclobutadiene as a function of bond alternation index.

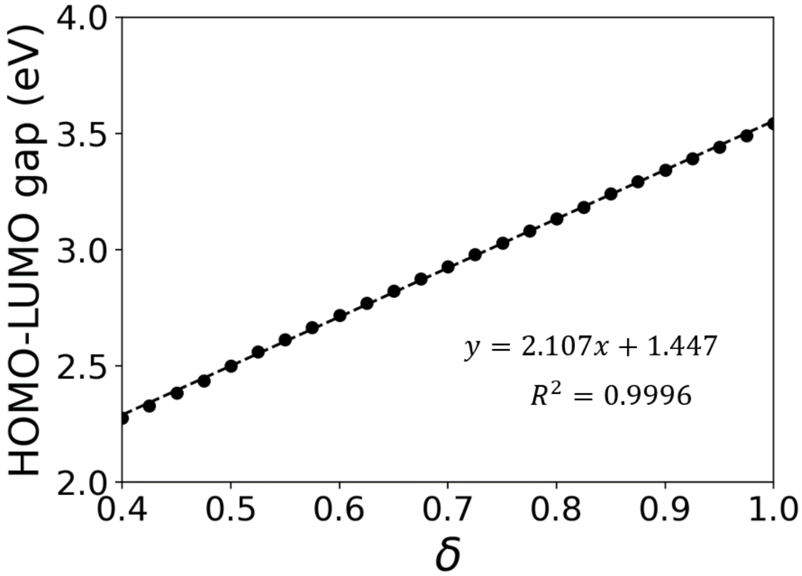

Figure 6.7. HOMO-LUMO gap of δ-cyclobutadiene monomers as a function of bond alternation index. Plotted range is 0.4 ≤ δ ≤ 1.0, where closed-shell singlet becomes more stable than the triplet. Black dashed line indicates linear regression line. Correlation coefficient for this plot is 0.9998.

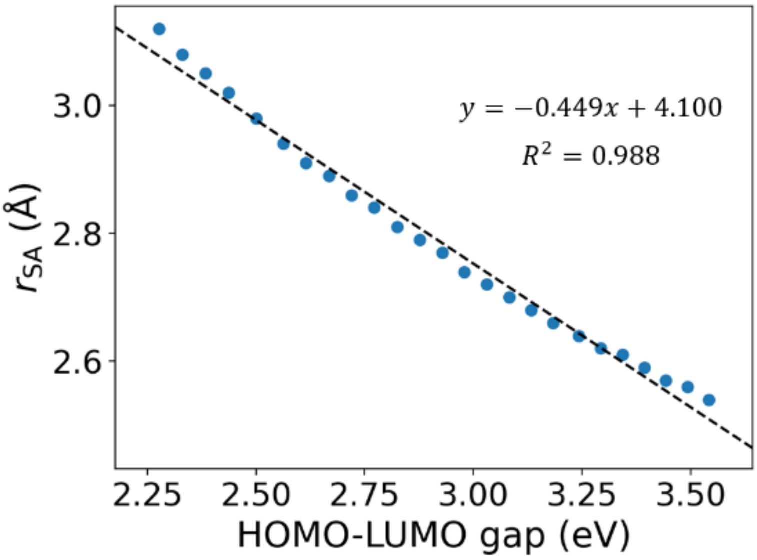

Figure 6.8. Threshold value of π-stacking distance for appearance of stacked aromaticity as a function of HOMO-LUMO gap of cyclobutadiene units with bond alternation index δ. Black dashed line indicates linear regression line.

6.4. Conclusion

It has been theoretically predicted that dimers with stacked antiaromatic molecules exhibit stacked aromaticity. However, experiments show that such systems do not exhibit stacked aromaticity despite the stacking of antiaromatic molecules. In this study, the author investigated the changes in aromaticity and molecular orbital interactions for a face-to-face dimer model with cyclobutadiene, through DFT calculations with fixed symmetry. The author found that the dimer with D_{4h}-cyclobutadiene units is always aromatic, while the dimer with D_{2h}-cyclobutadiene units is antiaromatic at larger π -stacking distances and aromatic at smaller distances. The D_{4h}-cyclobutadiene dimer forms degenerate HOMOs and degenerate LUMOs based on the interaction between the degenerate SOMOs of the monomer units. The HOMO-LUMO gap increases as the π-stacking distance decreases, mainly because of the orbital overlap. On the other hand, D_{2h}-cyclobutadiene has a HOMO-LUMO gap because of the pseudo-Jahn-Teller distortion. In D_{2h}-cyclobutadiene, the HOMO-to-HOMO and LUMO-to-LUMO interactions of the two monomer units result in a change in the dimer HOMO-LUMO gap in the direction at which it decreases. When the monomer units are at a specific distance, the HOMO of the dimer unit, corresponding to the antibonding between the monomer units and the LUMO of the dimer unit, corresponding to bonding between the monomer units, are interchanged. This interchange of molecular orbitals may result in an increase in the bond strength between the monomer units, thereby inducing stacked aromaticity. Furthermore, the author has demonstrated that the distance of stacked aromaticity can be controlled by engineering the HOMO-LUMO gap, which can be attained by adjusting the degree of bond alternation of cyclobutadiene monomer units. These results are expected to contribute to design guidelines for molecules with stacked aromaticity.

6.5. Appendix

6.5.1. Analysis of the relationship between bond alternation and HOMO-LUMO gap of cyclobutadiene using the Hückel method

First, the author defines the Hamiltonian of cyclobutadiene with bond alternation. The Hamiltonian of cyclobutadiene according to the degree of bond alternation as δ is as follows:

$$\mathbf{H} = \begin{pmatrix} 0 & 1+\delta & 0 & 1-\delta \\ 1+\delta & 0 & 1-\delta & 0 \\ 0 & 1-\delta & 0 & 1+\delta \\ 1-\delta & 0 & 1+\delta & 0 \end{pmatrix}, \tag{S6.1}$$

where the Coulomb integral α_C of the carbon atom is set to zero and the resonance integral β_{CC} between the carbon-carbon bonds is set to one. It is assumed that the absolute value of the change in the resonance integral between carbon-carbon bonds due to bond alternation is equal. The orbital energy and wave function of cyclobutadiene under bond alternation were obtained by solving the eigenvalue problem for Eq. S1.

$$\varepsilon_1 = 2\ (\beta), \psi_1 = \frac{1}{2}(\phi_1 + \phi_2 + \phi_3 + \phi_4) \tag{S6.2}$$

$$\varepsilon_2 = 2\delta\ (\beta), \psi_2 = \frac{1}{2}(\phi_1 + \phi_2 - \phi_3 - \phi_4) \tag{S6.3}$$

$$\varepsilon_3 = -2\delta\ (\beta), \psi_3 = \frac{1}{2}(\phi_1 - \phi_2 - \phi_3 + \phi_4) \tag{S6.4}$$

$$\varepsilon_4 = -2\ (\beta), \psi_4 = \frac{1}{2}(\phi_1 - \phi_2 + \phi_3 - \phi_4) \tag{S6.5}$$

It should be noted that the orbital energy is a unit of β, and ε_1 and ε_4 are independent of the value of δ. On the other hand, as δ increases, ε_2 shifts toward lower energies and ε_3 toward higher energies. In addition, ε_2 and ε_3 are linearly correlated with δ. The HOMO-LUMO gap of cyclobutadiene in bond alternation is expressed as 4δ.

Chapter 7

General Conclusions

In this thesis, the electrical conduction properties of π-conjugated single-molecule junctions and the stacked aromaticity related to the stability of highly conductive molecules have been studied on the basis of the NEGF method, frontier orbital theory, and graph theory.

In Chapter 3, the author proposed a classification of conducting systems in parallel circuits based on aromaticity. The author performed a theoretical study using non-equilibrium Green's functions and showed that these various results are closely related to the presence or absence of aromatic rings. This study characterizes molecular conductance properties based on frontier orbital theory, orbital interactions, and the local transmission concept. The author also clarified the mathematical aspects of the relationship between atomic connectivity and electronic conductivity.

In Chapter 4, the author has improved the relation between polyene bond alternation and conductance by Tsuji et al. and successfully reproduced the behavior in which the reversed conductance decay disappears. By using a Hamiltonian that replaces the electrode interaction as simple parameters, the disappearance of the reversed conductance decay can be reproduced. This modification made it possible to analyze the conduction properties using the orbital law for electron transport.

In Chapter 5, the author used Sachs graph theory to formulate the conduction properties of a single molecular junction consisting of a molecule in which one of the carbon atoms of the alternant hydrocarbon is replaced by a heteroatom. The derived equation differs from the graph of the parent structure in that it contains odd and even powers of the adjacency matrix. These powers correspond to odd and even length walks. Furthermore, since heteroatoms are represented in the graph as self-loops of unit length, an odd number of passes through a self-loop changes the parity of the walk length. To confirm the effects of heteroatoms on conduction in real samples, the author analyzed the conduction behavior of meta-linked molecular junctions consisting of heterocyclic six-membered rings, whose conduction properties have already been experimentally determined, based on the number of walks enumerated.

In Chapter 6, the author investigated the mechanism of stacked aromatics using cyclobutadiene. When the anti-aromatic molecules are stacked face-to-face, orbital interactions between the degenerate SOMOs of the monomer units result in a larger energy gap between the degenerate HOMOs and LUMOs of the dimers. In the case of cyclobutadiene, bond alternation splits the two SOMOs of the monomer unit into HOMOs and LUMOs. When the monomer units are within a certain distance, the HOMO and LUMO of the dimer are swapped, corresponding to antibonding and bonding between the units, respectively. The author revealed that the alternation of the molecular orbitals causes the stacking aromaticity.

The author expect that the results of these studies from a theoretical standpoint will be an important tool that will provide much help in designing integrated circuits using single-molecule devices. This is expected to provide new insights into the properties of various types of quantum interference in single-molecule junctions. This approach will provide comprehensive knowledge of the conduction properties of single-molecule junctions and will lay the groundwork for the design of future single-molecule devices.

References

1 A. Aviram and M. A. Ratner, *Chem. Phys. Lett.*, 1974, **29**, 277–283.

2 M. A. Reed, C. Zhou, C. J. Muller, T. P. Burgin and J. M. Tour, *Science*, 1997, **278**, 252–254.

3 B. Xu and N. J. Tao, *Science*, 2003, **301**, 1221–1223.

4 B. Xu, X. Xiao and N. J. Tao, *J. Am. Chem. Soc.*, 2003, **125**, 16164–16165.

5 J. Park, A. N. Pasupathy, J. I. Goldsmith, C. Chang, Y. Yalsh, J. R. Petta, M. Rinkoski, J. P. Sethna, H. D. Abruña, P. L. McEuen and D. C. Ralph, *Nature*, 2002, **417**, 722–725.

6 Y. Cao, S. Dong, S. Liu, L. He, L. Gan, X. Yu, M. L. Steigerwald, X. Wu, Z. Liu and X. Guo, *Angew. Chemie Int. Ed.*, 2012, **51**, 12228–12232.

7 L. Li, J. Z. Low, J. Wilhelm, G. Liao, S. Gunasekaran, C. R. Prindle, R. L. Starr, D. Golze, C. Nuckolls, M. L. Steigerwald, F. Evers, L. M. Campos, X. Yin and L. Venkataraman, *Nat. Chem.*, 2022, **14**, 1061–1067.

8 R. Gupta, J. A. Fereiro, A. Bayat, A. Pritam, M. Zharnikov and P. C. Mondal, *Nat. Rev. Chem.*, 2023, **7**, 106–122.

9 M. L. Perrin, E. Burzurí and H. S. J. Van Der Zant, *Chem. Soc. Rev.*, 2015, **44**, 902–919.

10 G. Ke, C. Duan, F. Huang and X. Guo, *InfoMat*, 2020, **2**, 92–112.

11 D. Aravena and E. Ruiz, *J. Am. Chem. Soc.*, 2012, **134**, 777–779.

12 S. Shaik, D. Mandal and R. Ramanan, *Nat. Chem.*, 2016, **8**, 1091–1098.

13 X. Xie, P. Li, Y. Xu, L. Zhou, Y. Yan, L. Xie, C. Jia and X. Guo, *ACS Nano*, 2022, **16**, 3476–3505.

14 R. Landauer, *IBM J. Res. Dev.*, 1957, **1**, 223–231.

15 M. Magoga and C. Joachim, *Phys. Rev. B*, 1999, **59**, 16011–16021.

16 C. Joachim, *Nat. Nanotechnol.*, 2012, **7**, 620–621.

17 T. Markussen, R. Stadler and K. S. Thygesen, *Nano Lett.*, 2010, **10**, 4260–4265.

18 H. Valkenier, C. M. Guédon, T. Markussen, K. S. Thygesen, S. J. Van Der Molen and J. C. Hummelen, *Phys. Chem. Chem. Phys.*, 2014, 16, 653–662.

19 G. C. Solomon, C. Herrmann, T. Hansen, V. Mujica and M. A. Ratner, *Nat. Chem.*, 2010, **2**, 223–228.

20 K. Yoshizawa, *Acc. Chem. Res.*, 2012, **45**, 1612–1621.

21 M. Kiguchi, H. Nakamura, Y. Takahashi, T. Takahashi and T. Ohto, *J. Phys. Chem. C*, 2010, **114**, 22254–22261.

22 G. Yang, H. Wu, J. Wei, J. Zheng, Z. Chen, J. Liu, J. Shi, Y. Yang and W. Hong,

Chinese Chem. Lett., 2018, **29**, 147–150.

23 K. Yoshizawa, T. Tada and A. Staykov, *J. Am. Chem. Soc.*, 2008, **130**, 9406–9413.

24 Y. Tsuji, E. Estrada, R. Movassagh and R. Hoffmann, *Chem. Rev.*, 2018, **118**, 4887–4911.

25 M. Büttiker, Y. Imry, R. Landauer and S. Pinhas, *Phys. Rev. B*, 1985, **31**, 6207–6215.

26 S. Datta, *Quantum Transport: Atom to Transistor*, Cambridge University Press, Cambridge, U.K., 2005.

27 E. G. Emberly and G. Kirczenow, *J. Phys. Condens. Matter*, 1999, **11**, 6911–6926.

28 R. P. Feynman, R. B. Leighton and M. Sands, *Lectures on Physics*, Addison-Wesley, 1965.

29 J. W. Essam and M. E. Fisher, *Rev. Mod. Phys.*, 1970, **42**, 271–288.

30 D. J. Klein and M. Randić, *J. Math. Chem.*, 1993, **12**, 81–95.

31 D. Babić, D. J. Klein, I. Lukovits, S. Nikolić and N. Trinajstić, *Int. J. Quantum Chem.*, 2002, **90**, 166–176.

32 H. Vazquez, R. Skouta, S. Schneebeli, M. Kamenetska, R. Breslow, L. Venkataraman and M. S. Hybertsen, *Nat. Nanotechnol.*, 2012, **7**, 663–667.

33 L. Y. Hsu and B. Y. Jin, *Chem. Phys.*, 2009, **355**, 177–182.

34 G. C. Solomon, *Nat. Chem.*, 2015, 7, 621–622.

35 X. Zhao, G. Kastlunger and R. Stadler, *Phys. Rev. B*, , DOI:10.1103/PhysRevB.96.085421.

36 K. P. Dou and C. C. Kaun, *J. Phys. Chem. C*, 2016, **120**, 18939–18944.

37 H. Sadeghi, J. A. Mol, C. S. Lau, G. A. D. Briggs, J. Warner and C. J. Lambert, *Proc. Natl. Acad. Sci.*, 2015, **112**, 2658–2663.

38 R. E. Sparks, V. M. García-Suárez, D. Z. Manrique and C. J. Lambert, *Phys. Rev. B*, 2011, **83**, 075437.

39 S. V. Aradhya and L. Venkataraman, *Nat. Nanotechnol.*, 2013, 8, 399–410.

40 Z. Li, M. Smeu, A. Rives, V. Maraval, R. Chauvin, M. A. Ratner and E. Borguet, *Nat. Commun.*, 2015, **6**, 6321.

41 A. Kleshchonok, R. Gutierrez and G. Cuniberti, *Nanoscale*, 2015, **7**, 13967–13973.

42 C. J. Lambert, *Chem. Soc. Rev.*, 2015, 44, 875–888.

43 A. Borges, J. Xia, S. H. Liu, L. Venkataraman and G. C. Solomon, *Nano Lett.*, 2017, **17**, 4436–4442.

44 G. Gryn'Ova and C. Corminboeuf, *J. Phys. Chem. Lett.*, 2019, **10**, 825–830.

45 Y. Zhou, X. Zheng, Z. Q. Cheng and K. Q. Chen, *J. Phys. Chem. C*, 2019, **123**, 10462–10468.

46 G. C. Solomon, D. Q. Andrews, R. P. Van Duyne and M. A. Ratner, *ChemPhysChem*, 2009, **10**, 257–264.

47 M. Brandbyge, J.-L. Mozos, P. Ordejón, J. Taylor and K. Stokbro, *Phys. Rev. B*, 2002, **65**, 165401.

48 T. Tada, M. Kondo and K. Yoshizawa, *J. Chem. Phys.*, 2004, **121**, 8050–8057.

49 P. Hohenberg and W. Kohn, *Phys. Rev.*, 1964, **136**, B864–B871.

50 W. Kohn and L. J. Sham, *Phys. Rev.*, 1965, **140**, A1133–A1138.

51 K. Fukui, T. Yonezawa and H. Shingu, *J. Chem. Phys.*, 1952, **20**, 722–725.

52 K. Fukui, T. Yonezawa, C. Nagata and H. Shingu, *J. Chem. Phys.*, 1954, **1433**, 1433–1442.

53 K. Fukui, N. Koga and H. Fujimoto, *J. Am. Chem. Soc.*, 1981, **103**, 196–197.

54 K. Fukui, *Science*, 1982, **218**, 747–754.

55 T. Tada and K. Yoshizawa, *ChemPhysChem*, 2002, **3**, 1035–1037.

56 A. D. Becke, *J. Chem. Phys.*, 1993, **98**, 5648–5652.

57 C. Lee, W. Yang and R. G. Parr, *Phys. Rev. B*, 1988, **37**, 785–789.

58 R. Krishnan, J. S. Binkley, R. Seeger and J. A. Pople, *J. Chem. Phys.*, 1980, **72**, 650–654.

59 M. J. Frisch, J. A. Pople and J. S. Binkley, *J. Chem. Phys.*, 1984, **80**, 3265–3269.

60 A. Bilić, J. R. Reimers and N. S. Hush, *J. Chem. Phys.*, 2005, **122**, 094708.

61 P. J. Hay and W. R. Wadt, *J. Chem. Phys.*, 1985, **82**, 270–283.

62 T. H. Dunning Jr. and P. Heffrey Hay, *Gaussian Basis Sets for Molecular Calculations*, Springer, Boston, MA, vol. 3., 1977.

63 C. J. O. Verzijl, J. S. Seldenthuis and J. M. Thijssen, *J. Chem. Phys.*, 2013, **138**, 094102.

64 C. Herrmann, G. C. Solomon and M. A. Ratner, *J. Chem. Phys.*, 2011, **134**, 224306.

65 M. J. Frisch, G. W. Trucks, H. B. Schlegel, G. E. Scuseria, M. A. Robb, J. R. Cheeseman, G. Scalmani, V. Barone, B. Mennucci, G. A. Petersson, H. Nakatsuji, M. Caricato, X. Li, H. P. Hratchian, A. F. Izmaylov, J. Bloino, G. Zheng, J. L. Sonnenberg, M. Hada, M. Ehara, K. Toyota, R. Fukuda, J. Hasegawa, M. Ishida, T. Nakajima, Y. Honda, O. Kitao, H. Nakai, T. Vreven, J. A. Montgomery Jr., J. E. Peralta, F. Ogliaro, M. Bearpark, J. J. Heyd, E. Brothers, K. N. Kudin, V. N. Staroverov, R. Kobayashi, J. Normand, K.

Raghavachari, A. Rendell, J. C. Burant, S. S. Iyengar, J. Tomasi, M. Cossi, N. Rega, J. M. Millam, M. Klene, J. E. Knox, J. B. Cross, V. Bakken, C. Adamo, J. Jaramillo, R. Gomperts, R. E. Stratmann, O. Yazyev, A. J. Austin, R. Cammi, C. Pomelli, J. W. Ochterski, R. L. Martin, K. Morokuma, V. G. Zakrzewski, G. A. Voth, P. Salvador, J. J. Dannenberg, S. Dapprich, A. D. Daniels, Ö. Farkas, J. B. Foresman, J. V Ortiz, J. Cioslowski and D. J. Fox, 2016.

66 M. Deffner, L. Gross, T. Steenbock, B. A. Voigt, G. C. Solomon and C. Herrmann, 2010.

67 C. Herrmann, G. C. Solomon and M. A. Ratner, *J. Am. Chem. Soc.*, 2010, **132**, 3682–3684.

68 C. Herrmann, G. C. Solomon, J. E. Subotnik, V. Mujica and M. A. Ratner, *J. Chem. Phys.*, 2010, **132**, 024103.

69 Y. Carissan, N. Goudard, D. Hagebaum-Reignier and S. Humbel, *J. Phys. Conf. Ser.*, 2016, **738**, 12015.

70 R. Breslow and F. W. Foss, *J. Phys. Condens. Matter*, 2008, **20**, 374104.

71 P. von R. Schleyer, C. Maerker, A. Dransfeld, H. Jiao and N. J. R. Van Eikema Hommes, *J. Am. Chem. Soc.*, 1996, **118**, 6317–6318.

72 H. Jiao, P. Von Ragué Schleyer, Y. Mo, M. A. McAllister and T. T. Tidwell, *J. Am. Chem. Soc.*, 1997, **119**, 7075–7083.

73 Z. Chen, C. S. Wannere, C. Corminboeuf, R. Puchta and P. v. R. Schleyer, *Chem. Rev.*, 2005, **105**, 3842.

74 W. Chen, H. Li, J. R. Widawsky, C. Appayee, L. Venkataraman and R. Breslow, *J. Am. Chem. Soc.*, 2014, **136**, 918–920.

75 Z. Xie, X. L. Ji, Y. Song, M. Z. Wei and C. K. Wang, *Chem. Phys. Lett.*, 2015, **639**, 131–134.

76 A. Borges and G. C. Solomon, *J. Phys. Chem. C*, 2017, **121**, 8272–8279.

77 T. Stuyver, S. Fias, P. Geerlings, F. De Proft and M. Alonso, *J. Phys. Chem. C*, 2018, **122**, 19842–19856.

78 *Comment*, .

79 S. Inagaki, H. Fujimoto and K. Fukui, *J. Am. Chem. Soc.*, 1976, **98**, 4054–4061.

80 W. T. Borden and E. R. Davidson, *J. Am. Chem. Soc.*, 1977, **99**, 4587–4594.

81 Y. Tsuji and K. Yoshizawa, *J. Phys. Chem. C*, 2017, **121**, 9621–9626.

82 R. B. Woodward and R. Hoffmann, *Angew. Chemie Int. Ed.*, 1969, **8**, 781–853.

83 T. A. Albright, J. K. Burdett and M. H. Whangbo, *Orbital Interactions in Chemistry: Second Edition*, 2013.

84 T. Hansen, G. C. Solomon, D. Q. Andrews and M. A. Ratner, *J. Chem. Phys.*,

2009, **131**, 194704.

85 Y. Tsuji, A. Staykov and K. Yoshizawa, *J. Phys. Chem. C*, 2012, **116**, 16325–16332.

86 S. Fujii, S. Marqués-González, J. Y. Shin, H. Shinokubo, T. Masuda, T. Nishino, N. P. Arasu, H. Vázquez and M. Kiguchi, *Nat. Commun.*, , DOI:10.1038/ncomms15984.

87 X. Yin, Y. Zang, L. Zhu, J. Z. Low, Z. F. Liu, J. Cui, J. B. Neaton, L. Venkataraman and L. M. Campos, *Sci. Adv.*, , DOI:10.1126/sciadv.aao2615.

88 H. Liu, N. Wang, J. Zhao, Y. Guo, X. Yin, F. Y. C. Boey and H. Zhang, *ChemPhysChem*, 2008, **9**, 1416–1424.

89 L. Lafferentz, F. Ample, H. Yu, S. Hecht, C. Joachim and L. Grill, *Science*, 2009, **323**, 1193–1197.

90 D. J. Wold, R. Haag, M. A. Rampi and C. D. Frisbie, *J. Phys. Chem. B*, 2002, **106**, 2813–2816.

91 V. Kaliginedi, P. Moreno-García, H. Valkenier, W. Hong, V. M. García-Suárez, P. Buiter, J. L. H. Otten, J. C. Hummelen, C. J. Lambert and T. Wandlowski, *J. Am. Chem. Soc.*, 2012, **134**, 5262–5275.

92 J. R. Reimers and N. S. Hush, *J. Photochem. Photobiol. A Chem.*, 1994, **82**, 31–46.

93 A. Nitzan, *http://dx.doi.org/10.1146/annurev.physchem.52.1.681*, 2003, **52**, 681–750.

94 G. C. Solomon, D. Q. Andrews, R. P. Van Duyne and M. A. Ratner, *J. Am. Chem. Soc.*, 2008, **130**, 7788–7789.

95 A. Salomon, D. Cahen, S. Lindsay, J. Tomfohr, V. B. Engelkes and C. D. Frisbie, *Adv. Mater.*, 2003, **15**, 1881–1890.

96 Y. Tsuji, R. Movassagh, S. Datta and R. Hoffmann, *ACS Nano*, 2015, **9**, 11109–11120.

97 T. Tada and K. Yoshizawa, *J. Phys. Chem. B*, 2004, **108**, 7565–7572.

98 N. Ramos-Berdullas and M. Mandado, *Chem. – A Eur. J.*, 2013, **19**, 3646–3654.

99 T. Stuyver, S. Fias, F. De Proft and P. Geerlings, *Chem. Phys. Lett.*, 2015, **630**, 51–56.

100 N. Ramos-Berdullas, S. Gil-Guerrero and M. Mandado, *Int. J. Quantum Chem.*, , DOI:10.1002/qua.25651.

101 T. Stuyver, T. Zeng, Y. Tsuji, S. Fias, P. Geerlings and F. De Proft, *J. Phys. Chem. C*, 2018, **122**, 3194–3200.

102 T. Stuyver, T. Zeng, Y. Tsuji, P. Geerlings and F. De Proft, *Nano Lett.*, 2018, **18**,

7298–7304.

103 W. P. Su, J. R. Schrieffer and A. J. Heeger, *Phys. Rev. Lett.*, 1979, **42**, 1698–1701.

104 A. J. Heeger, S. Kivelson, J. R. Schrieffer and W. P. Su, *Rev. Mod. Phys.*, 1988, **60**, 781–850.

105 J. K. Asbóth, L. Oroszlány and A. Pályi, *A Short Course on Topological Insulators*, Springer International Publishing, Cham, 2016, vol. 919.

106 A. Martín Pendás, J. Contreras-García, F. Pinilla, J. D. Mella, C. Cardenas and F. Muñoz, *Chem. Commun.*, 2019, **55**, 12281–12287.

107 I. Belopolski, S.-Y. Xu, N. Koirala, C. Liu, G. Bian, V. N. Strocov, G. Chang, M. Neupane, N. Alidoust, D. Sanchez, H. Zheng, M. Brahlek, V. Rogalev, T. Kim, N. C. Plumb, C. Chen, F. Bertran, P. Le Fèvre, A. Taleb-Ibrahimi, M.-C. Asensio, M. Shi, H. Lin, M. Hoesch, S. Oh and M. Z. Hasan, *Sci. Adv.*, , DOI:10.1126/sciadv.1501692.

108 B. Cirera, A. Sánchez-Grande, B. de la Torre, J. Santos, S. Edalatmanesh, E. Rodríguez-Sánchez, K. Lauwaet, B. Mallada, R. Zbořil, R. Miranda, O. Gröning, P. Jelínek, N. Martín and D. Ecija, *Nat. Nanotechnol.*, 2020, **15**, 437–443.

109 T. Stuyver, S. Fias, F. De Proft, P. Geerlings, Y. Tsuji and R. Hoffmann, *J. Chem. Phys.*, 2017, **146**, 092310.

110 M. H. Garner, W. Bro-Jørgensen, P. D. Pedersen and G. C. Solomon, *J. Phys. Chem. C*, 2018, **122**, 26777–26789.

111 L. Li, S. Louie, A. M. Evans, E. Meirzadeh, C. Nuckolls and L. Venkataraman, *J. Am. Chem. Soc.*, 2023, **145**, 2492–2498.

112 L. Li, C. R. Prindle, W. Shi, C. Nuckolls and L. Venkataraman, *J. Am. Chem. Soc.*, 2023, **145**, 18182–18204.

113 W. Xu, E. Leary, S. Hou, S. ara Sangtarash, M. Teresa Gonzµlez, G. Rubio-Bollinger, Q. Wu, H. atef Sadeghi, L. Tejerina, K. E. Christensen, S. J. Higgins, C. J. Lambert, R. Nichols, H. L. Anderson, W. Xu, D. ejerina, P. H. rof L Anderson, D. Leary, S. J. Higgins, P. R. rof J Nichols, R. J. Nichols, S. Hou, D. Sangtarash, D. Q. Wu, D. H. Sadeghi, C. J. Lambert, D. Rubio-Bollinger and P. N. rof Agraït, *Angew. Chemie Int. Ed.*, 2019, **58**, 8378–8382.

114 Y. Zang, T. Fu, Q. Zou, F. Ng, H. Li, M. L. Steigerwald, C. Nuckolls and L. Venkataraman, *Nano Lett.*, 2020, **20**, 8415–8419.

115 E. Leary, B. Limburg, A. Alanazy, S. Sangtarash, I. Grace, K. Swada, L. J. Esdaile, M. Noori, M. T. González, G. Rubio-Bollinger, H. Sadeghi, A. Hodgson, N. Agralt, S. J. Higgins, C. J. Lambert, H. L. Anderson and R. J.

Nichols, *J. Am. Chem. Soc.*, 2018, **140**, 12877–12883.

116 N. Algethami, H. Sadeghi, S. Sangtarash and C. J. Lambert, *Nano Lett.*, 2018, **18**, 4482–4486.

117 S. Gunasekaran, D. Hernangómez-Pérez, I. Davydenko, S. Marder, F. Evers and L. Venkataraman, *Nano Lett.*, 2018, **18**, 6387–6391.

118 W. Xu, E. Leary, S. Sangtarash, M. Jirasek, M. T. González, K. E. Christensen, L. Abellán Vicente, N. Agraït, S. J. Higgins, R. J. Nichols, C. J. Lambert and H. L. Anderson, *J. Am. Chem. Soc.*, 2021, **143**, 20472–20481.

119 A. Bajaj and M. E. Ali, *Phys. Chem. Chem. Phys.*, 2023, **25**, 9607–9616.

120 L. Li, S. Gunasekaran, Y. Wei, C. Nuckolls and L. Venkataraman, *J. Phys. Chem. Lett.*, 2022, **13**, 9703–9710.

121 E. Heilbronner, *Tetrahedron Lett.*, 1964, **5**, 1923–1928.

122 R. A. Usmani, *Linear Algebra Appl.*, 1994, **212–213**, 413–414.

123 R. Movassagh, G. Strang, Y. Tsuji and R. Hoffmann, *J. Math. Phys.*, 2017, **58**, 033505.

124 M. A. Ratner and N. Abraham, *Science*, 2003, **300**, 1384–1389.

125 Y. Tsuji, R. Hoffmann, R. Movassagh and S. Datta, *J. Chem. Phys.*, 2014, **141**, 224311.

126 J. He, O. Sankey, M. Lee, N. Tao, X. Li and S. Lindsay, *Faraday Discuss.*, 2006, **131**, 145–154.

127 S. Datta, *Electronic Transport in Mesoscopic Systems*, Cambridge University Press, Cambridge, U.K., 1997.

128 K. Okazawa, Y. Tsuji and K. Yoshizawa, *J. Phys. Chem. C*, 2020, **124**, 3322–3331.

129 D. Q. Andrews, G. C. Solomon, R. P. Van Duyne and M. A. Ratner, *J. Am. Chem. Soc.*, 2008, **130**, 17309–17319.

130 M. H. Garner, H. Li, M. Neupane, Q. Zou, T. Liu, T. A. Su, Z. Shangguan, D. W. Paley, F. Ng, S. Xiao, C. Nuckolls, L. Venkataraman and G. C. Solomon, *J. Am. Chem. Soc.*, 2019, **141**, 15471–15476.

131 R. Diestel, *Graph Theory*, Springer, 5th edn., 2017.

132 N. Trinajstić, *Chemical graph theory*, CRC Press, Boca Raton, FL, 2nd edn., 1992.

133 N. Trinajstić, D. Babić, S. Nikolić, D. Plavšić, D. Amić and Z. Mihalić, *J. Chem. Inf. Comput. Sci.*, 1994, **34**, 368–376.

134 A. Graovac, I. Gutman, N. Trinajstić and T. Živković, *Theor. Chim. Acta*, 1972, **26**, 67–78.

135 R. B. Mallion, A. J. Schwenk and N. Trinajstić, *Croat. Chem. Acta*, 1974, **46**, 171–182.

136 H. Hosoya, *Bull. Chem. Soc. Jpn.*, 1971, **44**, 2332–2339.

137 H. Hosoya, *Theor. Chim. Acta*, 1972, **25**, 215–222.

138 N. Biggs, N. L. Biggs and B. Norman, *Algebraic graph theory*, Cambridge university press, 1993.

139 D. M. Cvetković, *Publ. Elektroteh. Fak. Univ. u Beogradu. Ser. Mat. i Fiz.*, 1970, **320**, 27–34.

140 P. Sautet and C. Joachim, *Chem. Phys. Lett.*, 1988, **153**, 511–516.

141 G. C. Solomon, D. Q. Andrews, T. Hansen, R. H. Goldsmith, M. R. Wasielewski, R. P. Van Duyne and M. A. Ratner, *J. Chem. Phys.*, 2008, **129**, 054701.

142 S. H. Ke, Y. Weitao and H. U. Baranger, *Nano Lett.*, 2008, **8**, 3257–3261.

143 C. R. Arroyo, S. Tarkuc, R. Frisenda, J. S. Seldenthuis, C. H. M. Woerde, R. Eelkema, F. C. Grozema and H. S. J. van der Zant, *Angew. Chemie Int. Ed.*, 2013, **52**, 3152–3155.

144 X. Li, A. Staykov and K. Yoshizawa, *Theor. Chem. Acc.*, 2011, **130**, 765–774.

145 Y. Tsuji and E. Estrada, *J. Chem. Phys.*, 2019, **150**, 204123.

146 A. R. Williams, P. J. Feibelman and N. D. Lang, *Phys. Rev. B*, 1982, **26**, 5433–5444.

147 Y. Xue, S. Datta and M. A. Ratner, *Chem. Phys.*, 2002, **281**, 151–170.

148 Y. Tsuji, R. Hoffmann, M. Strange and G. C. Solomon, *Proc. Natl. Acad. Sci. U. S. A.*, 2016, **113**, E413–E419.

149 N. Trinajstić, *J. Math. Chem.*, 1988, **2**, 197–215.

150 A. Jeffrey, *Advanced Engineering Mathematics*, Harcourt Academic Press, San Diego, CA, 2002.

151 H. Sachs, *Publ. Math. Debrecen*, 1962, **9**, 11.

152 A. Graovac, O. E. Polansky, N. Trinajstić and N. Tyutyulkov, *Zeitschrift für Naturforsch. A*, 1975, **30**, 1696–1699.

153 E. Heilbronner and H. Bock, *HMO model and its application, Basis and Manipulation*, Wiley, London, 1976.

154 T. A. Albright, J. K. Burdett and M.-H. Whangbo, *Orbital Interactions in Chemistry*, John Wiley & Sons, Inc., Hoboken, NJ, USA, 2nd edn., 2013.

155 T. Tada and K. Yoshizawa, *J. Phys. Chem. B*, 2003, **107**, 8789–8793.

156 Y. Tsuji, T. Stuyver, S. Gunasekaran and L. Venkataraman, *J. Phys. Chem. C*, 2017, **121**, 14451–14462.

157 X. Liu, S. Sangtarash, D. Reber, D. Zhang, H. Sadeghi, J. Shi, Z.-Y. Xiao, W.

Hong, C. J. Lambert and S.-X. Liu, *Angew. Chemie Int. Ed.*, 2017, **56**, 173–176.

158 M. Gantenbein, L. Wang, A. A. Al-jobory, A. K. Ismael, C. J. Lambert, W. Hong and M. R. Bryce, *Sci. Rep.*, 2017, **7**, 1794.

159 Y. Yang, M. Gantenbein, A. Alqorashi, J. Wei, S. Sangtarash, D. Hu, H. Sadeghi, R. Zhang, J. Pi, L. Chen, X. Huang, R. Li, J. Liu, J. Shi, W. Hong, C. J. Lambert and M. R. Bryce, *J. Phys. Chem. C*, 2018, **122**, 14965–14970.

160 A. Al-Jobory and Z. Y. Mijbil, *Karbala Int. J. Mod. Sci.*, 2021, **7**, 10.

161 L. J. O'Driscoll, S. Sangtarash, W. Xu, A. Daaoub, W. Hong, H. Sadeghi and M. R. Bryce, *J. Phys. Chem. C*, 2021, **125**, 17385–17391.

162 S. Sangtarash, H. Sadeghi and C. J. Lambert, *Nanoscale*, 2016, **8**, 13199–13205.

163 I. Fernandez, *Aromaticity*, Elsevier, 2021.

164 B. A. Hess and L. J. Schaad, *J. Am. Chem. Soc.*, 1971, **93**, 305–310.

165 M. J. S. Dewar and G. J. Gleicher, *J. Am. Chem. Soc.*, 1965, **87**, 685–692.

166 M. J. S. Dewar and C. De Llano, *J. Am. Chem. Soc.*, 1969, **91**, 789–795.

167 A. Shurki, P. C. Hiberty, F. Dijkstra and S. Shaik, *J. Phys. Org. Chem.*, 2003, **16**, 731–745.

168 T. Stuyver, D. Danovich and S. Shaik, *J. Phys. Chem. A*, 2019, **123**, 7133–7141.

169 J. Aihara, *J. Am. Chem. Soc.*, 1976, **98**, 2750–2758.

170 I. Gutman, M. Milun and N. Trinajstic, *J. Am. Chem. Soc.*, 1977, **99**, 1692–1704.

171 J. Aihara, *Bull. Chem. Soc. Jpn.*, 2016, **89**, 1425–1454.

172 Y. Jiang, A. Tang and R. Hoffmann, *Theor. Chim. Acta*, 1984, **66**, 183–192.

173 Y. Jiang and H. Zhang, *Pure Appl. Chem.*, 1990, **62**, 451–456.

174 H. Hosoya, *Monatshefte für Chemie - Chem. Mon.*, 2005, **136**, 1037–1054.

175 J. R. Dias, *J. Phys. Chem. A*, 2021, **125**, 8482–8497.

176 J. K. Burdett, *Chemical bonds: a dialog*, John Wiley & Sons, 1997, vol. 13.

177 J. Clayden, N. Greeves and S. Warren, *Organic chemistry*, Oxford university press, London, England, 2nd edn., 2012.

178 C. Corminboeuf, P. von Ragué Schleyer and P. Warner, *Org. Lett.*, 2007, **9**, 3263–3266.

179 Y. Li and K. N. Houk, *J. Am. Chem. Soc.*, 1996, **118**, 880–885.

180 M. Alonso, J. Poater and M. Solà, *Struct. Chem.*, 2007, **18**, 773–783.

181 D. E. Bean and P. W. Fowler, *Org. Lett.*, 2008, **10**, 5573–5576.

182 J. Aihara, *J. Phys. Chem. A*, 2009, **113**, 7945–7952.

183 R. Nozawa, H. Tanaka, W.-Y. Cha, Y. Hong, I. Hisaki, S. Shimizu, J.-Y. Shin, T. Kowalczyk, S. Irle, D. Kim and H. Shinokubo, *Nat. Commun.*, 2016, **7**, 13620.

184 R. Nozawa, J. Kim, J. Oh, A. Lamping, Y. Wang, S. Shimizu, I. Hisaki, T.

Kowalczyk, H. Fliegl, D. Kim and H. Shinokubo, *Nat. Commun.*, 2019, **10**, 3576.

185 H. Kawashima, S. Ukai, R. Nozawa, N. Fukui, G. Fitzsimmons, T. Kowalczyk, H. Fliegl and H. Shinokubo, *J. Am. Chem. Soc.*, 2021, **143**, 10676–10685.

186 S.-Y. Liu, N. Kishida, J. Kim, N. Fukui, R. Haruki, Y. Niwa, R. Kumai, D. Kim, M. Yoshizawa and H. Shinokubo, *J. Am. Chem. Soc.*, 2023, **145**, 2135–2141.

187 J.-Y. Fujiyoshi, T. Tonami, M. Yamane, K. Okada, R. Kishi, S. Muhammad, A. G. Al-Sehemi, R. Nozawa, H. Shinokubo and M. Nakano, *ChemPhysChem*, 2018, **19**, 2863–2871.

188 T. M. Chen, Y. Tanaka, Y. Kametani, K. Cheng, C. Lin, Y. R. Lin, T. Hsu, Z. Chen, J. Hao, S. Mori, Y. Shiota, K. Yoshizawa, H. Furuta, S. Shimizu and C. Chen, *Angew. Chemie Int. Ed.*, 2022, **61**, e202212726.

189 M. J. Frisch, G. W. Trucks, H. B. Schlegel, G. E. Scuseria, M. A. Robb, J. R. Cheeseman, G. Scalmani, V. Barone, G. A. Petersson, H. Nakatsuji, X. Li, M. Caricato, A. V Marenich, J. Bloino, B. G. Janesko, R. Gomperts, B. Mennucci, H. P. Hratchian, J. V Ortiz, A. F. Izmaylov, J. L. Sonnenberg, D. Williams-Young, F. Ding, F. Lipparini, F. Egidi, J. Goings, B. Peng, A. Petrone, T. Henderson, D. Ranasinghe, V. G. Zakrzewski, J. Gao, N. Rega, G. Zheng, W. Liang, M. Hada, M. Ehara, K. Toyota, R. Fukuda, J. Hasegawa, M. Ishida, T. Nakajima, Y. Honda, O. Kitao, H. Nakai, T. Vreven, K. Throssell, J. A. Montgomery Jr., J. E. Peralta, F. Ogliaro, M. J. Bearpark, J. J. Heyd, E. N. Brothers, K. N. Kudin, V. N. Staroverov, T. A. Keith, R. Kobayashi, J. Normand, K. Raghavachari, A. P. Rendell, J. C. Burant, S. S. Iyengar, J. Tomasi, M. Cossi, J. M. Millam, M. Klene, C. Adamo, R. Cammi, J. W. Ochterski, R. L. Martin, K. Morokuma, O. Farkas, J. B. Foresman and D. J. Fox, 2016.

190 Y. Tsuji, K. Okazawa, B. Chen and K. Yoshizawa, *J. Phys. Chem. C*, 2020, **124**, 22941–22958.

191 D. W. Whitman and B. K. Carpenter, *J. Am. Chem. Soc.*, 1982, **104**, 6473–6474.

192 B. K. Carpenter, *J. Am. Chem. Soc.*, 1983, **105**, 1700–1701.

193 M. Eckert-Maksić, M. Vazdar, M. Barbatti, H. Lischka and Z. B. Maksić, *J. Chem. Phys.*, 2006, **125**, 064310.

194 J. Shen and P. Piecuch, *J. Chem. Phys.*, 2012, **136**, 144104.

195 E. Monino, M. Boggio-Pasqua, A. Scemama, D. Jacquemin and P.-F. Loos, *J. Phys. Chem. A*, 2022, **126**, 4664–4679.

196 P. U. Manohar and A. I. Krylov, *J. Chem. Phys.*, 2008, **129**, 194105.

197 M. Solà, F. Feixas, J. O. C. Jiménez-Halla, E. Matito and J. Poater, *Symmetry (Basel).*, 2010, **2**, 1156–1179.

198 I. Casademont-Reig, T. Woller, J. Contreras-García, M. Alonso, M. Torrent-Sucarrat and E. Matito, *Phys. Chem. Chem. Phys.*, 2018, **20**, 2787–2796.

199 P. von R. Schleyer, H. Jiao, N. J. R. van E. Hommes, V. G. Malkin and O. L. Malkina, *J. Am. Chem. Soc.*, 1997, **119**, 12669–12670.

200 P. Von Ragué Schleyer, M. Manoharan, Z. X. Wang, B. Kiran, H. Jiao, R. Puchta and N. J. R. Van Eikema Hommes, *Org. Lett.*, 2001, **3**, 2465–2468.

201 Z. Chen, C. S. Wannere, C. Corminboeuf, R. Puchta and P. von Ragué Schleyer, *Chem. Rev.*, 2005, **105**, 3842–3888.

202 H. Fallah-Bagher-Shaidaei, C. S. Wannere, C. Corminboeuf, R. Puchta and P. v. R. Schleyer, *Org. Lett.*, 2006, **8**, 863–866.

203 S. Klod and E. Kleinpeter, *J. Chem. Soc. Perkin Trans. 2*, 2001, 1893–1898.

204 E. Kleinpeter, S. Klod and A. Koch, *J. Mol. Struct. THEOCHEM*, 2007, **811**, 45–60.

205 R. Herges and D. Geuenich, *J. Phys. Chem. A*, 2001, **105**, 3214–3220.

206 D. Geuenich, K. Hess, F. Köhler and R. Herges, *Chem. Rev.*, 2005, **105**, 3758–3772.

207 J. Pedersen and K. V. Mikkelsen, *RSC Adv.*, 2022, **12**, 2830–2842.

208 T. Yanai, D. P. Tew and N. C. Handy, *Chem. Phys. Lett.*, 2004, **393**, 51–57.

209 A. D. Becke, *J. Chem. Phys.*, 1993, **98**, 1372–1377.

210 S. Grimme, J. Antony, S. Ehrlich and H. Krieg, *J. Chem. Phys.*, 2010, **132**, 154104.

211 S. Grimme, S. Ehrlich and L. Goerigk, *J. Comput. Chem.*, 2011, **32**, 1456–1465.

212 J. Witte, N. Mardirossian, J. B. Neaton and M. Head-Gordon, *J. Chem. Theory Comput.*, 2017, **13**, 2043–2052.

213 K. Momma and F. Izumi, *J. Appl. Crystallogr.*, 2011, **44**, 1272–1276.

214 K. B. Wiberg, *Tetrahedron*, 1968, **24**, 1083–1096.

215 E. D. Glendening, J. K. Badenhoop, A. E. Reed, J. E. Carpenter, J. A. Bohmann, C. M. Morales, P. Karafiloglou, C. R. Landis and F. Weinhold, 2019.

216 P. B. Lutz and C. A. Bayse, *Int. J. Quantum Chem.*, 2018, **118**, e25513.

217 Y. Shiota, M. Kondo and K. Yoshizawa, *J. Chem. Phys.*, 2001, **115**, 9243–9254.

Acknowledgement

The writing and completion of this dissertation would not have been possible without the assistance, support, and guidance of many teachers, colleagues, co-workers, and family members. It is my great pleasure to thank these people.

First of all, I would like to express my sincere gratitude to my supervisor, Professor Kazunari Yoshizawa, for leading me to the fascinating research field of quantum chemistry. His comments, suggestions, and encouragement have been of great value for my study.

I am deeply indebted to Associate Professor Yuta Tsuji for teaching me about single-molecule electronics, frontier orbital theory, graph theory, surface chemistry, and detailed technical support. I could not complete this dissertation without numerous discussions with him and his helpful advice.

I am thankful to Associate Professor Yoshihito Shiota and Assistant Professor Yosuke Sumiya, for their helpful advice, fruitful discussions, and technical support of computers. I am also thankful to Dr. Taiji Nakamura and Dr. Amit Shrestha for their kind comments on my research.

I would like to thank all members of the Yoshizawa laboratory for their supports and warm encouragements.

This work was financially supported by Research Fellowship of the Japan Society for the Promotion of Science for Young Scientists and JST, the establishment of university fellowships toward the creation of science technology innovation.

Finally, I would like to dedicate this dissertation to my family members for their continuous supports and warm encouragements.

Fukuoka, December 2023

Kazuki Okazawa

List of Publications

Chapter 3

“Understanding Single-Molecule Parallel Circuits on the Basis of Frontier Orbital Theory”
Kazuki Okazawa, Yuta Tsuji, and Kazunari Yoshizawa.
The Journal of Physical Chemistry C, **124**, 3322-3331 (2020).

Chapter 4

“Frontier Orbital View on the Disappearance of Reversed Conductance Decay in Highly Conductive Polyacetylene Wires Based on One-Dimensional Topological Insulators”
Kazuki Okazawa, Yuta Tsuji, and Kazunari Yoshizawa.
to be submitted.

Chapter 5

“Graph-theoretical exploration of the relation between conductivity and connectivity in heteroatom-containing single-molecule junctions”
Kazuki Okazawa, Yuta Tsuji, and Kazunari Yoshizawa.
The Journal of Chemical Physics, **156**, 091102 (2022).

Chapter 6

“Frontier Orbital Views of Stacked Aromaticity”
Kazuki Okazawa, Yuta Tsuji, and Kazunari Yoshizawa.
The Journal of Physical Chemistry A, **127**, 4780-4786 (2023).

The following papers are not included in this thesis.

(1) "Photo-Induced Ring-Opening Reaction of Flav-3-en-2-ol Monitored by Time-Resolved Infrared Spectroscopy"
Masato Kondoh, Akira Sakuta, Kazuki Okazawa, Dai Akase, Misako Aida, and Taka-aki Ishibashi.
The Journal of Physical Chemistry B, **123**, 8499-8504 (2019).

(2) "Time-resolved infrared study of photo-induced ring-closure reaction of trans-2-hydroxychalcone"
Masato Kondoh, Chinatsu Takizawa, Kazuki Okazawa, Dai Akase, Misako Aida, and Taka-aki Ishibashi.
Journal of Photochemistry and Photobiology A: Chemistry, **389**, 112280 (2020).

(3) "Mechanical Control of Molecular Conductance and Diradical Character in Bond Stretching and π-Stack Compression"
Yuta Tsuji, Kazuki Okazawa, Bo Chen, and Kazunari Yoshizawa.
The Journal of Physical Chemistry C, **124**, 22941-22958 (2020).

(4) "Electronic Origin of Catalytic Activity of TiH_2 for Ammonia Synthesis"
Yuta Tsuji, Kazuki Okazawa, Yoji Kobayashi, Hiroshi Kageyama, and Kazunari Yoshizawa.
The Journal of Physical Chemistry C, **125**, 3948-3960 (2021).

(5) "Topology Dictates Magnetic and Conductive Properties of a π-Stacked System: Insight into Possible Coexistence of Magnetic and Conductive Systems"
Yuta Tsuji, Kazuki Okazawa, Keita Kurino, and Kazunari Yoshizawa.
The Journal of Physical Chemistry C, **126**, 3244-3256 (2022).

(6) “Exploring the Optimal Alloy for Nitrogen Activation by Combining Bayesian Optimization with Density Functional Theory Calculations”
Kazuki Okazawa, Yuta Tsuji, Keita Kurino, Masataka Yoshida, Yoshifumi Amamoto, and Kazunari Yoshizawa.
ACS Omega, **7**, 45403-45408 (2022).

(7) “Mechanistic origins of accelerated hydrogenation of mixed alkylaromatics by synchronised adsorption over Rh/SiO_2”
Nikolay Cherkasov, Shunsaku Asano, Yuta Tsuji, Kazuki Okazawa, Kazunari Yoshizawa, Hiroyuki Miyamura, Jun-ichiro Hayashi, Alexander A. Kunitsa, and S. David Jackson.
Reaction Chemistry & Engineering, **8**, 1341-1348 (2023).

(8) “Extraordinary Acceleration of an Electrophilic Reaction Driven by the Polar Surface of 2D Aluminosilicate Nanosheets”
Nagy L. Torad, Yuta Tsuji, Azhar Alowasheeir, Masako Momotake, Kazuki Okazawa, Kazunari Yoshizawa, Michio Matsumoto, Masafumi Yamato, Yusuke Yamauchi, and Miharu Eguchi.
Small, **19**, 2205857 (2023).

(9) “Molecular Understanding of Adhesion of Epoxy Resin to Graphene and Graphene Oxide Surfaces in Terms of Orbital Interactions”
Amit Shrestha, Yosuke Sumiya, Kazuki Okazawa, Takahiro Uwabe, and Kazunari Yoshizawa.
Langmuir, **39**, 5514-5526 (2023).

(10) “Exploring Metal Nanocluster Catalysts for Ammonia Synthesis Using Informatics Methods: A Concerted Effort of Bayesian Optimization, Swarm Intelligence, and First-Principles Computation”
Yuta Tsuji, Yuta Yoshioka, Kazuki Okazawa, and Kazunari Yoshizawa.
ACS Omega, **8**, 30335-30348 (2023).

(11) “Complexation-Triggered Fluctuation of π-Conjugation on an Antiaromatic Dicyanoanthracene Dianion”
Taiki Imagawa, Kazuki Okazawa, Kazunari Yoshizawa, Hiroto Yoshida, Rong Shang, Yohsuke Yamamoto, and Masaaki Nakamoto.
Chemistry–A European Journal, e202302550 (2023).

(12) “Hückel Molecular Orbital Analysis for Stability and instability of Stacked Aromatic and Stacked Antiaromatic Systems”
Yuta Tsuji, Kazuki Okazawa, and Kazunari Yoshizawa
The Journal of Organic Chemistry, **88**, 14887-14898 (2023).

(13) “A machine learning approach to designing tough and degradable polyamides based on multiblock structures”
Yoshifumi Amamoto, Chie, Koganemaru, Ken Kojio, Atsushi Takahara, Sayoko Yamamoto, Kazuki Okazawa, Yuta Tsuji, Toshimitsu Aritake, Kei Terayama.
submitted, (preprint DOI: 10.26434/chemrxiv-2023-jm387)

(14) “芳香族単分子並列回路の電気伝導度とフロンティア軌道の関係”
岡澤 一樹, 辻 雄太, 吉澤 一成.
Journal of Computational Chemistry, Japan, **18**, 227-229 (2019).

(15) “ヘテロ原子を含んだ単分子接合の導電性に関するグラフ理論的研究”
岡澤 一樹, 辻 雄太, 吉澤 一成.
Journal of Computational Chemistry, Japan, **19**, 158-160 (2020).

(16) “積層芳香族性を有するπスタック単分子接合の伝導特性に関する理論的研究”
岡澤 一樹, 辻 雄太, 吉澤 一成.
Journal of Computational Chemistry, Japan, **21**, 87-89 (2022).